Fluid Mechanics and Bio-Transport Phenomena in Imaging of Biological Membranes Using AFM-Integrated Microelectrode

A Thesis
Presented to
The Academic Faculty

by

Tai-Hsi Fan

In Partial Fulfillment
of the Requirements for the Degree
Doctor of Philosophy in Mechanical Engineering

Georgia Institute of Technology
Nov 2003

Fluid Mechanics and Bio-Transport Phenomena in Imaging of Biological Membranes Using AFM-Integrated Microelectrode

Approved by:

Dr. Andrei G. Fedorov, Advisor

Dr. Mostafa Ghiaasiaan

Dr. Cheng Zhu

Dr. Boris Mizaikoff

Dr. John Pelesko

Date Approved November 18, 2003

ACKNOWLEDGEMENTS

Last two years have been a richest learning time for me in mathematical modeling. Nearly all knowledge was gained by solving a complex biological system led by my advisor, Professor Andrei Fedorov. I am most grateful to him for his patient guidance and encouragement throughout this research work and other projects. I have been enjoying many delightful discussions with him since the first day I came to Georgia Tech four years ago, and most importantly, continuously perceived the spirit and essence of academic research.

Among the thesis committee members, I would like to thank Professor Boris Mizaikoff for his initialization of this multidisciplinary project that has led to many fruitful results. I am also thankful to Drs. Christine Kranz and Angelika Kueng from the Professor Mizaikoff's group for sharing important information from AFM-SECM experiments. I also thank Professor Cheng Zhu for many insightful comments in modeling of a cell-level biological system, and Dr. Mostafa Ghiaasiaan for his careful review and comments on my thesis. I am especially thankful to Professor John Pelesko for his course in applied mathematics; it was a very enjoyable learning process in both physical and mathematical aspects.

I am grateful to my master thesis advisor, Professor Fan-Bill Cheung of the Pennsylvania State University. For many years, he has continuously encouraged me to pursue an academic career. I also thank Professor Wenjing Ye for helping me learn the boundary integral method, which has been a major analysis tool applied in this thesis.

I am thankful to my colleagues of Chen-Tech industries who mentored me to be an organized, hard working engineer in aerospace industry. Beyond my expectation, this has been a great help to me in the graduate school.

I acknowledge my undergraduate teachers, Professors Tung Wan and Dao-Lien Cherng of Tamkang University, for introducing computational mechanics to me; my best friends at the Penn State University, C.C. Yang and Y.H. Chen, for their friendship and encouragement; S.L. Lin, for sharing the dream when we were young; many graduate students in the Professor Fedorov's laboratory and the MEMS group, for broadening my view of modern technologies.

I would like to thank my parents; I am deeply indebted to them for showing the greatest tolerance to their beloved son, especially during the time when I almost flunked out of college. They also provided financial support for my early studies in the US. I also thank my other family members, for their continuous encouragement.

Theoretical work is a lonely, and oftentimes a very frustrating process. The only treat is a bit of taste of beauty in nature. I am very grateful to my lovely wife, and my best friend, Ruei-Fong; without her love, understanding, and encouragement, I would not be able to complete this work.

Finally, I thank God for strengthening my mind and leading my life.

TABLE OF CONTENTS

LIST OF FIGURES

NOMENCLATURE

a	final radius of the swelling matrix
Δa_0	total displacement of the swelling matrix interface
A	surface area
b	pseudo-source term
B	bending rigidity
c_0	spontaneous curvature
c_1, c_2	principal curvatures
C	species concentration
D	characteristic diameter of a biological cell, molecular diffusivity
D_r	relative diffusivity (D_{matrix} / D_{bulk})
$\hat{D}_r$	relative diffusivity (D_{swell} / D_{matrix})
e	single electron charge
$\hat{\mathbf{e}}$	unit vector
E	curvature free energy
$\mathbf{E}$	electric field
$\mathbf{f}$	surface force
f	effective friction coefficient between polymer matrix and solvent
f_{mik}	particular solution
$\mathbf{f}^{eh}$	electrohydrodynamic force
$\mathbf{f}^{M}$	Maxwell electric force
F	Faraday constant

$\mathbf{F}$	body force
G	shear modulus of elasticity
G_L	fundamental solution of the Laplace operator
G_p	fundamental solution of the adjoint Poisson operator
G_{ij}	fundamental solution of Stokes flow (Stokeslet)
H	mean curvature
i	local current density
I	Faradaic current response
K	Gaussian curvature, bulk modulus of elasticity
k_B	Boltzmann constant
k	modulus of an elliptic integral
ℓ	variable of a line integral
M	ring-source type Green's function, molar concentration unit
n	valence number of the released neurotransmitter
n_i	number density of ionic species i
n_c	ionic strength of electrolyte solution
$\mathbf{n}$	surface normal
$p.v.$	Cauchy principal value
p	fluid flow pressure field, modulus of an elliptic integral
Q	normal gradient of ring-source type Green's function
r	distance between source and field points, spatial variable in the radial direction
r_{mk}	radial basis function

$\mathbf{r}(\xi,\eta)$ position vector in a surface curvalinear coordinate system

R AFM tip radius

R_0 initial radius of a secretory vesicle

s arc length coordinate

$\mathbf{S}$ source term

t time

T absolute temperature

T_{ijk} stress field corresponding to fundamental solution of Stokes flow (Stresslet)

$\hat{\mathbf{t}}_s$ surface tangent along the arc length coordinate s

$\mathbf{u}$ elastic displacement field

$\mathbf{v}$ fluid flow velocity field

V volume

V_0 AFM tip probing speed, maximum expansion velocity of a fusion pore

x coordinate along the axial direction

$\mathbf{x}$ position vector in Cartesian coordinate system

$\mathbf{x}_0$ position vector of singular source point

z_i valence number of ionic species

Greek Symbols

α opening angle of AFM tip, dimensionless parameter ($\varepsilon_\ell \varepsilon_0 \kappa \zeta^2 / \mu V_0$)

α_k, β_k interpolation coefficients

β_n eigenvalue

γ surface tension/compression force

λ	viscosity ratio (μ_{env}/μ_{cyt})
ρ	fluid density
ρ_e	volumetric charge density
μ	dynamic viscosity
σ	cylindrical coordinate along the radial direction
ϕ	electric potential
ϕ_{mk}	interpolating function
θ	azimuthal angle
δ	Kronecker delta function
τ	fluid viscous stress field, linear elastic stress field
τ^M	Maxwell electric stress field
ζ	characteristic electric potential (k_BT/e)
κ^{-1}	Debye length of electric double layer
ε_0	permittivity of vacuum
$\varepsilon_\ell, \varepsilon_t$	relative permittivity of electrolyte solution and AFM tip
ε_r	relative dielectric constant ($\varepsilon_t/\varepsilon_\ell$)
Ω	computational domain
$\partial\Omega$	boundary of computational domain
ω	coefficient used in boundary integral formulation

SUMMARY

Living cells are enclosed by a protein integrated lipid bilayer membrane that separates them from other cells and the extracellular medium. They grow and communicate with each other by exchanging water, ions, and other macromolecules with the extracellular fluid through complex physiological processes that involve multitude of temporal and spatial scales. Biological membranes guard the cell structural integrity and rely on two main transport mechanisms to maintain basic biological functions: (i) the secretion of neurotransmitters/molecular messengers through a process of exocytosis, and (ii) water/ions transport mediated by the channel proteins. Understanding of biomembrane transport mechanisms is one of the key issues in modern biophysics. This understanding has direct impact on developing new diagnostic tools for human diseases as well as clinical treatments from gene therapy, to drug delivery, and to tissue engineering of artificial organs.

An integrated atomic force (AFM) and scanning electrochemical (SECM) microscope is a new instrument that provides a unique opportunity to study the cell communication processes *in-situ* with unprecedented spatial/temporal resolutions. One of the main challenges in AFM-SECM experiments lies in data interpretation during imaging of biological cells. For example, deformation of the cell membrane, intra and extra cellular electrolyte flow, species transport and reaction kinetics, and the electric current response detected by an electrode are intimately coupled processes resulting in data convolution and difficulty of result interpretation. Thus, development of the fundamental sound, yet computationally efficient theoretical models to resolve the interacting physical phenomena in the AFM-SECM probing process is necessary to optimize the operating

conditions of the instrument and to understand/interpret the biological phenomena from the experimental data under actual physiological conditions.

This thesis is divided into three integral parts, addressing fundamental issues from fluid mechanics and surface force analysis in AFM imaging to molecular messenger transport during a vesicular exocytotic event and its detection by a SECM microelectrode. In chapter 1, the effect of fluid mechanics of the inner and outer cellular fluids combined with the simplified bilayer membrane biomechanics is quantified for a noncontact, nonresonant mode AFM imaging process. In chapter 2, the analysis is extended to investigate the interactions between a dielectric AFM tip and a charged bilayer membrane in a dilute electrolyte solution. The coupled electric double-layer theory is solved in conjunction with the membrane biomechanics and electrohydrodynamics in the limits of the continuum theories. In chapter 3, a theoretical model is developed to simulate the intimately coupled transport and kinetics of an exocytotic release of molecular messengers. The analysis considers the pore expansion dynamics, membrane unfolding, and granular matrix swelling that culminates with the neurotransmitter/hormone release. The simulation results are qualitatively compared with the experimental results from the literature of *in vitro* electroanalytical measurements. Finally, an important analytical technique, the boundary integral method, is applied to solve the model governing equations and it is briefly summarized in Appendices A and B.

The major original contribution of this work is in two aspects: (i) development of the self-consistent theory for coupled electrohydrodynamics and biomechanics of AFM imaging of soft lipid bilayers and biomembranes, and (ii) development of the first-

principle model that predicts the biofluidic and biomechanical forces driving the exocytotic messenger release dynamics. Two peer-reviewed archival articles[1,2] have been published based on the results of this thesis research, and the third article[3] on the dynamics of exocytosis is being prepared for submission.

CHAPTER 1

Analysis of Hydrodynamic Interactions during AFM Imaging of Biological Membranes

The physical processes taking place during AFM imaging of soft biological membranes are investigated in this chapter. A particular emphasis is placed on understanding of hydrodynamics effects in the fluid inside and outside of the cell associated with elastic deformation of the membrane in response to AFM tapping action for the entire probing cycle. For the first time, it is theoretically shown that "hysteresis" in the membrane deformation versus tip-sample separation curve is due to strong coupling of fluid motion and kinematics of the membrane bending for the noncontact, nonresonant mode of measurements in liquid environment. The effects of the AFM tip opening angle and the membrane elasticity constants such as bending rigidity and spontaneous curvature are investigated in detail to establish the structure of the flow field and dynamics of the membrane evolution, leading to theoretical interpretation of AFM imaging experiments.

1.1 Introduction

The atomic force microscope (AFM) provides a unique opportunity to investigate spatially resolved structure, morphology, and mechanical properties of biological membranes down to the nanometer or atomic scale,[4] and these studies can be performed in-situ, i.e., in a natural aqueous environment for cells. Examples of using AFM in biology include investigation of the membrane structure, mechanical properties, and

surface charge of living osteoblasts,[5,6] measurement of molecular level interactions in microbial cells,[7] and even assessment of electrically excited cardiac activities in living cells.[8,9]

Mechanical properties of the cell membranes are typically deduced by generating an applied force versus distance curve when the AFM tip scans the surface and then fitting the experimental results to the simple Hertz model for the maximum distance between two elastically deformed surfaces.[10] Further, to preserve the integrity of the biological sample under investigation, the tapping mode of operation is used by vibrating the AFM tip at high frequency during surface scanning. However, since biological membranes are highly-deformable, fluid-like surfaces, the actual deformation of the membrane cannot be measured, thereby shading doubts on the validity of straight-forward application of the Hertz model to deduce mechanical properties of the membrane. Indeed, a more detailed model is needed which accounts for interactions between an AFM tip and the membrane surface through hydrodynamic coupling via the fluid layer between the tip and membrane. Such a model would provide a fundamental basis for quantitative interpretation of AFM imaging experiments as well as serve as a framework for designing new imaging modalities for non-invasive imaging of soft biological samples.

In this chapter, the development of the theoretical model and simulation results are presented for fluid mechanics of the AFM imaging of biological membranes. The model couples dynamics of the biological membrane deformation and fluid motion inside and outside of the cell as the AFM tip probes the membrane interface in periodic tapping mode. The fluid motion is modeled by the Stokes creeping flow, and Helfrich's theory for the equilibrium shape of an infinitely thin biological membrane[11,12] is used to determine

an instantaneous position of the flexible boundary that links fluid flows inside and outside of the cell. The boundary element method[13] is used as a numerical technique for computationally efficient solution of the problem. The results of simulations are intended to demonstrate the fundamental physics of what happens during AFM imaging of soft biological membranes as well as to assess the effect of main instrument/sample parameters (e.g., an AFM tip opening angle and the membrane elasticity constants such as bending rigidity and spontaneous curvature) on the force vs. distance response curves generated in the AFM imaging experiments. The cell membrane behavior when an AFM tip moves in forward and reverse directions is also observed. The practical benefits from this research are twofold. First, the cell mechanical properties can be obtained from a modified hydrodynamic force vs. distance curve without actually contacting or indenting the sample so that cell damage can be prevented. Second, the methodology to simulate the tip-sample interactions provides a theoretical foundation for interpretation of the convoluted experimental information obtained when multiple imaging functions are integrated into an AFM tip.[14]

1.2 Theoretical Development

1.2.1 Hydrodynamics Analysis

Figure 1.1 shows a schematic view of the AFM tip approaching a deformable cell surface. The size of the biological cell is usually much larger then that of an AFM tip, so that a simplified representation with an initially planar membrane surface can be adapted. In biological environment, the activities of microorganisms and living cells in the fluid

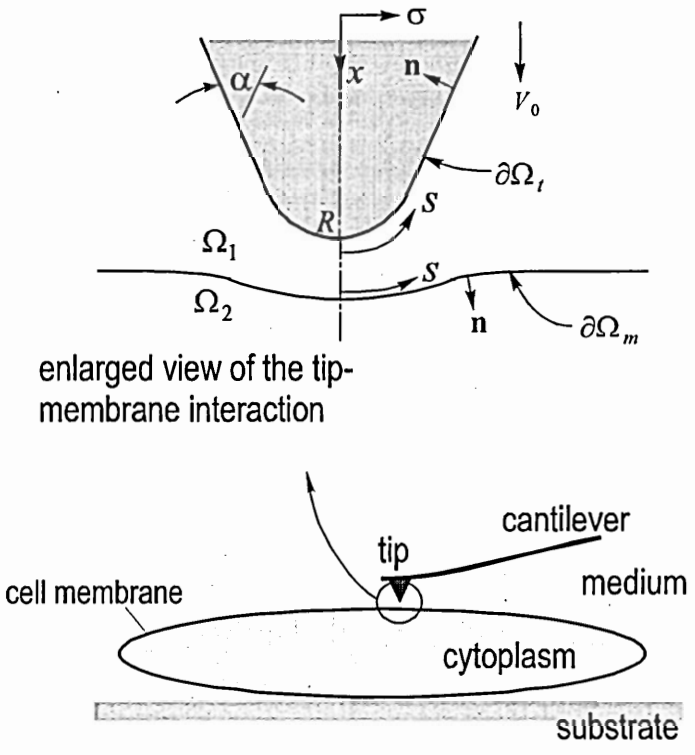

Figure 1.1 Schematic view of an AFM tip approaching a cell membrane and definition of the computational domain.

are usually characterized by the low Reynolds number flow because of the small velocity and length scales. For example, the size of biological cells ranges from few micrometers to several millimeters,[15] whereas the AFM tip is only tens to hundreds of nanometers in radius and up to several micrometers in height. Choosing the length scale as the height of an AFM tip, $L \sim 5\,\mu m$, and assuming that the cell living environment is an acqueous solution with viscosity $\mu \sim 0.015\,g/cm{\cdot}s$ and density $\rho \sim 1.0\,g/cm^3$, the low Reynolds number criteria [$\mathrm{Re} = \rho V_0 L/\mu << O(1)$] are satisfied as long as the characteristic speed V_0 of an AFM tip is less than $1\,cm/s$ ($\mathrm{Re} \sim 0.03$). In AFM imaging, we assume that the tip-to-sample distance is of the order of 5 μm and the vertical scanning frequency is around $f \sim 10\,Hz$.[5] Thus, the resulting characteristic velocity $V_0 \sim 0.01\,cm/s$ is much less than the minimum velocity dictated by the low Reynolds number criteria for the Stokes flow; hence, the advection inertia force can be neglected. The characteristic time scale for the system is $\tau = 1/f \sim 0.1\,s$, leading to the forcing frequency parameter $\rho L^2/\mu\tau$ of the order of 10^{-4} so that the acceleration force can also be neglected as compared to the viscous forces. Thus, the Stokes flow approximation is clearly justified for the system under consideration.

For simplicity, the fluids outside and inside of the cell are assumed incompressible Newtonian fluids with the same density and viscosity. A typical eukaryotic cell membrane with lipid bilayers and integrated glycoproteins is approximately $5\,nm$ thick, so that the membrane thickness can be neglected in comparison to the size of an AFM tip. Thus, the membrane can be mathematically treated as an infinitesimally thin interface. Besides, for the continuous fluid representation to be applicable, the thermal fluctuations are assumed to be negligible so that the membrane surface is perfectly smooth. Also the

system is assumed isothermal, no other body forces are involved, and the cell membrane is non-permeable. Furthermore, the molecular level interaction forces and the surface electrostatic force are not included in the analysis, as they become significant only at the tip-membrane separation around $50\,nm$ or less. Specifically, the van der Waals, electrostatic double layer, and solvations forces are significant when the interface separation distance is less then $10\,nm$, and their effective range is rarely longer than $100\,nm$.[16] Thus, neglecting molecular level interactions is justified in the present analysis, as it is correct to the order of magnitude of the the AFM tip radius ($500\,nm$).

On the basis of the Stokes flow approximation, the dynamics of both fluids, i.e., inside (Ω_2-domain) and outside (Ω_1-domain) of the cell (Figure 1.1), is governed by the following momentum and mass conservation equations

$$\nabla \cdot \boldsymbol{\tau}(\mathbf{x}) = -\nabla p(\mathbf{x}) + \mu \nabla^2 \mathbf{v}(\mathbf{x}) = 0, \quad \mathbf{x} \in \Omega_1 + \Omega_2 \tag{1-1}$$

$$\nabla \cdot \mathbf{v}(\mathbf{x}) = 0, \quad \mathbf{x} \in \Omega_1 + \Omega_2 \tag{1-2}$$

respectively, where $\boldsymbol{\tau}$ is the viscous stress tensor, p is the hydrodynamic pressure, $\mathbf{v}$ is the velocity field vector, μ is the dynamic viscosity assumed constant, and $\mathbf{x}$ denotes a position vector in the Cartesian coordinate system. The kinematic boundary conditions for the flow field are no-slip at both the AFM tip and the membrane surfaces,

$$\mathbf{v}(\mathbf{x}) = V_0 \hat{\mathbf{e}}_x, \quad \mathbf{x} \in \partial\Omega_t \tag{1-3}$$

$$\mathbf{v}(\mathbf{x}) = \mathbf{v}_m, \quad \mathbf{x} \in \partial\Omega_m \tag{1-4}$$

where V_0 is a prescribed appproach speed of the AFM tip, $\hat{\mathbf{e}}_x$ is the unit vector along the x-axis direction (Figure 1.1), and $\mathbf{v}_m$ is an unknown local migration velocity of the cell membrane. The rest of the unbounded fluid domain is assumed quiescent at infinity. The

solution of eqs 1-1 and 1-2 requires knowledge of the position of the cell membrane, which, in turn, is defined by the AFM induced flow in domains Ω_1 and Ω_2 (Figure 1.1), according to the migration velocity, which is not known a priori. Thus, to complete formulation of the problem, a dynamic boundary condition is required to couple the fluid motion on both sides of the cell membrane to determine migration of the membrane due to the hydrodynamic and membrane elasticity effects. This dynamic boundary condition can be obtained from the stress balance on both sides of the membrane, and it is discussed in detail in section 1.2.2.

Although the problem in hand is a transient nonlinear problem owing to an a priori unknown deformation of the cell membrane, the governing equations (1-1 and 1-2) are those for the simplified linear, quasi-steady Stokes flow. Thus, the problem can be solved by the general solution procedure for the Stokes flows,[13] while satisfying the nonlinear boundary condition at the cell membrane via numerical iterations. A convenient way to solve the linearized fluid flow problem is by using the boundary integral method, which originates from the Lorentz reciprocal theorem[17] in 1907. The integral solution of the Stokes flow problem was later outlined by Odqvist[18] and Ladyzhenskaya[19] by considering the solution as superposition of the contributions from a single layer (the flow induced by the continuously distributed point force, Stokeslet) and a double layer (the flow induced by the continuous point stress, Stresslet) potentials. The details of the theoretical development and numerical implementation of the integral formulation are discussed in detail by Pozrikidis.[13] The Lorentz reciprocal theorem gives a pair-wise relation between the real flow in the actual physical domain and the Stokeslet flow induced by the corresponding Green's function. Following Pozrikidis' derivation,[13] a

general integral solution of Stokes flow problem satisfies the following boundary integral equation:

$$\iint_{\partial\Omega}\left[\tau_{ik}(\mathbf{x})G_{ij}(\mathbf{x},\mathbf{x}_0)-\mu v_i(\mathbf{x})T_{ijk}(\mathbf{x},\mathbf{x}_0)\right]n_k(\mathbf{x})dA(\mathbf{x})=0 \tag{1-5}$$

where the singular source point is located outside the fluid domain, $\mathbf{x}_0 \notin \Omega$, the unit surface normal vector n_k points into the fluid domain, v_i and τ_{ik} represent the physical velocity and stress fields, respectively, and the fundamental solution (Stokeslet) and its corresponding stress field (Stresslet) are given by

$$G_{ij}(\mathbf{x},\mathbf{x}_0)=\frac{\delta_{ij}}{r}+\frac{r_i r_j}{r^3} \quad \text{and} \quad T_{ijk}(\mathbf{x},\mathbf{x}_0)=-6\frac{r_i r_j r_k}{r^5} \tag{1-6}$$

respectively, where δ_{ij} is the Kronecker delta function, $\mathbf{r}=\mathbf{x}\text{-}\mathbf{x}_0$ is the position vector between the given field point and a source point, and $r=|\mathbf{x}\text{-}\mathbf{x}_0|$ is the distance between them. When the source point is located inside the flow field, $\mathbf{x}_0 \in \Omega-\partial\Omega$, the combined Stokeslet and Stresslet induced velocity field must satisfy the following general integral solution:

$$v_j(\mathbf{x}_0)=-\frac{1}{8\pi\mu}\iint_{\partial\Omega}\tau_{ik}(\mathbf{x})n_k(\mathbf{x})G_{ij}(\mathbf{x},\mathbf{x}_0)dA(\mathbf{x})+\frac{1}{8\pi}\iint_{\partial\Omega}v_i(\mathbf{x})T_{ijk}(\mathbf{x},\mathbf{x}_0)n_k dA(\mathbf{x}) \tag{1-7}$$

An integral formulation of the Stokes flow problem for the two-fluid system with a free moving interface has been studied previously for fluids with arbitrary viscosity ratio.[20,21,22] We use this technique to find the surface force jump condition in the case when the viscosity ratio is unity, resulting in vanishing of the double layer integral at the surface of the cell membrane. To simplify notation, the traction term is replaced by the surface force expression, $f_i=\tau_{ik}n_k$, and the obvious position symbols are dropped hereafter in this chapter. Applying eq 1-7 to fluid 2 (inside of the cell) and eq 1-5 to fluid

1 (outside of the cell) and then combining the resulting equations, the flow field inside of the cell (domain Ω_2) can be expressed in terms of the surface force jump, $\Delta f_i = f_i^{(2)} - f_i^{(1)}$,

$$v_j^{(2)} = -\frac{1}{8\pi\mu}\int_{\partial\Omega_m}\Delta f_i G_{ij}\,dA + \frac{1}{8\pi\mu}\int_{\partial\Omega_t} f_i^{(1)} G_{ij}\,dA - \frac{1}{8\pi}\int_{\partial\Omega_t} v_i^{(1)} T_{ijk}\,n_k\,dA \tag{1-8}$$

with Δf_i becoming the source density acting on fluid 2 from the cell membrane surface. Here, $\partial\Omega_m$ and $\partial\Omega_t$ denote the surfaces of the cell membrane and of the AFM tip, respectively, and the superscripts (1) and (2) refer to the fluid domains outside (Ω_1) and inside (Ω_2) of the cell, respectively. Note that eq 1-8 is still valid even when the source point $\mathbf{x}_0$ is approaching the membrane surface, since the improper double layer integral ($\int_{\partial\Omega_m} v_i T_{ijk} n_k dA$) vanishes. Similar arguments can be applied to develop an integral momentum conservation equation for the fluid 1 oustide of the cell,

$$v_j^{(1)} = -\frac{1}{8\pi\mu}\int_{\partial\Omega_m}\Delta f_i G_{ij}\,dA + \frac{1}{8\pi\mu}\int_{\partial\Omega_t} f_i^{(1)} G_{ij}\,dA - \frac{1}{8\pi}\int_{\partial\Omega_t} v_i^{(1)} T_{ijk}\,n_k\,dA \tag{1-9}$$

An improper integral of the double layer potential (the third term in eq 1-9) is interpreted in the sense of Cauchy principal value when the source point is approaching the AFM tip surface, where we have

$$\lim_{\mathbf{x}_0\to\partial\Omega_t}\int_{\partial\Omega_t} v_i^{(1)} T_{ijk} n_k\,dA = -4\pi v_j + \overset{p.v.}{\int_{\partial\Omega_t}} v_i^{(1)} T_{ijk} n_k\,dA \tag{1-10}$$

To generalize the approach, the governing equations are non-dimensionlized by describing the fluid motion and membrane dynamics using the following scales: length scale is given by the AFM tip radius R, velocity is scaled by the tip approach velocity V_0, time is scaled by R/V_0, the local surface tension γ is scaled by $V_0\mu$, the membrane

bending rigidity B is scaled by $V_0\mu R^2$, the membrane mean curvature H and the spontaneous curvature c_0 are scaled by $1/R$, the Gaussian curvature K is scaled by $1/R^2$, and the surface force f and pressure p are both scaled by $V_0\mu/R$. Using these scales, the dimensionless integral form of the governing equations (1-8 and 9) becomes

$$\omega v_j = -\frac{1}{8\pi}\int_{\partial\Omega_m}\Delta f_i G_{ij}\,dA + \frac{1}{8\pi}\int_{\partial\Omega_t} f_i^{(1)} G_{ij}\,dA - \frac{1}{8\pi}\overset{p.v.\ for\ \mathbf{x}_0\in\partial\Omega_t}{\int_{\partial\Omega_t}} v_i T_{ijk} n_k\,dA \tag{1-11}$$

where

$$\omega = \begin{cases} 1 & for\ \ \mathbf{x}_0 \in \Omega_1 + \Omega_2 + \partial\Omega_m \\ 1/2 & for\ \ \mathbf{x}_0 \in \partial\Omega_t \end{cases} \tag{1-12}$$

with the boundary conditions

$$\mathbf{v}(\mathbf{x}) = 1\,\hat{\mathbf{e}}_x \ \text{ for } \ \mathbf{x}\in\partial\Omega_t, \ \ \mathbf{v}(\mathbf{x}) = \mathbf{v}_m \ \text{ for } \ \mathbf{x}\in\partial\Omega_m, \ \ \mathbf{v}(\mathbf{x}) = 0 \ \text{ for } \ \mathbf{x}\to\infty \tag{1-13}$$

Since the AFM tip, the cell membrane, and induced flow are axisymmetric, the surface integrals in eq 1-11 can be reduced to the line integrals by transforming the Cartesian coordinates to the polar cylindrical coordinates through $(x,y,z) = (x,\sigma\cos\theta,\sigma\sin\theta)$, and then integrating eq 1-11 along the azimuthal θ direction. As shown in Figure 1.1, x is the coordinate along the axial direction, σ is the coordinate along the radial direction, and ϕ is the azimuthal angle. The integral eq 1-11 is reduced to one-dimensional form by using the integral over the arc length s along the membrane boundary within a vertical plane defined by the constant azimuthal angle. The transformed integral equation is then expressed as

$$\omega\, v_\alpha = -\frac{1}{8\pi}\int_{\partial\Omega_m} M_{\alpha\beta}\,\Delta f_\beta\,ds + \frac{1}{8\pi}\int_{\partial\Omega_t} M_{\alpha\beta}\, f_\beta^{(1)} ds - \frac{1}{8\pi}\overset{p.v.\ for\ \mathbf{x}_0\in\partial\Omega_t}{\int_{\partial\Omega_t}} Q_{\alpha\beta\gamma}\, v_\gamma\, n_\beta ds \tag{1-14}$$

where ω is defined in eq 1-12, the Greek symbols α, β, γ denote either x or σ directions, and the kernel functions $M_{\alpha\beta}$ and $Q_{\alpha\beta\gamma}$ are the transformation matrices from Stokeslet and Stresslet in the Cartesian coordinate system.[13,20] Each matrix element in $M_{\alpha\beta}$ and $Q_{\alpha\beta\gamma}$ can be determined in terms of the complete elliptic integrals of the first and second kind and is either approximated by the asymptotic polynomials or computed by direct numerical integration. The details of transformations are given in the Appendix C for completeness.

1.2.2 Deformation of the Biological Membrane

Unlike the free interface between two immiscible fluids, mammalian cell membranes are constructed by amphiphilic molecules such as phospholipids or glycolipids with integrated functional proteins. The flexible and fluid-like lipid bilayers form an elastic interface which can resist bending and stretching to maintain the integrity of the membrane surface.[23] Since the lipid molecules are free to migrate or rearrange locally within the surface of the fluid-like membrane, the surface tension could be assumed locally isotropic on the time scale of interest in this study as long as the lipid bilayer has negligible shear elasticity and the membrane deformation is dominated by its bending rigidity. Considering a dynamic boundary condition for the surface force jump in a three dimensional free surface flow, a postulation generalized by Landau[24] and Scriven[25] takes the form

$$(\boldsymbol{\tau}_2 \cdot \mathbf{n} - \boldsymbol{\tau}_1 \cdot \mathbf{n}) + \nabla_s \gamma - \gamma \mathbf{n}(\nabla_s \cdot \mathbf{n}) = 0 \qquad (1\text{-}15)$$

where $\boldsymbol{\tau}_2 \cdot \mathbf{n} - \boldsymbol{\tau}_1 \cdot \mathbf{n}$ is the net surface traction acting along the surface normal $\mathbf{n}$ and tangent $\hat{\mathbf{t}}_s$ directions, ∇_s is a surface gradient operator, and γ is the surface tension. For

a fluid-like membrane characteristic to cells, the normal force component ($\gamma \nabla_s \cdot \mathbf{n}$) in eq 1-15 has to be generalized using the fluid membrane theory originated from Helfrich;[11] see also ref [26] in conjunction with a more recently developed equation for the equilibrium shape of a vesicle membrane.[12,27,28] It is now known that the major factor that defines an equilibrium shape of the cell membranes is the bending stiffness,[29] and the equilibrium membrane shape of a spherical vesicle is determined by the minimization of the curvature free energy, or shape energy[28]

$$E = \frac{1}{2} B \int (c_1 + c_2 - c_0)^2 dA + \Delta p \int dV + \int \gamma \, dA \qquad (1\text{-}16)$$

where B is the apparent bending rigidity, c_1 and c_2 are the two principal curvatures, c_0 is the effective spontaneous curvature that is used to describe various asymmetric effects in the membrane itself and its living environment,[29] $\Delta p = p_{out} - p_{in}$ is the osmotic pressure difference between outer and inner fluids of the cell, γ is the local surface tension, and $\int(...)dV$ and $\int(...)dA$ are integrals over the volume and surface of the cell, respectively. Taking the first variation of the shape energy given by eq 1-16, and treating Δp and γ as the Lagrange multipliers for the volume and surface constraints, respectively, Zhong-can and Helfrich[27] derived the equilibrium shape equation for the vesicle membranes

$$\Delta p - 2\gamma H + B(2H + c_0)(2H^2 - 2K - c_0 H) + 2B\nabla^2 H = 0 \qquad (1\text{-}17)$$

where $H = -(c_1 + c_2)/2$ is the mean curvature, $K = c_1 c_2$ is the Gaussian curvature, and ∇^2 is the Laplace-Beltrami operator for the curvilinear surface. In a dynamic system such as an AFM cell membrane immersed into a liquid, the viscous effects associated with motion of fluids on both sides of the interface must be included in eq 1-17 to describe the

surface force jump across the cell membrane. Thus, the balance of the normal force has to be generalized to obtain a Laplace-like formula, as shown by Zhong-can,[28]

$$(\boldsymbol{\tau}_2 \cdot \mathbf{n} - \boldsymbol{\tau}_1 \cdot \mathbf{n}) \cdot \mathbf{n} = \left[\Delta p - 2\gamma H + B(2H + c_0)(2H^2 - 2K - c_0 H) + 2B\nabla^2 H\right] \tag{1-18}$$

Assuming that the initial osmotic pressure difference Δp is zero for the planar membrane interface, the dynamic boundary condition (eq 1-15) can be modified as follows:

$$\Delta \mathbf{f} = \left[-2\gamma H + B(2H + c_0)(2H^2 - 2K - c_0 H) + 2B\nabla^2 H\right]\mathbf{n} - \nabla_s \gamma \tag{1-19}$$

where $\Delta \mathbf{f} = \boldsymbol{\tau}_2 \cdot \mathbf{n} - \boldsymbol{\tau}_1 \cdot \mathbf{n}$ enters the Stokes system describing fluid motion through eq 1-14.

In the free surface problems, the surface force jump $\Delta \mathbf{f}$ is solely determined by the surface geometry. For the flexible membrane, however, eq 1-19 shows that the local tension force γ must be known a priori in order to determine the surface force jump. Thus, an additional equation needs to be introduced based on the membrane surface constraint to complete the formulation. From differential geometry, the two surface curvilinear coordinates ξ and η can be introduced to describe the position vector $\mathbf{r}(\xi,\eta)$ defining the membrane surface. There exist two tangential vectors and the surface normal defined by

$$\mathbf{r}_\xi = \partial \mathbf{r}/\partial \xi, \quad \mathbf{r}_\eta = \partial \mathbf{r}/\partial \eta, \quad \mathbf{n} = (\mathbf{r}_\xi \times \mathbf{r}_\eta)/\left|\mathbf{r}_\xi \times \mathbf{r}_\eta\right| \tag{1-20}$$

and a useful covariant metric tensor defined for the general curvilinear system by

$$g_{ij} = \mathbf{r}_i \cdot \mathbf{r}_j \tag{1-21}$$

where i and j are either ξ or η directions. In the case of a locally incompressible cell membrane, the surface area must remain locally constant in time so that the dilation rate of a differential surface element satisfies the constraint

$$\frac{\partial(dA)}{\partial t}=\frac{\partial}{\partial t}\int\sqrt{g}\;\; d\xi\;\; d\eta=0 \tag{1-22}$$

with the 2-D Jacobian of the transformation given by

$$\sqrt{g}=\sqrt{\det(g_{ij})}=\left|\mathbf{r}_{\xi}\times\mathbf{r}_{\eta}\right| \tag{1-23}$$

Then eq 1-22 can be written in differential form

$$\mathbf{n}\cdot\frac{\partial}{\partial t}\left(\mathbf{r}_{\xi}\times\mathbf{r}_{\eta}\right)=0 \tag{1-24}$$

Using the orthogonal curvilinear surface coordinates, that is, the arc length s and the azimuthal angle θ, as ξ and η, respectively, the time derivative of eq 1-24 can be expressed in terms of components of the surface migration velocity $\mathbf{v}$,

$$\mathbf{n}\cdot\left(\mathbf{v}_{s}\times\mathbf{r}_{\theta}+\mathbf{r}_{s}\times\mathbf{v}_{\theta}\right)=0 \tag{1-25}$$

For $\mathbf{r}=(x,\sigma\cos\theta,\sigma\sin\theta)$ and $\mathbf{v}=(v_x,v_\sigma\cos\theta,v_\sigma\sin\theta)$, one can relate the unit tangent vector $\hat{\mathbf{t}}_s$ along the arc length coordinate s to the surface normal $\mathbf{n}$ by

$$\hat{\mathbf{t}}_{s}=-n_{\sigma}\hat{\mathbf{e}}_{x}+n_{x}\hat{\mathbf{e}}_{\sigma} \tag{1-26}$$

With that, we can further simplify eq 1-25 to obtain

$$\sigma\hat{\mathbf{t}}_{s}\cdot\frac{\partial\mathbf{v}}{\partial s}+\mathbf{v}\cdot\hat{\mathbf{e}}_{\sigma}=0 \tag{1-27}$$

Note that eq 1-27 is consistent with the Pozrikidis derivation for a nonisotropic stretching membrane by considering the constraint of the principal extension ratios.[30] Substituting eq 1-14 into eq 1-27 for $\mathbf{x}_0\in\Omega_m$, we obtain the membrane area constraint in the final compact form,

$$\int_{\partial\Omega_m}\left(\sigma(\mathbf{x}_0)\hat{t}_\alpha(\mathbf{x}_0)\frac{\partial M_{\alpha\beta}(\mathbf{x},\mathbf{x}_0)}{\partial s(\mathbf{x}_0)}+M_{\alpha\beta}(\mathbf{x},\mathbf{x}_0)\right)\Delta f_\beta(\mathbf{x})ds(\mathbf{x})$$
$$-\int_{\partial\Omega_t}\left(\sigma(\mathbf{x}_0)\hat{t}_\alpha(\mathbf{x}_0)\frac{\partial M_{\alpha\beta}(\mathbf{x},\mathbf{x}_0)}{\partial s(\mathbf{x}_0)}+M_{\alpha\beta}(\mathbf{x},\mathbf{x}_0)\right)f_\beta^{(1)}(\mathbf{x})ds(\mathbf{x}) \tag{1-28}$$
$$+\int_{\partial\Omega_t}\left(\sigma(\mathbf{x}_0)\hat{t}_\alpha(\mathbf{x}_0)\frac{\partial Q_{\alpha\beta\gamma}(\mathbf{x},\mathbf{x}_0)}{\partial s(\mathbf{x}_0)}+Q_{\alpha\beta\gamma}(\mathbf{x},\mathbf{x}_0)\right)v_\gamma(\mathbf{x})n_\beta(\mathbf{x})ds(\mathbf{x})=0$$

where α,β denote either σ or x directions, and the unknown local tension force γ can be obtained implicitly from $\Delta\mathbf{f}$ given by eq 1-19.

In summary, the linear integral equations (1-14 and 1-28) are developed for the boundary value problem that, combined with the flow boundary conditions given by eq 1-13 and the nonlinear interface boundary condition eq 1-19 defining the surface force jump as a function of the membrane geometry and the local surface tension, describes the flow of fluids inside and outside of the cell as well as membrane deformation during the AFM imaging process.

1.3 Numerical Method

The coupled fluid-membrane system is solved using the Boundary Element Method (BEM) with discretization along the surfaces of the AFM tip and the cell membrane. One advantage of this method is that no discretization of governing equations is needed inside the solution domain, but only along the boundaries. Once the boundary values are obtained, the field solutions (i.e., inside the domain) can be obtained through simple and computationally efficient post-processing calculations. Also, for the axisymmetric formulation, the dimensionality is further reduced to a one-dimensional problem, which significantly simplifies the solution of the problem.

The model is described by four integral equations (eq 1-14, given that α denotes two diretions, x and σ, and ω is defined by eq 1-12), and subject to one constraint integral equation (eq 1-28) for five unknown functions, $v_x(\mathbf{x})$ and $v_\sigma(\mathbf{x})$ for $\mathbf{x} \in \partial\Omega_m$, $f_x(\mathbf{x})$ and $f_\sigma(\mathbf{x})$ for $\mathbf{x} \in \partial\Omega_t$, and $\gamma(\mathbf{x})$ for $\mathbf{x} \in \partial\Omega_m$. The calculations use N_t and N_m collocation points for the AFM tip and the cell membrane, respectively. After descretization and numerical approximation of the integral equations, there are total $2N_t + 3N_m$ linear algebraic equations to be solved simultaneously at each time step. The initial state assumes that the membrane is planar and the AFM tip to the membrane separation distance is $10R$ (recall that R is the radius of the AFM tip). The position of an AFM tip and that of the cell membrane are advanced following the local velocity field at every time step using the Euler time integration method for each collocation point.[31] On the fluid membrane, the collocation points are rearranged at every time step by cubic spline interpolation with node clustering near the membrane center, while maintaining the total number of elements fixed. Observing that the decay of the Green's function is of the order of $(1/r)$, and that of the Stresslet is of the order of $(1/r^2)$, the surface integrals can be truncated without loss of accuracy at sufficiently large r. Although the membrane area also increases proportional to r, the truncation is still justified in evaluation of the first integral term in eq 1-11 because the surface curvatures (H and K) and the gradient of the surface tension $\nabla_s\gamma$ vanish at large distances r where the membrane becomes planar, resulting in fast decay of the surface force jump Δf_i with the distance r according to eq 1-19. In numerical calculations, the integral is truncated at the dimensionless radius $\sigma \approx 150$. The appropriate truncation distance is justified through sensitivity studies. The

element level integral is evaluated by the Gaussian quadrature,[31] and the system of algebraic equations is solved by the Gauss elimination method.[31]

Further, if we assume that the local membrane tension force γ is isotropic, the tangent component of the interface stress in eq 1-19 can be expressed in terms of an arc-length coordinate s as follows:

$$\nabla_s \gamma = \frac{\partial \gamma}{\partial s} \hat{\mathbf{t}}_s \tag{1-29}$$

Since γ is an unknown, this surface gradient operation is implemented in an implicit finite difference form to achieve numerical stability. The derivatives of the transformation matrices $\partial M_{\alpha\beta}/\partial s$ and $\partial Q_{\alpha\beta\gamma}/\partial s$ in eq 1-28 are evaluated by the central difference at the integration points. In general, the membrane boundary can be defined by the parametric equations, $x = x(s)$, $\sigma = \sigma(s)$ with s being the arc-length along membrane interface $\partial\Omega_m$ measured from the center point (Figure1.1). From differential geometry, the parametric forms for the mean curvature H and Gaussian curvature K are derived:

$$H(x(s),\sigma(s)) = \frac{\sigma\sigma' x'' + x' - \sigma'\sigma'' x'}{2\sigma} \tag{1-30}$$

$$K(x(s),\sigma(s)) = \frac{\sigma' x' x'' - \sigma'' x'^2}{\sigma} \tag{1-31}$$

Also, the Laplace-Beltrami term in eq 1-19 can be expressed in terms of the arc-length coordinate s as

$$\nabla^2 H = \frac{\partial^2 H}{\partial s^2} \tag{1-32}$$

In the evaluation of membrane curvatures in eqs 1-30 and 1-31, the continuous first- and second-order derivatives of $x(s)$ and $\sigma(s)$ along the arc-length are evaluated on a cubic

spline. The mean curvature $H(s)$ may exhibit small oscillations in the second order derivatives which prohibit the Laplacian operation in eq 1-32. A remedial way to increase the smoothness of the mean curvature is to use the piecewise polynomial fit along the arc-length s in the least-squares sense[31] and to compute the Laplacian directly from the polynomial representation. Numerical test showed that a third-order piecewise polynomial with between six to twelve point window size can filter out the small oscillation in $H(s)$.

It should be noted that mathematical developments above assume that all functions and their derivatives are sufficiently smooth to perform the differential operations. Besides, the uniqueness of the solution of the coupled integral equations (1-14 and 1-28) cannot be easily proven, since the unknown local membrane tension γ is defined as a Lagrange multiplier which may render multiple solutions of the problem. Our numerical experiments show that multiple converged solutions for γ do indeed exist, but the physically plausible solution is the one that results in $\gamma = 0$ at $\sigma \to \infty$, i.e. at the truncated membrane location, or an a priori known constant value for the planar membrane at the initial stage.

1.4 Results and Discussion

There are three basic interaction processes in respect to direction of the tip movement to characterize the fundamental modes of tip-membrane interactions in non-contact tapping mode: first, the AFM tip is approaching an initially planar membrane with a constant velocity in the positive x direction (*forward*) until the tip-membrane separation distance is equal to R (where R is the tip radius); second, the tip returns to its initial

position moving in the negative x direction (*reverse*); and third, the tip stops at its upper state and the membrane is allowed to freely relax and slowly return to its undeformed planar shape (*relaxation*). It should be noted that the driving mechanisms for the membrane deformation are different from those responsible for the free liquid-liquid interface evolution[21] because of the additional effects arising from the surface bending energy and the local tension or compression force induced by the constant area constraint, reflecting the assumption of the local membrane incompressibility. Although a harmonic, rather than a piece-wise-constant-velocity, motion of the cantilever is more realistic representation of the actual AFM tapping-mode operation, the main goal of this article is to uncover fundamental modes of fluid-membrane interactions under conditions which are relevant, but not necessarily identical, to current practices of using AFM for imaging soft samples. Indeed, the tip acceleration/deceleration under the harmonic cantilever motion will only convolute the insight into the basic physics of the problem, and simplified cantilever motion with a piecewise constant velocity provides an opportunity to reveal the key physical mechanisms of the AFM imaging process necessary for understanding and optimization of the process. Thus, because of the overwhelming complexity of the problem, the main goal here is to gain a fundamental insight and resolve key interaction mechanisms independently.

The results of presented simulations are based on the geometry of the computational domain defined by the following dimensionless quantities: the AFM tip height is $10R$, the initial tip-sample separation is $10R$, and the dimensionless time step is set to 0.1 and is increased to 2.0 in the final stage of the slow membrane relaxation. Several test cases with the dimensionless bending rigidity B varying from 0.1 to 20.0, the tip opening angle

ranging from 15° to 90°, and the spontaneous curvature c_0 changing from -0.1 to -5.0 are investigated by comparing corresponding force versus distance response curves. In all reported simulations, a total of 40 boundary elements are used for the tip and 60 elements are used for the cell membrane with element clustering around the center portion where the deformation is more significant. This set of simulation parameters was selected after an extensive grid sensitivity study based on its ability to produce the mesh-independent results with temporal and spatial resolutions sufficient for capturing the essential details of the system dynamics.

Figure 1.2 shows the membrane evolution during forward, reverse, and relaxation modes of AFM imaging. As a result of viscous flow induced by an AFM motion in fluid outside of the cell, the membrane is pushed forward (bends down) by the hydrodynamic piston force, and the fluid within the cell is in turn moved by the membrane with the highest local velocity around the center location. The curvature-dependent bending energy continuously changes with the membrane bending, thereby providing a local resistance to any deformation away from the planar, equilibrium state of the membrane of the minimum energy. This resistance causes different transient behavior during forward and reverse modes of AFM operation. In the *forward* (push) motion mode, an increase in the bending energy induces upward motion of the fluid above the membrane (negative local migration velocities of the fluid 1) against the hydrodynamic (forward directed) forces. On the other hand, in the *reverse* (pull) mode of operation, a decrease in the bending energy assists initially the membrane to withdraw from its highly deformed bend-down state. However, once the membrane returns to and passes its equilibrium

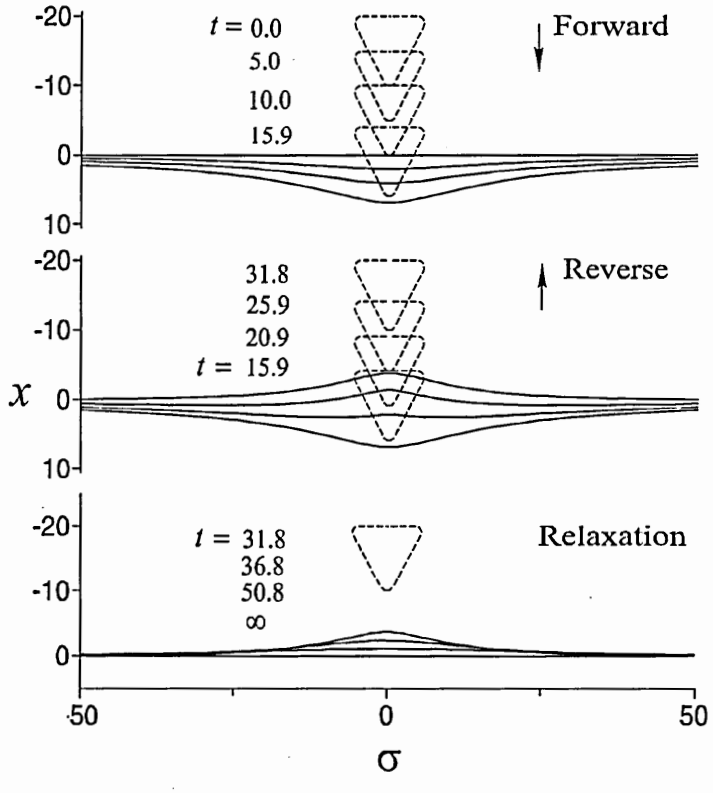

Figure 1.2 Full cycle evolution of the fluid membrane with bending rigidity $B = 1.0$ and spontaneous curvature $c_0 = -2.0$ induced by the AFM tip with an opening angle $\alpha = 60°$.

planar position going upward, the bending energy again starts increasing and begins to resist any further deformation of the membrane until the membrane reaches its maximum negative deformation when the AFM tip stops in its upper position. In the final *relaxation* stage, the migration of the membrane is slow and solely depends on its bending energy and the fluid viscosity. The evolution shows that the viscous hydrodynamic forces affect the membrane state even in the far field along the radial direction, which is a typical dragging behavior of the Stokes flows. If the simulations are continued for sufficiently long time, the membrane eventually returns to its equilibrium planar shape and the fluid velocity, the hydrodynamics forces, and the membrane surface forces vanish everywhere.

Figure 1.3 shows the axisymmetric streamlines and contours of the velocity field at the end of the forward and reverse motion of the AFM tip at time moments $t = 15.9$ and 31.8, respectively, for $B = 1.0$, $c_0 = -2.0$, and $\alpha = 60°$. The velocity field is computed as a post-processing step using eq 1-14 with $\lambda = 1.0$ after the boundary values of the velocity are calculated. The velocity field reveals the kinematics of the flow produced by the coupling effects of the AFM tip motion and elastic deformation of the cell membrane. A relatively high speed flow is induced in the wake behind the flat bottom area of the AFM tip due to the strong viscous dragging force from the bottom surface and a relatively weak response from the membrane. Right near the front of the AFM tip and around the cone-shaped surface of the tip, the induced flow field is suppressed by the strong opposite single-layer force potential distributed along the surface of the deformed membrane. As a result, the velocity magnitude is reduced but the local velocity gradient becomes greater. The moving tip causes a converging/diverging streamline pattern around the tip circumference, which is the behavior generally observed in the Stokes flows when the

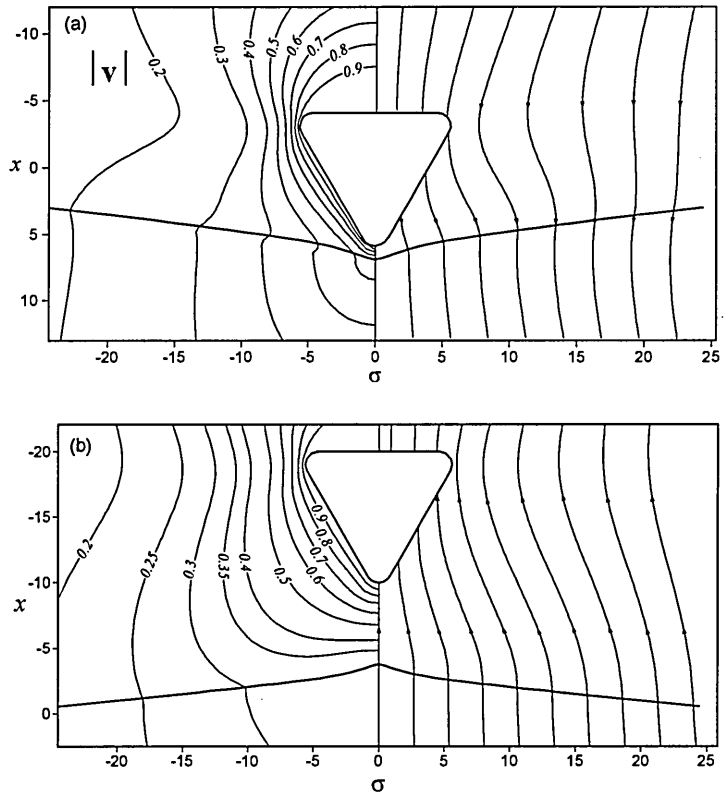

Figure 1.3 Instantaneous normalized velocity contours (left), and streamlines (right) around the AFM tip and the cell membrane at the following time instants: (a) $t = 15.9$ in the forward direction (b) $t = 31.8$ in the reverse direction for the membrane with bending rigidity $B = 1.0$, spontaneous curvature $c_0 = -2.0$, and the AFM tip with opening angle $\alpha = 60°$.

flow field is perturbed by a moving body of an arbitrary shape. The contours show that the velocity field decays significantly along the radial σ axis away from the centerline, which supports our choice of truncating the computational domain along the membrane at $\sigma = 150R$. For the case shown in Figure 1.3, the velocity magnitude diminishes by almost 80 percent when σ reaches $20R$, which is about twice as large as the tip height, and the same reduction percentage is achieved at the location $\sigma = 10R$ for the case with the narrow tip shown later in Figure 1.7. Note that both the velocity contours and the streamlines express the continuity of the velocity distribution and the viscous stress jump across the infinitesimally thin membrane interface. The stress jump becomes more significant as the membrane elasticity and the membrane tension force increase around the membrane center where the membrane bending is the greatest.

Figure 1.4 depicts the local isotropic tension ($\gamma > 0$) or compression ($\gamma < 0$) forces acting on the membrane with respect to the radial position during forward, reverse, and relaxation modes of operation. When the AFM tip is moving forward, the membrane is pushed down by the fluid flow and the tension force is induced to drag the membrane into the center area to satisfy the surface area constraint imposed by the membrane incompressibility (eq 1-28). In the reverse motion, compression is observed as the membrane is pulled back and forced to adopt a new shape with the smaller area. Even when the membrane recedes over its neutral equilibrium position in the reverse motion (Figure 1.2), the surface force is still in the compression mode because the strong hydrodynamic forces overcome the force induced by the slow membrane self-relaxation, thereby maintaining the compression state of the membrane on a shorter time scale.

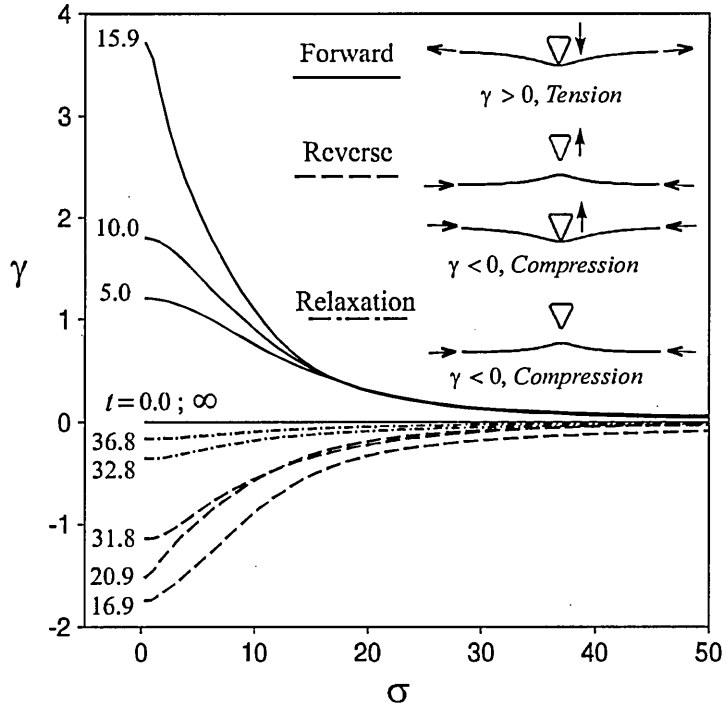

Figure 1.4 Isotropic local tension/compression force of the deforming membrane with bending rigidity $B = 1.0$ and spontaneous curvature $c_0 = -2.0$ probed by the AFM tip with an opening angle $\alpha = 60°$.

Figure 1.5 shows the instantaneous maximum deformation of the membrane (at the center) as a function of the instantaneous tip-membrane separation distance in a full cycle simulation. Clearly, this plot is analogous to the typical sampling force (proportional to membrane deformation) versus distance curves obtained experimentally during actual AFM imaging of biological cells. The range of experimentally measured bending rigidity values reported in the literature is $1.3\times10^{-20}\sim7\times10^{-19}J$ with the nominal value about $10^{-19}J$,[32,33,34,35] which translates into parameter B values ranging between 0.1 and 20. The greater bending rigidity translates into stronger membrane resistance to deformation as demonstrated by the smaller variation range for the trace curve along the y-axis. At the same time, during the reverse operation mode and when the bending rigidity is sufficiently large, the membrane initially moves faster than an AFM tip owing to the strong bending force acting on the membrane. This fact is manifested in Figure 1.5 by a decrease of the tip-membrane separation distance below 1.0 at the time moment just past 12.6, for the case of $B=5.0$. The lagging response is also observed when the minimum tip-membrane separation distance (equal to 1.0) is maintained at times t=18.6, 17.1, 15.9, 12.6, and 10.4 for the cases with bending rigidity $B=0.1$, 0.5, 1.0, 5.0, and 20.0, respectively. In the AFM imaging experiments, such an irreversible "hysteresis" behavior in respect to the forward and reverse motion of an AFM tip is frequently observed for soft samples, and the simulations provide the first theoretical evidence that this behavior is due to coupling of hydrodynamic and elastic membrane effects. Also, in the forward operation mode, as the tip approaches the membrane the tip-sample interaction becomes stronger and this results in a locally increased slope of the deformation curves when the tip-membrane separation distance approaches unity. The slope also appears much greater

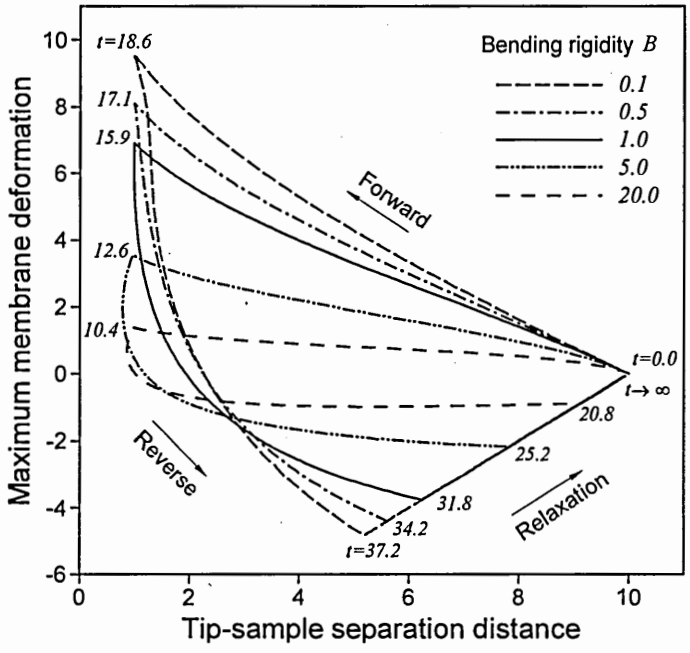

Figure 1.5 Effect of the bending rigidity on the hysteresis curve of the membrane deformation vs tip-sample separation distance for the membrane with spontaneous curvature $c_0 = -2.0$ and the AFM tip opening angle $\alpha = 60°$.

(i.e., a steeper change in the membrane deformation) in the beginning of the tip reverse motion due to contributions from both the bending force acting in upward direction and the upward hydrodynamic pull force induced by the reverse motion of the AFM tip. After passing through the equilibrium membrane position with zero bending energy, the bending force begins to act in the opposite direction relative to the hydrodynamic force leading to a decrease in the slope of deformation curves continuously until the AFM tip comes to rest at its upper elevated position. Finally, in the membrane relaxation mode, the deformation curves for all three bending rigidities are identical and the membrane relaxes to its equilibrium position as expected, featuring linear dependence on the tip-membrane separation distance.

In the AFM probing experiments, choosing the tip geometry is based on the characteristics of the sample surface and the requirements of the image resolution. Two of the most important factors affecting the image resolution are the tip sharpness (represented by the tip radius R) and the tip aspect ratio (represented by the tip opening angle α). Since our system is made dimensionless using the tip radius as a scale, the effect of the tip radius R is reflected in Figures 1.2-1.5. The effects of the tip opening angle are presented in Figures 1.6 and 1.7. Figure 1.6 illustrates the hysteresis plot for four different cases with the opening angle ranging from 15° to 90°. Clearly, a decrease in the AFM tip opening angle (tip sharpening) results in significant enhancement of the AFM sensitivity, as even small membrane deformation leads to a fairly large change in the separation distance between the tip and the cell membrane (Figure 1.6). This is because sharpening of the tip results in focusing of the hydrodynamic push/pull force into

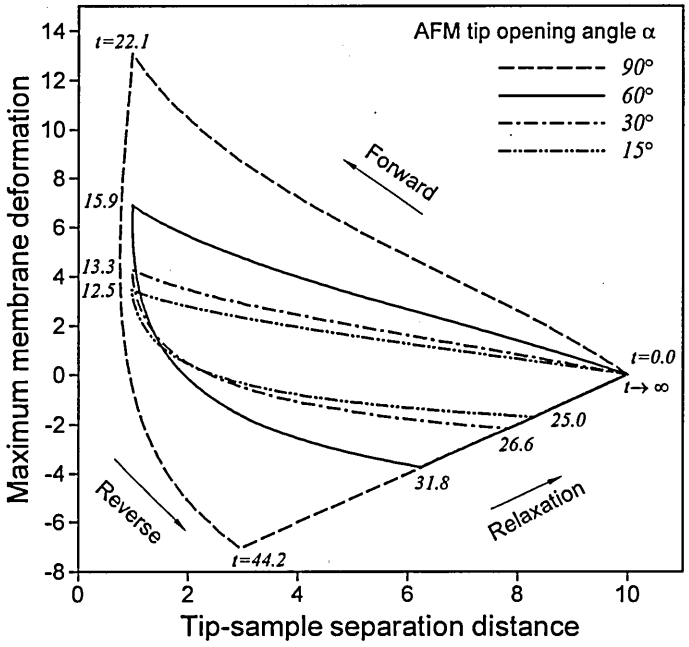

Figure 1.6 Effect of the AFM tip opening angle on the hysteresis curve of the membrane deformation vs. tip-sample separation distance for the membrane with bending rigidity $B = 1.0$ and spontaneous curvature $c_0 = -2.0$.

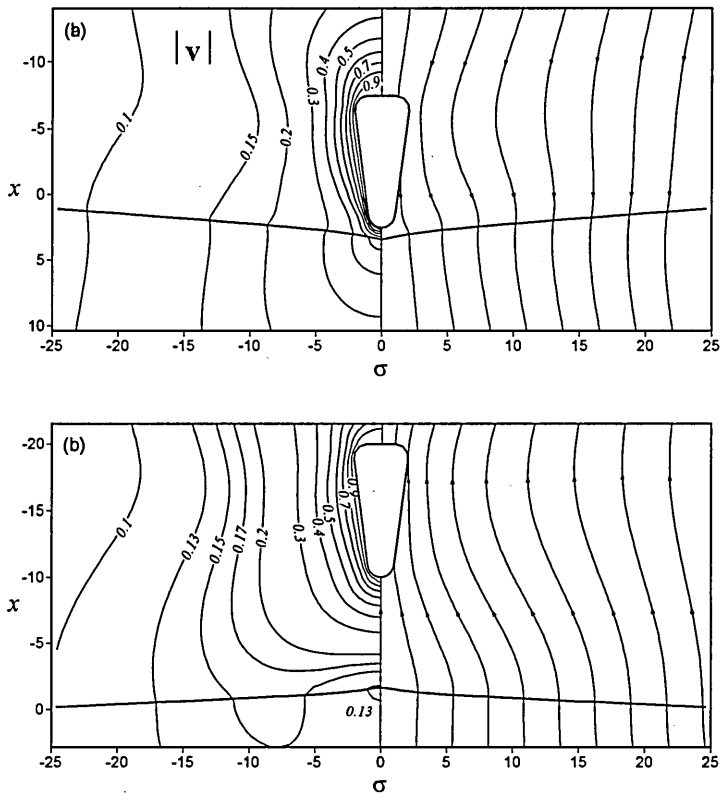

Figure 1.7 Instantaneous normalized velocity contours and streamlines around the AFM tip and the cell membrane at time instants: (a) $t = 12.5$ in the forward direction and (b) $t = 25.0$ in reverse direction for the membrane with bending rigidity $B = 1.0$, spontaneous curvature $c_0 = -2.0$, and the AFM tip with an opening angle $\alpha = 15°$.

a much smaller region of the membrane, as illustrated by a decrease in size of the induced fluid flow domain and, in turn, much greater local velocity gradients in the flow field exemplified by the velocity contours and streamlines in Figure 1.7. In some sense, the effect of tip sharpening (Figure 1.6) is equivalent to an increase in the apparent bending rigidity of the membrane (Figure 1.5), which results in enhanced spatial resolution and sensitivity of the imaging process. Further, the duration of the full probing cycle decreases, thereby allowing for an increase in speed of the membrane scanning process.

Previous studies[28,29] for the elastic properties of giant vesicles indicate that the bending rigidity of the membrane B serves only as a scaling factor for the membrane curvature effect (see eq 1-17), whereas the spontaneous curvature c_0 controls the equilibrium shape of the vesicles. Indeed, the spontaneous curvature represents a phenomenological constant to accommodate various effects due to the asymmetric fluid environment inside and outside of the cell and in the lipid bilayer structure of the membrane. It is obtained by fitting the experiment data of the equilibrium vesicle shape to the curvature elasticity model as shown in Deuling and Helfrich's work.[36] For example, they showed that a red blood cell features a shape of a biconcave disk with negative spontaneous curvatures. Although the elasticity model[36] does not impose any restrictions on the sign of the spontaneous curvature, the positive c_0 is rarely, if ever, found in the experiments. Our simulations show that positive spontaneous curvatures c_0 result in physically unrealistic results, for example, with the bending elastic force further augmenting the hydrodynamic push force in the forward operation mode. Thus, we only present the results for the negative spontaneous curvature by varying c_0 over a broad

range from -0.1 to -5.0, which corresponds to the values found in the experiments with giant vesicles and red blood cells.[29,35,36]

Figure 1.8 shows the hysteresis curves that reflect the effect of the membrane spontaneous curvature. Clearly, with a decrease in an absolute value of c_0, the maximum membrane deformation increases until it reaches the saturation limit at $c_0 \to 0$. The "hysteresis" curves shown in Figure 1.8 exhibit a qualitatively similar behavior to that of the "hysteresis" curves shown in Figure 1.5 which expresses the effect of another elastic constant, the bending rigidity B. Therefore, in practical applications, consolidating these two elastic constants, B and c_0, may provide a basis for the simplified curvature elasticity model to be used as the dynamic boundary condition eq 1-19 for interpretation of AFM images using analytical techniques.

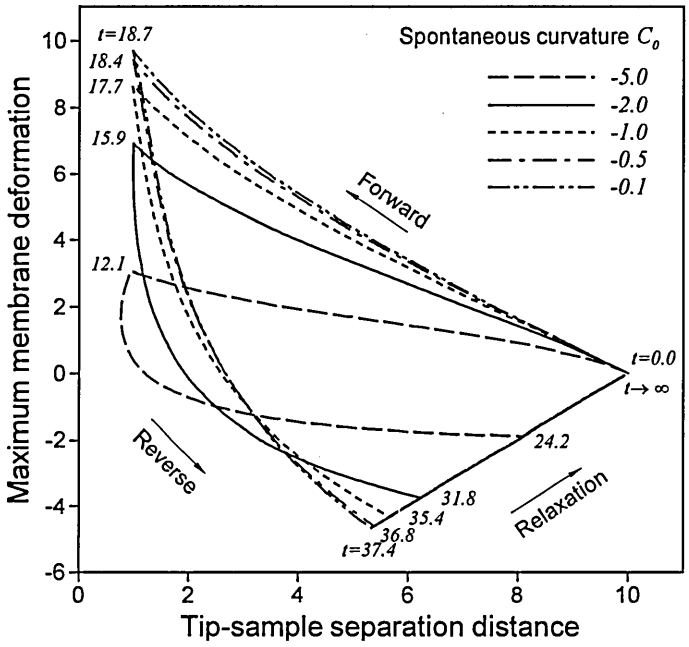

Figure 1.8 Effect of the spontaneous membrane curvature on the hysteresis curve of the membrane deformation vs tip-sample separation distance for the membrane with bending rigidity $B = 1.0$ and the AFM tip with an opening angle $\alpha = 60°$.

1.5 Conclusions

The hydrodynamic interactions during AFM imaging of biological membranes have been investigated through fundamental theoretical analysis and numerical simulations. The model developed couples the Stokes flow induced by an AFM tip motion and the elastic membrane dynamics extended from Helfrich's theory.[11] The governing equations are solved by the boundary element method. In the calculations, the molecular level interactions are disregarded by keeping an AFM tip sufficiently far away from the membrane. The details of the membrane transient deformation and fluid motion (inside and outside of the cell) are described for three probing regimes: forward motion, reverse motion, and relaxation. In each case, a number of interesting and sometimes counterintuitive phenomena were observed such as (a) dominance of the compression force acting on the membrane in the reverse (pull-back) mode of AFM operation even after the membrane passes its equilibrium planar state; (b) a local instantaneous decrease in separation between the AFM tip and the membrane in the beginning of the reverse mode operation when the bending rigidity of the membrane is sufficiently large; (c) the tip parameters (the radius of curvature and the opening angle) define the sensitivity, resolution, and speed of the imaging process; and (d) the probing cycle lasts longer in the case of a softer membrane with smaller bending rigidity and smaller spontaneous curvature as well as when the AFM tip opening angle is large. The "hysteresis" behavior observed in the full cycle noncontact probing experiments using AFM for imaging soft biological samples has been explained by the strong coupling of hydrodynamic effects (fluid motion) and elastic deformation of the membrane when imaging takes place in the liquid environment. The numerical results show that the highest tensile force (scaled by

$V_0\mu$) induced by the fluid motion is of the order of $10^{-3}\,mN/m$, which falls in the range of values measured in the micropipet experiments.[33] The predicted tensile force is also far below the observed rupture tension force $\sim 10\,mN/m$,[33] indicating that the induced viscous stress will not damage the cell membrane.

CHAPTER 2

Electrohydrodynamics and Surface Force Analysis in AFM Imaging of a Charged, Deformable Biological Membrane in a Dilute Electrolyte Solution

Surface forces arising in AFM imaging of a deformable, negatively charged biological membrane in an electrolyte solution are investigated in the limit of continuous electrohydrodynamics. Specifically, the study extends the analysis from the previous chapter of purely hydrodynamic interactions between an AFM tip and the elastic cell membrane by accounting for electric double-layer forces under the assumptions of a dilute electrolyte solution and local electrochemical equilibrium. The solution of the problem is obtained by integrating the quasi-steady, electrically forced Stokes equation for the electrohydrodynamic field, the linearized Poisson-Boltzmann equation for the electrostatic field in the electrolyte inside and outside of the cell, and the Laplace equation for the electrostatic field within a dielectric AFM tip. Helfrich and Zhong-can's equation for an equilibrium shape of the cell membrane is employed as a quasi-steady, nonlinear boundary condition linking the stress fields on both sides of the cell membrane augmented by the local membrane incompressibility condition in order to find the local tension/compression force acting on the membrane. An integrated framework for the dynamic coupling of the membrane double-layer effects and the AFM tip-electrolyte-membrane motion is established that allows for characterizing of the local electrolyte flow field, the electrostatic field, the elastic deformation of the membrane, and the electrohydrodynamic surface force acting on the AFM tip in great detail. The results of the analysis provide information on the motion of the membrane and the surface forces

induced by both an electrolyte motion and the Maxwell stresses resulting from the electric double layer for a full cycle motion of the AFM tip during noncontact, nonresonant mode imaging of a simple cell membrane.

2.1 Introduction

Atomic force microscopy (AFM) provides a unique opportunity to investigate the structure, morphology, micromechanical properties, and biochemical signaling activity of cells, subcell structures, and even a single molecule with high temporal and spatial resolutions. [4,37,38,39,40] In biological applications, AFM imaging of living cells needs to be performed in their natural aqueous environment in order to observe molecular level interactions and biochemical processes in situ in the electrolyte solution and to avoid the interference due to the capillary adhesion forces. Despite significant advances made in experimental application of AFM in cell imaging, the data interpretation and associated theoretical models are still in their infancy. This is perhaps owing to the overwhelming complexity of the physical/chemical phenomena taking place during AFM imaging of flexible, electrochemically active biological samples, which includes intimately coupled fluid flow (inside and outside of the cell), dynamics of the cell membrane deformation, electrokinetics of ionic interactions in the electrolyte, the electric double-layer induced surfaces forces, and other long- and short-range effects. As pointed out by Kamm in his recent review of cellular fluid mechanics,[41] understanding of these interactions is of critical importance because of the key role played by the electrolyte flow conditions in defining the biological functions, normal physiology, and diseases of living cells. In previous chapter, the physical processes taking place during AFM imaging of soft

biological membranes in an aqueous environment were investigated. A particular emphasis was placed on the understanding of hydrodynamic effects in the fluid inside and outside of the cell associated with elastic deformation of the membrane in response to the AFM tapping action for an entire probing cycle. It was also assumed that for an electrolyte with high ionic strength the tip-membrane separation distance is sufficiently large as compared to the thickness of the electric double layer. Thus, the electric double-layer force can be safely neglected in the electrically screened flow domain. In this chapter, the AFM tip-membrane separation distance down to 30 nm is considered in a dilute electrolyte solution. The focus of this chapter is on electrohydrodynamic and elastic interactions between the AFM tip and the cell membrane as observed in noncontact, nonresonant imaging experiments that focus on inferring the local micromechanical properties of biomembranes that are obscured by the dynamic response of the cell (membrane) as a whole.[42] This should not be confused with another important resonant tapping-mode AFM imaging modality commonly used in biological applications, wherein the AFM cantilever is oscillated at the kiloHertz-level resonant frequencies and change in the amplitude or resonant frequency upon interaction with the substrate is used for image interpretation. The problem of hydrodynamic effects relevant to interpretation of the tapping-mode images was successfully attacked by Sader[43] and by the Rajagopalan's group.[44,45] The difference with this study is in two aspects: (1) Sader's and Rajagopalan's works were concerned with the hydrodynamic aspects of fluid-AFM cantilever beam (not a tip) interactions, and (2) their focus was not hydrodynamics, but the effect of fluid damping on the resonance dynamic behavior of the AFM cantilever beam in the tapping mode imaging.

For mammalian cells, the cytoplasm is enclosed by a deformable fluidlike membrane assembled by the lipid bilayers with integrated proteins. Due to the large concentration of charged proteins, the water molecules inside the cell become structured, forming cytosol and making the solution properties inside the cell very different from those of the cell exterior. Such a complex biophysical system is far beyond the reach of current theoretical understanding in the field, especially, in combination with simulation of the instrument and of the imaging process. However, complementary theoretical modeling and experiments are feasible for the simplest "artificial" cell without the space-filled cytoskeleton such as vesicles or artificial synthetic bilayers. The investigation of such simplified systems can provide a significant insight into membrane biomechanics, thereby making the first important step toward basic understanding of the fundamental structure and properties of living cells.

The bending elasticity of the electrically charged lipid bilayers was first studied theoretically by Mitchell and Ninham,[46] Winterhalter and Helfrich,[47] and Chou et al.[48] Experimentally, in the early 1990s, Tao et al.[49] used AFM to measure the local elastic modulus of the hydrated cow tibia, and Radmacher et al.[50] investigated the viscoelastic properties of a living platelet. A summary of more recent work is also available.[5,6,7,51] Typically, the AFM tip force versus separation distance curves generated during AFM imaging experiments are used to determine the micromechanical properties of the cell by fitting the experimental data to the appropriate physical model of the AFM tip-to-sample interactions. Recently, McElfresh et al.[42] used AFM to decouple the mechanical response of the cell from the molecular binding event in order to quantify the local interactions.

Butt[52,53,54] appears to be the first researcher who analyzed the static tip-to-sample interactions by identifying the contribution from the electrostatic, van der Waals, and hydration forces in a quiescent electrolyte solution. A similar solution methodology can also be found in Grant and Saville's study[55] of the particle-rigid plate interactions under various charge conditions of significance to colloidal systems. For a deformable interface, the early work on the dynamic fluid stress induced by the deformation of a free surface by a solid particle was performed by Lee and Leal[21] using the Stokes fundamental solution. More recently, the static equilibrium analysis of the interactions between a charged sphere and a charged monolayer-type interface was reported by Dungan and Hatton[56] who considered the balance of double-layer, gravity, and constant surface tension forces. Although the fluid motion induced by the probing process is observed in most experiments, the analysis becomes rather complex so that most researchers try to eliminate or at least reduce the contribution from the hydrodynamic forces acting on the AFM tip by reducing the probing speed. Only in very recent studies of the flow slip on hydrophilic surfaces, Bonaccurso et al.[57] published measurements with the surface force apparatus which account for the interaction forces due to both hydrodynamic and electric double-layer effects on the solid surface and Vinogradova and Yakubov[58] reported a hydrodynamic force acting on a colloidal probe in a lubrication regime.

These early pioneering works in different areas of colloid and interface sciences as well as the new developments in the area of multifunctional AFM-SECM scanning probes[14,59] provided a stimulus to our study on the pure hydrodynamics of noncontact AFM imaging of a soft biological membrane in an aqueous environment,[1] which is reported in chapter 1. In this chapter, the analysis is extended by considering the effect of

the electric double layer in the coupled AFM tip-electrolyte-membrane system to characterize the local electrolyte flow field, the electrostatic field, the elastic deformation of the membrane, and the surface forces acting on the AFM tip. In this model, the parameters are designed to match the characteristic scales of the above referenced experimental studies.[5,6,7,42] Specifically, we used an AFM tip size equal to 3 μm, and a vertical scanning distance of 500~1000 nm, and the AFM is operated at a low vertical scanning frequency of about 5-10 Hz.

The analysis neglects molecular level interactions and other short-range effects, and is limited to a dilute electrolyte under local electrochemical equilibrium. The minimum tip-to-sample separation distance commonly used in the tapping mode experiments could be an order of magnitude smaller than the value used in the simulations and, at contact, even becomes zero. The reasons for keeping the minimum separation distance greater than 30 nm are as follows. First, the theoretical analysis is based on the "continuum" electrohydrodynamics and elasticity theories and thus is strictly valid for fluid length scales of the order of 30 nm or greater. The discrete nature of surface charges, the details of the protein structures/domains formed within the membrane, and the complex short-range force interactions arising when the AFM tip is in very close proximity to the membrane are beyond the reach of the present model as the "continuum" theory breaks down at such small scales. Second, although the currently available AFM instruments do not allow for control of the tip-to-sample separation distance when imaging soft biological membranes, it ought to be emphasized that, if either the membrane deformation or the tip-to-membrane distance can be measured using an alternative experimental technique (e.g., AFM–scanning near-field optical microscopy (SNOM)

combination), the mathematical relation between the surface force and the membrane deformation developed here may provide a basis for a new noncontact AFM imaging method that avoids the problems of tip contamination and possible cell damage due to the contact with the AFM tip.

The current analysis developed for a dilute electrolyte environment may provide a basis for qualitative interpretation of the AFM studies of electrophysiological properties of real membranes[60,61] or supported artificial membranes wherein the ionic composition of the solution can be varied on both sides of the membrane. For a nondilute electrolyte (e.g., ~0.15 M salt balance inside a typical cell and the buffer solution), the Debye length is very small, less than 1 nm. As a result, the electrostatic field is almost completely screened, there is no electric force acting on the AFM tip until it almost contacts the membrane, and the electric force is no longer coupled to the fluid system. Therefore, to simulate the AFM tip and membrane interactions in a nondilute electrolyte, one can simply modify the phenomenological elastic properties of the membrane to account for various surface charge conditions[46,47] and then model the AFM tip-fluid-membrane interactions using purely hydrodynamic analysis as described in chapter 1.

2.2 Theoretical Development

2.2.1 Scaling and Governing Equations

Figure 2.1 shows a schematic view of the idealized physical arrangement that includes the vertically moving (probing) AFM tip and a biological cell bounded by a charged, deformable membrane and immersed in an electrolyte solution. In the analysis,

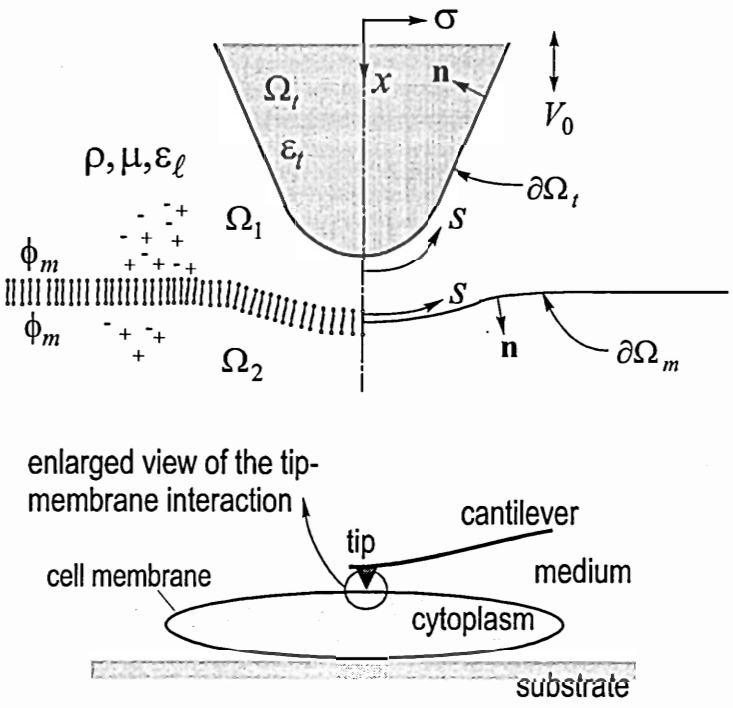

Figure 2.1 Schematic view of an AFM tip approaching a cell membrane and definition of the computational domain.

the representative parameters of the AFM tip and of the noncontact probing process are taken to be 3 μm (the tip height), 30 nm (the tip radius), 300 nm (the initial tip-to-membrane separation distance), and 30 nm (the minimum tip-to-membrane separation distance). An electrolyte solution is characterized by its ionic strength n_c, density ρ, dynamic viscosity μ, and thermal energy k_BT, with k_B and T being the Boltzmann constant and the absolute temperature, respectively. We assume that the AFM tip moves at the piecewise constant probing speed V_0 in the forward and reverse directions defined by the scanning frequency of around 5~10 Hz and the vertical probing distance of around 500~1000 nm. A biological cell is characterized by its equivalent diameter D and the effective membrane bending rigidity B.

A dilute electrolyte features a greater (more diffuse) electric double layer extending further away from the charged membrane surface. As a result, the fluid flow induced by the AFM tip motion may encompass or be encompassed by the double layer during different periods of the AFM probing cycle. Since the focus of the present analysis is on the electrohydrodynamic interactions and the membrane charge double-layer effects, the Debye length of the electric double layer κ^{-1} is chosen as the characteristic dimension for scaling the electrolyte systems with the varying ionic strength. Four time scales can be identified as relevant to the problem in hand. These are as follows:

(i) The forcing velocity time scale, t_{forc}, characterizes the driving force of the fluid motion, and is defined by the ratio of the characteristic length scale, the Debye length κ^{-1}, to the characteristic velocity, V_0, of the vertical probing motion of the AFM tip.

(ii) The viscous diffusion time scale, t_{visc}, characterizes the viscous force induced by the fluid motion, and is defined by the square of the diffusion length across the electric double layer, κ^{-2}, divided by the viscous diffusivity, μ/ρ.

(iii) The ionic migration time scale, t_{mig}, characterizes an accelerated motion of the volumetrically charged fluid element induced by the Coulombic force $\rho_e \mathrm{E} \sim \sum_i z_i e n_i \nabla\phi$ relative to the baseline thermal energy $k_B T/e$ and the bulk ionic strength of the solution $n_c \sim \sum_i z_i^2 n_i^\infty$. In other words, the time scale is derived from the following balance equation $\rho_e \mathbf{E} \sim \sum_i z_i e n_i \nabla\phi \sim \kappa n_c k_B T$, where ρ_e is the volumetric charge density, $\mathbf{E}$ is the local electric field, z_i is the valence number, e is the single electron charge, and n_i is the number density of each ionic species. Note that such a scaling is consistent with the result obtained by the linear approximation of the charge density.

(iv) The simplified membrane bending relaxation time scale without considering the fluid resistance, t_{bend}, characterizes the accelerated motion of the membrane driven by the bending elasticity, and is defined by the bending rigidity B, the judiciously selected cell diameter D (used instead of κ^{-1} for the length scale), and a representative total volume based on the selected length scale for the cell diameter, D^3.

In summary, the four corresponding time scales are expressed as

$$t_{forc} \sim (\kappa V_0)^{-1}, \quad t_{visc} \sim \rho/(\kappa^2 \mu), \quad t_{mig} \sim (\rho/\kappa^2 n_c k_B T)^{1/2}, \quad t_{bend} \sim (\rho D^5/B)^{1/2} \qquad (2\text{-}1)$$

For the typical values of $V_0 = 10^{-5} m/s$, $n_c = 10^{-6} M \sim 10^{-4} M$ and $\kappa^{-1} = 300 \sim 30 nm$, the forcing time scale is of the order of $10^{-2} \sim 10^{-3} s$. For the electrolyte properties, $\rho \sim 10^3 kg/m^3$ and $\mu \sim 1.5 \times 10^{-3} kg/m \cdot s$ at room temperature, the viscous diffusion time scale is of the order of $10^{-8} \sim 10^{-10} s$, and the ionic migration time scale is of the order of $10^{-6} \sim 10^{-8} s$. For a cell whose representative diameter is greater than the height of the AFM tip, for example, a 10 μm cell, and a nominal bilayer bending rigidity of $2 \times 10^{-19} J$,[32,34] the membrane bending relaxation time scale is of the order of $10^{-2} s$. Therefore, if we focus on the dynamic effects associated with forced motion of the AFM tip, the characteristic time scale for the problem t_{char} should be given by the forcing velocity time scale t_{forc} and the following scale hierarchy can be established,

$$t_{char} = t_{forc} \sim t_{bend} >> t_{mig} > t_{visc} \tag{2-2}$$

The comparison of time scales in eq 2-2 clarifies some key time-domain limitations of the present analysis: (i) the selected forcing time scale resolves the effects resulting from the AFM tip motion as well as the membrane deformation induced by the fluid flow; (ii) the viscous time scale is much smaller than the characteristic forcing time scale which supports the quasi-steady approach to the analysis of the fluid motion (i.e., a vanished time derivative term in the Navier-Stokes equations) because the viscous diffusion affects flow on a much shorter time scale than that of the AFM tip motion; and (iii) the much smaller ionic migration time scale, as compared to the characteristic forcing time scale, implies that the local electrochemical equilibrium can be assumed to exist in the electrolyte solution. Further, owing to the very low Reynolds number, $\mathrm{Re} = \rho V_0 / \kappa\mu \sim 10^{-6}$ to 10^{-7}, the flow inertial forces are negligibly small as compared to the viscous forces

and, thus, the nonlinear advection term in the Navier-Stokes equations can be also dropped.

We consider a homogeneous electrolyte with uniform electrical and fluid properties on both sides of the cell membrane, whose surface potential or charge density is assumed uniform and described by a symmetric value of the zeta potential. The short-range structural, hydration, van der Waals, and other molecular level interactions are neglected as compared to the electric force acting on the AFM tip when it penetrates into the charged double layer of the membrane down to the minimum tip-to-membrane separation distance of about 30 nm. It is also assumed that the AFM tip is made of a dielectric material, for example, silicon nitride, both the environment fluid and the fluid inside the cell are incompressible Newtonian fluids with the same density and viscosity, and the Coulombic electric force is the only body force involved in the probing process. The membrane thickness is neglected so the membrane can be mathematically treated as an infinitesimally thin interface. Thermal fluctuations due to Brownian motion are assumed to be insignificant to perturb a sufficiently rigid cell membrane from its perfectly smooth and, initially, equilibrium flat shape. Further, the interior of the cell is assumed electrochemically isolated from the exterior environment without considering any ion transport across the cell membrane.

The dynamics of both fluids, i.e., inside (Ω_2-domain) and outside (Ω_1-domain) of the cell (Figure 2.1), is governed by the steady-state, electrically forced nonhomogeneous Stokes equation and the continuity equation:

$$-\nabla p + \mu \nabla^2 \mathbf{v} + \rho_e \mathbf{E} = 0, \quad \mathbf{x} \in \Omega_1, \Omega_2 \tag{2-3}$$

$$\nabla \cdot \mathbf{v} = 0, \quad \mathbf{x} \in \Omega_1, \Omega_2 \tag{2-4}$$

where p, $\mathbf{v}$, and μ are the pressure field, the velocity field, and the dynamic viscosity, respectively, ρ_e is the local volumetric charge density, $\mathbf{E}$ is the electric field vector related to the electric potential ϕ by $\mathbf{E}=-\nabla\phi$, and $\mathbf{x}$ denotes a position vector in the Cartesian coordinate system. The charged membrane induces an electric field in the electrolyte solution, which is screened by the electric double layer and also coupled to the electric field within the AFM tip through the electric boundary conditions. Applying Gauss' Law leads to the Poisson equation for the electric potential in the electrolyte environment,

$$\nabla^2\phi=\frac{-\rho_e}{\varepsilon_\ell\varepsilon_0}, \quad \mathbf{x}\in\Omega_1,\Omega_2 \tag{2-5}$$

where ε_ℓ is the electrolyte relative permittivity, and ε_0 is the permittivity of a vacuum, and to the Laplace equation for the electric potential distribution in the dielectric AFM tip which has no free or fixed charges inside,

$$\nabla^2\phi=0, \quad \mathbf{x}\in\Omega_t \tag{2-6}$$

where the Ω_t domain indicates the dielectric material of the AFM tip (Figure 2.1). Recall that the scale relationship given by eq 2-2 permits us to use the local electrochemical equilibrium since the ion relaxation occurs on a much shorter time scale than the characteristic forcing time scale based on the AFM tip probing speed. The local electrochemical equilibrium condition for a dilute system leads to the nonlinear Poisson-Boltzmann equation owing to a nonlinear dependence of the charge density on the electric field potential in eq 2-5.[62] To facilitate the complete integral solution of the problem, only a simple case of the Debye-Hückel linear approximation[63] is considered for a system with a small electric potential, $|\phi|<<k_BT/e\sim 25mV$ at 25°C, where e is a

single electron charge. This linear approximation reduces the volumetric charge density to

$$\rho_e(\mathbf{x}) \sim (-2e^2 n_c / k_B T)\phi(\mathbf{x}) \tag{2-7}$$

By substituting eq 2-7 into eqs 2-3 and 2-5, the nonhomogeneous Stokes equation is obtained, expressed as

$$-\nabla p + \mu\nabla^2 \mathbf{v} + \varepsilon\varepsilon_0\kappa^2\phi\nabla\phi = 0, \quad \mathbf{x} \in \Omega_1, \Omega_2 \tag{2-8}$$

and the linearized Poisson-Boltzmann equation becomes

$$\nabla^2\phi = \kappa^2\phi, \quad \mathbf{x} \in \Omega_1, \Omega_2 \tag{2-9}$$

where the Debye length κ^{-1} is related to the ionic strength n_c by

$$\kappa = \sqrt{2e^2 n_c / \varepsilon_\ell \varepsilon_0 k_B T} \tag{2-10}$$

The dynamic boundary condition at the membrane interface can be obtained from the stress balance on both sides of the membrane.[25] We assume that the membrane deformation is dominated by its bending rigidity and the fluidlike membrane has locally isotropic surface tension on the time scale of interest and has negligible shear elasticity.[1] Under these conditions, the quasi-steady stress balance for the cell membrane can be expressed as

$$\left(\boldsymbol{\tau}_2^{eh} \cdot \mathbf{n} - \boldsymbol{\tau}_1^{eh} \cdot \mathbf{n}\right) + \nabla_s \gamma - \gamma \mathbf{n}(\nabla_s \cdot \mathbf{n}) + \mathbf{f}_1^M + \mathbf{f}_2^M = 0 \tag{2-11}$$

where $\Delta\mathbf{f}^{eh} = \boldsymbol{\tau}_2^{eh} \cdot \mathbf{n} - \boldsymbol{\tau}_1^{eh} \cdot \mathbf{n}$ is the surface force jump condition induced by the electrohydrodynamic stresses from the adjacent fluids, and $\nabla_s \gamma - \gamma \mathbf{n}(\nabla_s \cdot \mathbf{n})$ is defined by the membrane geometry including the shear component given by the surface tension gradient in the tangential direction $\mathbf{s}$ of the membrane and the normal component given by Helfrich and Zhong-can's membrane mechanics and the equilibrium shape equation.[11,

[12,26,28] The last two terms $\mathbf{f}_1^M + \mathbf{f}_2^M$ are added to account for the electrostatic force induced by the asymmetric (relative to the membrane) electric screening fields on both sides of the membrane. The electric force is computed from the Maxwell electric stress tensor $\boldsymbol{\tau}^M$ as a function of the local electric field,[64]

$$\mathbf{f}^M = \boldsymbol{\tau}^M \cdot \mathbf{n} = \varepsilon_\ell \varepsilon_0 \left(\mathbf{EE} - \frac{1}{2}\mathbf{E} \cdot \mathbf{E}\boldsymbol{\delta} \right) \cdot \mathbf{n} \tag{2-12}$$

where the term in front of the Kronecker delta ($\boldsymbol{\delta}$) denotes the isotropic component of the electric stress tensor. Using Helfrich and Zhong-can's membrane equilibrium shape equation, eq 2-11 can be rearranged[1] to the following jump condition suitable for the integral formulation of the problem described in the next section:

$$\Delta \mathbf{f}^{eh} = -\nabla_s \gamma - \Delta \mathbf{f}^M + \left(-2\gamma H + B(2H + c_0)(2H^2 - 2K - c_0 H) + 2B\nabla^2 H \right) \mathbf{n} \tag{2-13}$$

where γ is the local tension force, B is the apparent bending rigidity, H is the mean curvature, K is the Gaussian curvature, c_0 is the effective spontaneous curvature, ∇^2 is the Laplace-Beltrami operator for the curvilinear surface, ∇_s is a surface gradient operator, and $\Delta \mathbf{f}^M = \mathbf{f}_1^M + \mathbf{f}_2^M = \boldsymbol{\tau}_2^M \cdot \mathbf{n} - \boldsymbol{\tau}_1^M \cdot \mathbf{n}$ is the net electric force applied to the membrane due to the asymmetric electric fields in the electrolyte on both sides of the membrane. Note that the normal direction $\mathbf{n}$ follows the definition in Figure 2.1, and the mean and Gaussian curvatures can be transformed into parametric forms in terms of the derivatives of the axisymmetric coordinates (x, σ) with respect to the arc-length coordinate s along the membrane interface $\partial\Omega_m$ as $H = \left[x' - \sigma\sigma'' x' + \sigma\sigma' x'' \right] / 2\sigma$ and $K = \left[\sigma' x' x'' - \sigma'' x'^2 \right] / \sigma$. Further, since the local tension force γ is not known a priori in the dynamic boundary condition, eq 2-13, an additional equation needs to be introduced

based on the membrane surface area constraint condition, $\partial(dA)/\partial t = 0$, to complete the formulation. The general form of the constraint equation for a locally incompressible membrane was first derived by Pozrikidis[30] for the deformation of a red blood cell in the shear flow, and it can be expressed in terms of the arc-length coordinate with the local surface tangent $\hat{\mathbf{t}}_s(\mathbf{x} \in \partial\Omega_m)$:

$$\sigma \hat{\mathbf{t}}_s \cdot \frac{\partial \mathbf{v}}{\partial s} + \mathbf{v} \cdot \hat{\mathbf{e}}_\sigma = 0 \tag{2-14}$$

To generalize the formulation, the governing equations are made dimensionless by the following scales: the length scale is given by the Debye length κ^{-1}, velocity the $\mathbf{v}$ is scaled by the AFM tip approach speed V_0, time is scaled by the characteristic forcing time $t_{forc} = (\kappa V_0)^{-1}$, the local surface tension γ is scaled by $V_0\mu$, the membrane bending rigidity B is scaled by $V_0\mu/\kappa^2$, the membrane mean curvature H and spontaneous curvature c_0 are both scaled by the inverse of the Debye length κ, the Gaussian curvature K is scaled by κ^2, the surface force f and pressure p are both scaled by $V_0\mu\kappa$, and the electric potential ϕ is scaled by ζ $(\zeta = k_B T/e)$. Using these scales, the following dimensionless governing equations can be derived:

$$-\nabla p + \nabla^2 \mathbf{v} + \alpha\phi\nabla\phi = 0, \quad \nabla \cdot \mathbf{v} = 0 \quad \text{for } \mathbf{x} \in \Omega_1, \Omega_2 \tag{2-15}$$

$$\nabla^2 \phi = \phi, \quad \mathbf{x} \in \Omega_1, \Omega_2 \tag{2-16}$$

$$\nabla^2 \phi = 0, \quad \mathbf{x} \in \Omega_t \tag{2-17}$$

where the dimensionless parameter α measures the relative strength of the electric force as compared to the viscous force in the electrolyte solution (provided, of course, $\phi\nabla\phi \sim O(1)$ and the scale for the surface potential is ζ):

$$\alpha = \frac{\varepsilon_\ell \varepsilon_0 \kappa \zeta^2}{\mu V_0} \sim \frac{electric\ force}{viscous\ force} \tag{2-18}$$

And the dimensionless Maxwell surface force, eq 2-12, can be reduced to a function of the local potential field,

$$f_i^M = \alpha\left(\frac{\partial\phi}{\partial x_i}\frac{\partial\phi}{\partial n} - \frac{1}{2}\frac{\partial\phi}{\partial x_k}\frac{\partial\phi}{\partial x_k}n_i\right) \tag{2-19}$$

The dynamic interface boundary condition, eq 2-13, and the membrane surface area constraint equation, eq 2-14, remain in the same form after being made dimensionless. Finally, the system of governing dimensionless equations is complemented by the following boundary conditions, in dimensionless forms:

$\mathbf{v}(\mathbf{x}) = \pm 1\hat{\mathbf{e}}_x, \quad \mathbf{x} \in \partial\Omega_t$ no slip condition on the AFM tip (2-20)

$\mathbf{v}(\mathbf{x}) = \mathbf{v}_m(\mathbf{x}), \quad \mathbf{x} \in \partial\Omega_m$ no slip condition on the cell membrane (2-21)

$\mathbf{v}(\mathbf{x}) = 0, \quad |\mathbf{x}| \to \infty$ velocity field vanishes at the infinity (2-22)

$\phi(\sigma, x) = 0, \quad x \to \pm\infty$ electric potential field vanishes at the infinity (2-23)

$\phi_1(\mathbf{x}) = \phi_2(\mathbf{x}) = \phi_m, \quad \mathbf{x} \in \partial\Omega_m$ symmetrically charged membrane (2-24)

$\phi_1(\mathbf{x}) = \phi_t(\mathbf{x}), \quad \mathbf{x} \in \partial\Omega_t$ continuity of the electric field on the AFM tip (2-25)

$\varepsilon_r \nabla\phi_t(\mathbf{x}) \cdot \mathbf{n}(\mathbf{x}) = \nabla\phi_1(\mathbf{x}) \cdot \mathbf{n}(\mathbf{x}), \quad \mathbf{x} \in \partial\Omega_t$ continuity of the potential flux on the AFM tip (2-26)

where the relative (AFM tip material to environment electrolyte) dielectric constant is defined by $\varepsilon_r = \varepsilon_t / \varepsilon_\ell$. Several assumptions are made in the boundary conditions to simplify the system: (i) the AFM tip approach speed is piecewise constant during the imaging process; (ii) the apparent electric potential of the membrane is small, $|\phi| << \zeta$, so that the Poisson-Boltzmann equation can be linearized; (iii) the charged molecules and

polar groups of the lipid molecules uniformly smear out along the surface to maintain constant zeta potentials[65] on both sides of the membrane, and the membrane is initially in its equilibrium flat shape; (iv) the AFM tip has zero surface charge density.

2.2.2 Boundary Integral Formulation

The model equations are intimately coupled and solved by the boundary integral method.[13,66] According to Ladyzhenskaya,[19] the general integral solution of the nonhomogeneous Stokes equation, $-\nabla p+\nabla^2\mathbf{v}=\mathbf{S}$, can be written as a combination of contributions from the Stokeslet, the Stresslet, and the nonhomogeneous source term,

$$\omega v_j(\mathbf{x}_0) = -\int_{\Omega} S_i(\mathbf{x})G_{ij}(\mathbf{x},\mathbf{x}_0)\,dV(\mathbf{x}) - \int_{\partial\Omega} \tau_{ik}(\mathbf{x})n_k(\mathbf{x})G_{ij}(\mathbf{x},\mathbf{x}_0)\,dA(\mathbf{x}) + \overset{p.v.,\,\mathbf{x}_0\in\partial\Omega}{\int_{\partial\Omega}} v_i(\mathbf{x})T_{ijk}(\mathbf{x},\mathbf{x}_0)n_k(\mathbf{x})\,dA(\mathbf{x}) \tag{2-27}$$

where $\omega=0$ for $\mathbf{x}_0\notin\Omega$, $\omega=8\pi$ for $\mathbf{x}_0\in\Omega-\partial\Omega$, and $\omega=4\pi$ for $\mathbf{x}_0\in\partial\Omega$ on the sufficiently smooth boundary. On the right-hand side of eq 2-27, the first term is a volume integral, and the second and third terms are the single-layer and the double-layer surface integrals. The unit surface normal vector n_k points into the fluid domain, $S_i=-\alpha\phi\nabla\phi$ represents the vector source term due to the electric force in eq 2-15, and v_i and τ_{ik} represent the velocity and electrohydrodynamic stress fields, respectively. Note that when the source point is located at the boundary, $\mathbf{x}_0\in\partial\Omega$, the double-layer contribution from the Stresslet has to be interpreted in the sense of Cauchy principal value because of the stronger singularity in the integral kernel T_{ijk}. The fundamental solution, the Stokeslet, and its corresponding stress field, the Stresslet, are given for the solution of the homogeneous Stokes system, $-\nabla p+\nabla^2\mathbf{v}=0$,[13]

$$G_{ij}(\mathbf{x},\mathbf{x}_0)=\frac{\delta_{ij}}{r}+\frac{r_i r_j}{r^3},\quad T_{ijk}(\mathbf{x},\mathbf{x}_0)=-6\frac{r_i r_j r_k}{r^5} \tag{2-28}$$

respectively, where δ_{ij} is the Kronecker delta function, and $\mathbf{r}=\mathbf{x}\text{-}\mathbf{x}_0$ and $r=|\mathbf{x}\text{-}\mathbf{x}_0|$ are the position vector and the distance between the field and the source points, respectively. To facilitate the advantages of the boundary integral only formulation, the domain integral of the source term $S_i=-\alpha\phi\nabla\phi$ is transformed into the surface integral by incorporating the divergence free property of the Stokeslet,

$$\nabla\cdot G_{ij}=0 \tag{2-29}$$

so that

$$\int_\Omega \phi\frac{\partial\phi}{\partial x_i}G_{ij}\,dV=\frac{1}{2}\int_\Omega \nabla\cdot\left(\phi^2 G_{ij}\right)dV \tag{2-30}$$

Then, by applying the divergence theorem to the right-hand side of eq 2-30, the complete boundary integral formulation of eq 2-15 can be obtained,

$$\omega v_j=-\frac{\alpha}{2}\int_{\partial\Omega}\phi^2 G_{ij}\,n_i dA-\int_{\partial\Omega} f_i^{eh}G_{ij}\,dA+\int_{\partial\Omega} v_i T_{ijk}\,n_k dA \tag{2-31}$$

with $\mathbf{n}$ pointing into the fluid domain and the traction term replaced by the surface force expression, $f_i^{eh}=\tau_{ik}^{eh}n_k$. It can be proven[1,20,21] that for a symmetric and uniformly charged membrane, the boundary integral solution (eq 2-31) in both fluid domains (i.e., inside and outside of the cell) can be effectively combined using the dynamic interface boundary condition (eq 2-13) leading to the following unified formulation:

$$\omega v_j=-\int_{\partial\Omega_m}\Delta f_i^{eh}G_{ij}\,dA+\int_{\partial\Omega_t}\left(f_i^{eh}+\frac{\alpha}{2}\phi_t^2 n_i\right)G_{ij}dA-\overset{p.v.,\,\mathbf{x}_0\in\partial\Omega_t}{\int_{\partial\Omega_t}} v_i T_{ijk}n_k dA \tag{2-32}$$

where $\omega=8\pi$ for $\mathbf{x}_0\in\Omega_1+\Omega_2+\partial\Omega_m$, and $\omega=4\pi$ for $\mathbf{x}_0\in\partial\Omega_t$. The surface force jump condition Δf_i^{eh}, given by eq 2-13, in the kernel function can be interpreted as the source

density acting on the fluid from the cell membrane surface, and ϕ_t is the induced local surface potential at the AFM tip.

If the AFM tip, the cell membrane, and the induced flow are axisymmetric, the complexity of the integral formulations can be further reduced by using the cylindrical coordinate system $(x, y, z) = (x, \sigma\cos\theta, \sigma\sin\theta)$ and expressing the fundamental solutions, the Stokeslet and the Stresslet, in terms of Green's functions of the ring source type. As shown in Figure 2.1, x is the coordinate along the axial direction, σ is the coordinate along the radial direction, and θ is the azimuthal angle. Similar to the analysis in chapter 1, Δf_i^{eh}, f_i^{eh}, and v_i are independent of the azimuthal angle so that the azimuthal integration needs to be performed only for Green's function and for its corresponding stress field leading to the final solution of the three-dimensional axisymmetric problem in terms of one-dimensional integrals only,

$$\omega v_\alpha = -\int_{\partial\Omega_m} \Delta f_\beta^{eh} M_{\alpha\beta}\, ds + \int_{\partial\Omega_t} \left(f_\beta^{eh} + \frac{\alpha}{2}\phi_t^2 n_\beta \right) M_{\alpha\beta}\, ds - \overset{p.v.,\ \mathbf{x}_0\in\partial\Omega_t}{\int_{\partial\Omega_t}} Q_{\alpha\beta\gamma}\, v_\gamma\, n_\beta ds \qquad (2\text{-}33)$$

where ω has been defined for eq 2-32, the Greek symbols α, β and γ denote either x or σ directions, and the kernel functions $M_{\alpha\beta}$ and $Q_{\alpha\beta\gamma}$ are the general coordinate transformation matrixes for the Stokeslet and the Stresslet in the Cartesian coordinate system,[13,21] which can be expressed in terms of the complete elliptic integrals of the first and second kinds. Now, by substituting eq 2-33 into eq 2-14, the integral formulation of the local membrane constraint equation, including the hydrodynamic and electric effects, takes its final compact form,

$$\int_{\partial\Omega_m} \Delta f_\beta^{eh}(\mathbf{x})\Pi_1(\mathbf{x}, \mathbf{x}_0) ds(\mathbf{x}) - \int_{\partial\Omega_t} \left(f_\beta^{eh} + \frac{\alpha}{2}\phi_t^2 n_\beta \right) \Pi_1\, ds + \overset{p.v.,\ \mathbf{x}_0\in\partial\Omega_t}{\int_{\partial\Omega_t}} \Pi_2\, v_\gamma n_\beta ds = 0 \qquad (2\text{-}34)$$

with the integral kernels expressed as

$$\Pi_1(\mathbf{x},\mathbf{x}_0)=\sigma(\mathbf{x}_0)\hat{t}_\alpha(\mathbf{x}_0)\frac{\partial M_{\alpha\beta}(\mathbf{x},\mathbf{x}_0)}{\partial s(\mathbf{x}_0)}+M_{\sigma\beta}(\mathbf{x},\mathbf{x}_0) \tag{2-35}$$

$$\Pi_2(\mathbf{x},\mathbf{x}_0)=\sigma(\mathbf{x}_0)\hat{t}_\alpha(\mathbf{x}_0)\frac{\partial Q_{\alpha\beta\gamma}(\mathbf{x},\mathbf{x}_0)}{\partial s(\mathbf{x}_0)}+Q_{\sigma\beta\gamma}(\mathbf{x},\mathbf{x}_0) \tag{2-36}$$

where α, β and γ denote either the σ or x directions, and the unknown local membrane tension/compression force is obtained implicitly from $\Delta\mathbf{f}^{eh}$ given by eq 2-13. The tangential derivatives of $M_{\alpha\beta}$ and $Q_{\alpha\beta\gamma}$ can also, in principle, be expressed in terms of the complete elliptic integrals of the first and second kinds. However, such a derivation is quite cumbersome, so in simulations the finite difference technique is used to compute these terms.

The linearized Poisson and Laplace equations for the electric field potentials can also be transformed into the integral formulation by using the weighted residual method and the general Green's identity. The adjoint integral forms of eqs 2-16 and 2-17 are identical and can be expressed as

$$\omega_P\phi=\int_{\partial\Omega}\left(G_P\frac{\partial\phi}{\partial n}-\phi\frac{\partial G_P}{\partial n}\right)dA \tag{2-37}$$

$$\omega_L\phi=\int_{\partial\Omega}\left(G_L\frac{\partial\phi}{\partial n}-\phi\frac{\partial G_L}{\partial n}\right)dA \tag{2-38}$$

where $\omega_P=1$ for $\mathbf{x}_0\in\Omega_1,\Omega_2$, $\omega_P=1/2$ for $\mathbf{x}_0\in\partial\Omega_t,\partial\Omega_m$, $\omega_L=1$ for $\mathbf{x}_0\in\Omega_t$, and $\omega_L=1/2$ for $\mathbf{x}_0\in\partial\Omega_t$. Note that the coefficient value 1/2 is valid only for a smooth boundary. The fundamental solutions of the adjoint differential operators ∇^2-1 and ∇^2 in eqs 2-16 and 2-17, respectively, can be derived by the Fourier transform technique and are given by:

$$G_P=e^{-r}/4\pi r \tag{2-39}$$

$$G_L = 1/4\pi r \tag{2-40}$$

where $r = |\mathbf{x}\text{-}\mathbf{x}_0|$ is the distance between the source and field points. Similar to the Stokes flow problem, the surface integrals in eqs 2-37 and 2-38 can be reduced to the one-dimensional line integrals by transforming the Cartesian coordinates to the cylindrical coordinates,

$$\omega_P \phi = \int_{\partial\Omega} \left(M_P \frac{\partial \phi}{\partial n} - \phi Q_P \right) ds \tag{2-41}$$

$$\omega_L \phi = \int_{\partial\Omega} \left(M_L \frac{\partial \phi}{\partial n} - \phi Q_L \right) ds \tag{2-42}$$

where ω_P and ω_L are the same as those defined for eq 2-37 and 2-38, and the ring source type Green's function (M_P) and its normal gradient (Q_P) for the Poisson equation can be expressed in terms of compact forms,

$$M_P = \sigma \int_0^{2\pi} G_P \, d\theta = \frac{\sigma k}{2\pi(\sigma\sigma_0)^{1/2}} J_{10} \tag{2-43}$$

$$Q_P = \sigma \int_0^{2\pi} \frac{\partial G_P}{\partial n} d\theta = \frac{n_\sigma k^2}{4\pi} \left(\frac{k}{2(\sigma\sigma_0)^{1/2}} J_{31} + J_{21} \right) - \frac{(\hat{x} n_x + \sigma n_\sigma) k^2}{4\pi\sigma_0} \left(\frac{k}{2(\sigma\sigma_0)^{1/2}} J_{30} + J_{20} \right) \tag{2-44}$$

respectively, where $\hat{x} = x - x_0$, $k = \sqrt{4\sigma\sigma_0 / \left(\hat{x}^2 + (\sigma + \sigma_0)^2\right)}$, the field and source point locations are defined by $\mathbf{x} = (x, \sigma)$ and $\mathbf{x}_0 = (x_0, \sigma_0)$, respectively, and the integral J_{mn} is defined by

$$J_{mn} = \int_0^{\pi/2} \frac{e^{-\sqrt{\left(\hat{x}^2 + (\sigma+\sigma_0)^2\right)\left(1 - k^2 \cos^2\theta\right)}} \cdot \left(2\cos^2\theta - 1\right)^n}{\left(1 - k^2 \cos^2\theta\right)^{m/2}} d\theta \tag{2-45}$$

Equation 2-45 cannot be integrated analytically or transformed into a simplified form using the elliptic integrals, so it is necessary to divide the integral into two parts: the first

part, which includes the singular point when $k \to 1$ and $\theta \to 0$, can be asymptotically expanded into a series in terms of the azimuthal angle as a small parameter, and the second part can be calculated by direct numerical integration. Similarly, for the Laplace equation, the ring source type Green's function (M_L) and its normal gradient (Q_L) are

$$M_L = \sigma \int_0^{2\pi} G_L \, d\theta = \frac{\sigma}{4\pi} I_{10} \tag{2-46}$$

$$Q_L = \sigma \int_0^{2\pi} \frac{\partial G_L}{\partial n} d\theta = -\frac{\sigma \hat{x}}{4\pi} I_{30} n_x + \left(\frac{\sigma \sigma_0}{4\pi} I_{31} - \frac{\sigma^2}{4\pi} I_{30} \right) n_\sigma \tag{2-47}$$

respectively, where the integrals I_{ij} are derived from the Integral Tables[67] and expressed in terms of the complete elliptic integrals of the first and second kinds, listed in Appendix C. Note that the surface integrals in eqs 2-41 and 2-42 cannot be arbitrarily truncated since the membrane surface potential does not vanish when $\sigma \to \infty$. Therefore, in the construction of the computational domain used in numerical simulations, an imaginary, infinitely long cylindrical wall (or tube) is placed vertically around the system, with a radius defined by an appropriate truncation distance, about ten folds of total height of the AFM tip. The boundary condition at the imaginary wall is that of a vanishing gradient for all scalar quantities along the surface normal. The electric potential should also vanish in the axial direction as $x \to \pm\infty$. In addition, the required gradient of the potential field in eq 2-19 can be derived by taking the derivative of the integral solution given by eq 2-41, although this would increase the kernel singularity and further complicate the numerical integration. An alternative way to overcome this difficulty is to use the invariant coordinate system transformation defined by $\nabla\phi = \frac{\partial \phi}{\partial x}\hat{\mathbf{e}}_x + \frac{\partial \phi}{\partial \sigma}\hat{\mathbf{e}}_\sigma = \frac{\partial \phi}{\partial n}\mathbf{n} + \frac{\partial \phi}{\partial s}\hat{\mathbf{t}}_s$ in order to obtain the gradients $\partial\phi/\partial x$ and $\partial\phi/\partial\sigma$. The normal gradient $\partial\phi/\partial n$ can be computed

through the integral solution of eq 2-41, and $\partial\phi/\partial s$ can be calculated using the finite difference technique. Then, the gradients $\partial\phi/\partial x$ and $\partial\phi/\partial\sigma$ can be computed from $\partial\phi/\partial n$ and $\partial\phi/\partial s$ by using the rotation matrixes:

$$\begin{bmatrix} n_x & -n_\sigma \\ n_\sigma & n_x \end{bmatrix} \text{ for } \mathbf{x} \in \partial\Omega_m, \quad \begin{bmatrix} n_x & n_\sigma \\ n_\sigma & -n_x \end{bmatrix} \text{ for } \mathbf{x} \in \partial\Omega_t \tag{2-48}$$

In summary, we have developed the system of linear integral equations, eqs 2-33, 34, 41, and 42, that, combined with the boundary conditions, eqs 2-20 to 26, and the nonlinear membrane boundary condition, eq 2-13, constitute the boundary value problem for the coupled electric field/fluid flow/membrane deformation problem describing the dynamics of the noncontact AFM imaging process of the biological membrane. The system is solved numerically using the boundary element method with discretization along the surface of the AFM tip and the cell membrane. Note that the electric field governed by eqs 2-41 and 2-42 is essentially uncoupled from the fluid system, and can be solved once the moving membrane/tip boundaries are advanced to the next time step through the Euler time integration method using the velocity field at every collocation point. The details of the numerical implementation for the fluid system are discussed in chapter 1, and, therefore, not repeated here.

2.3 Results and Discussion

The total force acting on the AFM tip is due to: (i) the electrohydrodynamic stress owing to the electrically (Coulombic force) driven fluid motion, and (ii) the Maxwell stress generated by the electric field in the vicinity of the AFM tip induced by the charged biomembrane. The first part is obtained by direct integration of the integral solution, $\mathbf{f}^{eh}$ of eq 2-33, along the surface boundary of the AFM tip. The second part, contributed by the Maxwell stress field, $\mathbf{f}^{M}$ of eq 2-19, is also obtained by surface integration after the potential field of eq 2-41 is computed. We demonstrate the results for a dilute solution with variable ionic strength from $n_c^{\infty} = 10^{-6} M$ to $10^{-4} M$ for a fixed AFM tip geometry and membrane elastic properties. The axisymmetric AFM tip geometry is characterized by a total height of 3 μm, a radius of the upper corner 0.3 μm, a tip opening angle of 60°, a front radius of the tip of 30 nm, and the nominal membrane bending rigidity and spontaneous curvature $B = 2 \times 10^{-19} J$ and $c_0 = -4.0 \mu m^{-1}$, respectively. The tip moves at a piecewise constant vertical scanning velocity of ±10 μm/s, and is initially placed at a distance 300 nm above the membrane whose equilibrium position is given by $x = 0$. The reversing point of the scanning process is set to 30 nm as the minimum tip-to-membrane separation distance. The relative dielectric constant, $\varepsilon_r = 0.075$, and the dimensionless small membrane zeta potential, $\phi_m = -0.5$, are maintained constant. Other dimensionless parameters used in simulations are listed in the caption of Figure 2.2. The boundary element method is implemented using a total of 70 and 60 elements along the tip and the membrane surface, respectively. The numerical results followed are first obtained in

dimensionless form and then converted to dimensional quantities to facilitate physical interpretation of the phenomena.

In Figure 2.2, the total force acting on the AFM tip due to the electrohydrodynamic and electrostatic contributions is depicted by the hysteresis curves. The positive force values represent the repulsion force (toward $-x$) on the tip, and the negative values represent the attraction force (toward $+x$) on the tip. During the simulated probing process, the case of purely hydrodynamic fluid-membrane interactions[1] ($\alpha = 0$) is used for reference. Clearly, similarly to the purely hydrodynamic case, AFM imaging in the low ionic strength electrolyte (case a) features monotonically increasing repulsive and decreasing attractive forces during the forward and reverse strokes, respectively. For solutions with stronger ionic strength, cases b, the electrohydrodynamic force loses its monotonicity and its behavior is determined by the competitive effects from the bending resistance of the membrane and the repulsive force generated by the electrostatic charged double layer. The decrease in magnitude of repulsive forces for the forward strokes is due to the unsymmetric electrostatic forces that push the membrane away from the tip, thereby reducing the draglike electrohydrodynamic forces acting on the AFM tip. Such a behavior is the most profound in cases c and d with the large ratio of the electric to viscous forces (α is large) and thin Debye layer, wherein the dominant electrostatic force (acting on the membrane, not the AFM tip) continuously pushes the membrane further away as the AFM tip approaches. As a result, the AFM tip-to-membrane separation distance never reaches the minimum threshold distance of 30 nm at which the tip motion should normally be reversed, and the dynamic behavior of the AFM tip-membrane is defined primarily by the

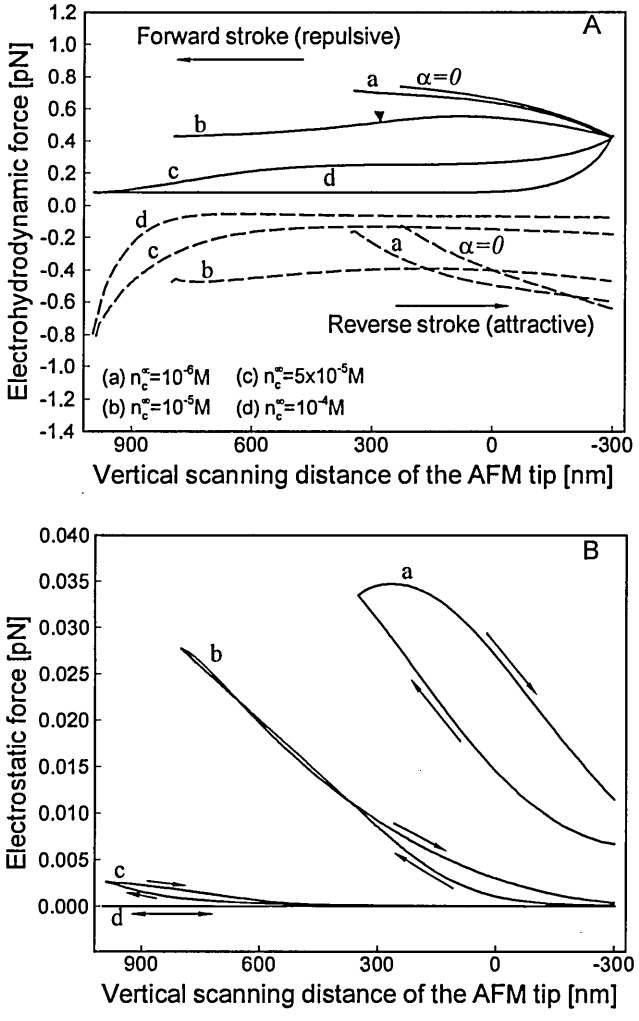

Figure 2.2 The comparison of electrohydrodynamic (A) and electrostatic (B) forces acting on the AFM tip during the forward and reverse strokes of the AFM imaging process for four dilute systems: (a) $n_c^{\infty} = 10^{-6} M$, $\kappa^{-1} = 304 nm$, $B = 144.3$, $c_0 = -1.216$, $\alpha = 97$, $dt = 0.01$. (b) $n_c^{\infty} = 10^{-5} M$, $\kappa^{-1} = 96 nm$, $B = 1447.2$, $c_0 = -0.384$, $\alpha = 307$, $dt = 0.03$. (c) $n_c^{\infty} = 5 \times 10^{-5} M$, $\kappa^{-1} = 43 nm$, $B = 7211$, $c_0 = -0.172$, $\alpha = 686.4$, $dt = 0.05$. (d) $n_c^{\infty} = 10^{-4} M$, $\kappa^{-1} = 30.4 nm$, $B = 14430$, $c_0 = -0.1216$, $\alpha = 971$, $dt = 0.1$. Note that in case a the entire stroke is within the Debye layer; in case b the tip enters the Debye layer at the point marked by the symbol ▼; and in cases c and d the AFM tip remains outside of the Debye layer for the entire stroke.

strong repulsive electrostatic force acting on the membrane as it begins to deform. In simulations, the forward stroke is terminated and reversed at the moment when the tip travels the distance of 1 μm from the membrane planar equilibrium state ($x = 0$). Furthermore, in these two cases, the validity of the boundary condition, $\gamma = 0$, at the cutoff distance $\sigma \sim 45$ μm (which is only 15 times the total height of the AFM tip) is questionable, since the large membrane deformation induced by the strong electrostatic force acting on the membrane should result in non-negligible tension in the membrane even in the far-field. Presently, no theoretically sound approach exists to evaluate the induced nonzero γ-tension in the far-field of the membrane, and our analysis with the vanishing tension boundary condition is limited to the AFM tip-membrane interactions of the small perturbation type. Alternatively, for some small and simple model cells such as a red blood cell, the entire cell membrane can be included into a closed simulation domain, making the boundary condition for the membrane tension no longer necessary. During the reverse stroke, the electrohydrodynamic force is attractive and its magnitude is initially smaller for cases a and b because of the assisted bending energy released by the recovering membrane. In the later stage, however, this attractive force becomes enhanced as the tip-to-membrane separation increases and their electrostatic coupling vanishes. In the cases of a stronger electrolyte, for example, cases c and d, the membrane recovery is resisted by the unsymmetric electrostatic force which renders the higher attractive force acting on the AFM tip in the early stage of the reverse stroke. This intriguing dynamics is very different from that observed in the experiments for noncontact AFM imaging of nondeformable solid surfaces[57] in which the repulsive electrohydrodynamic force always monotonically increases during the forward stroke

until exponential saturation within a highly repulsive region where the tip-to-surface separation distance falls below 30 nm and the short-range forces become significant. These short-range effects are beyond the scope of our study. The discontinuity in the electrohydrodynamic force is due to the piecewise constant approach speed of the AFM tip during the forward and reverse strokes.

The electrostatic force is continuous, always repulsive, and exhibits hysteresis behavior in the full cycle simulations because of the hysteresis in the membrane deformation as later shown in Figures 2.3 and 2.4A. The electrostatic interaction of the AFM tip and membrane increases as the AFM tip penetrates into the charged double layer of the membrane where the field-affected area of the tip becomes greater and the intensity of the electrical potential field increases. For the case of a stronger electrolyte with the large screening effect (case c), the electrostatic force is reduced significantly because most of the time the tip is outside of the double layer, where the electric field vanishes. And in case d, the electrostatic force is essentially zero as the tip never penetrates into or even close to the Debye layer. Note that the AFM tip never touches the membrane and the total surface force acting on the AFM tip and the membrane is due to a combined contribution from both the electrohydrodynamic and electrostatic forces as well as the membrane bending elasticity. Furthermore, in the reverse stroke the electrostatic force is greater than it is in the forward stroke, since the AFM tip and the membrane are closer to each other during the reverse tip motion leading to the greater electric field gradient and, thus, enhanced electric force. The surface forces illustrated in Figure 2.2 are in the piconewton and subpiconewton range, and the electrostatic force is an order of magnitude smaller than the electrohydrodynamic force. This is a result of the assumption made in

analysis of the small surface zeta potential (about -12.5 mV) in order to linearize governing equations. One may expect that for a higher surface potential the electrostatic force may contribute equally or become even more significant than the combination of the viscous and osmosis effects described by the electrohydrodynamic force. Indeed, eq 2-19 provides a scaling argument that the electrostatic force should approximately increase by 2 orders of magnitude as the membrane zeta potential increases 10-fold, if the ionic strength of the solution or the Debye length remains unchanged. The detailed simulation of the high zeta potential case demands a more complex analysis involving solution of the nonlinear Poisson equation for the electric field and is beyond the scope of this work.

Figure 2.3 demonstrates the instantaneous axisymmetric velocity vectors describing the flow field and the corresponding electrical equal-potential lines defining the tip-to-membrane electrostatic interactions for the intermediate case (case b) in Figure 2.2 at the three time instances, namely, the initial moment and the ends of the forward and reverse strokes. Both the velocity field and the electric field are computed in a postprocessing step using eqs 2-33, 41, and 42 after all required boundary values are calculated. The velocity vector plot reveals the flow structure resulting from the coupling of the AFM tip motion and the deformation of the cell membrane. The moving tip causes a converging/diverging flow pattern around the tip circumference, which is the generally observed behavior for the Stokes flows when the flow field is perturbed by a moving body of an arbitrary shape. The electrical equal-potential lines show the perturbed double layer with densely spaced isolines and the induced electric field inside the AFM tip. The resulting unsymmetric screening field causes a repulsive force acting on both the tip and

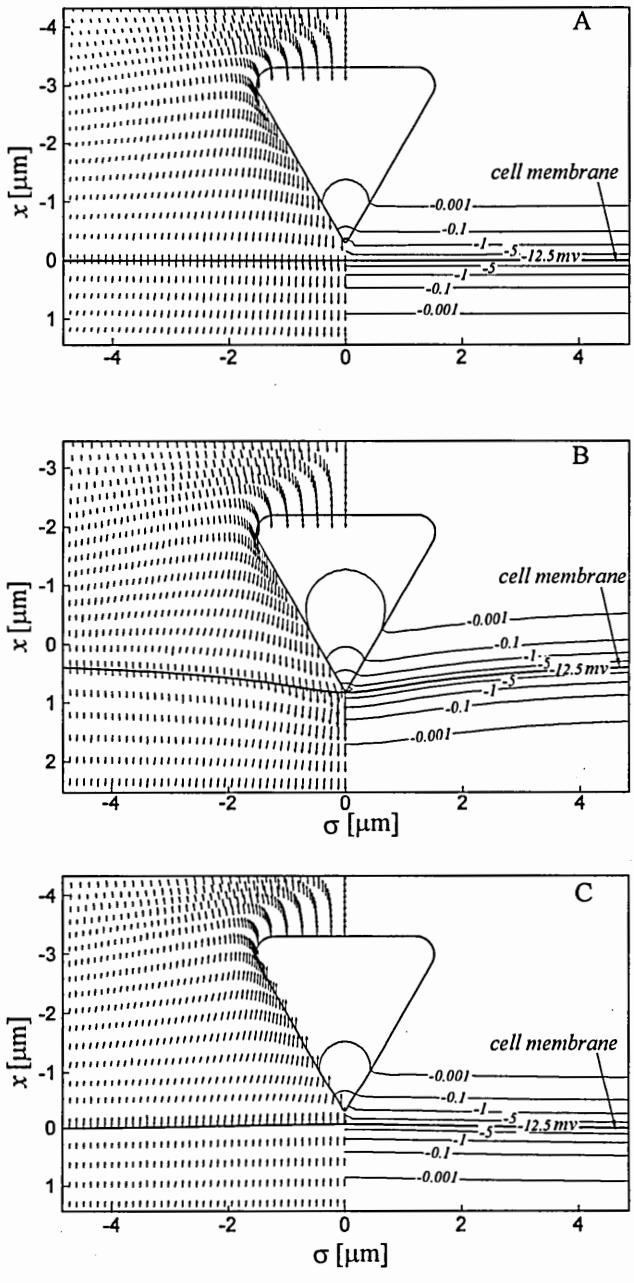

Figure 2.3 Instantaneous velocity vector field (left section) and the electrical potential isolines (right section) for simulation case b in Figure 2.2 at three time instances: (A) an initial moment, $t = 0.0\,s$, (B) the end of the forward stroke, $t = 0.109\,s$, and (C) the end of the reverse stroke, $t = 0.218\ s$.

the cell membrane. Also, the stress jump becomes more significant as the membrane tension, the bending forces, and the Maxwell electric forces increase around the membrane center where the membrane deformation is the greatest. The double-layer structure on both sides of the membrane exhibits an exponential decay resulting in a significant electrostatic force acting only on a small portion of the tip front. The electric field inside of the insulating AFM tip features large gradients to satisfy the continuity of flux in the electric boundary conditions.

Figure 2.4 shows the transient evolution of the membrane and the surface tension/compression force during the forward and reverse strokes, also corresponding to case b in Figure 2.2 for the time moment $t = 0.109s$ at the end of the forward stroke and $t = 0.218s$ at the end of the reverse stroke. The membrane deformation shown in Figure 2.4A reflects the dominance of fluid flow and electric effects over the membrane relaxation behavior near the center portion of the membrane during different stages of the imaging process. In particular, at the end of the forward stroke ($t = 0.109s$) the membrane shape features a sharp dip in the center where the AFM tip penetrates the deepest into a charged double layer leading to a local maximum of repulsive electrohydrodynamic shear and electrostatic forces (see Figure 2.3). The surface tension/compression forces in the membrane induced by the AFM probing action are shown in Figure 2.4B. At the end of the forward stroke ($t = 0.109s$), the membrane switches abruptly from the tension ($\gamma > 0$) to a compression ($\gamma < 0$) state because the strongly repulsive electrohydrodynamic stress and the Maxwell stress favor a compression deformation mode ($\gamma < 0$) near the center portion of the membrane. This unusual behavior was not observed in the previous study of chapter 1 due to neglected double-layer interactions.

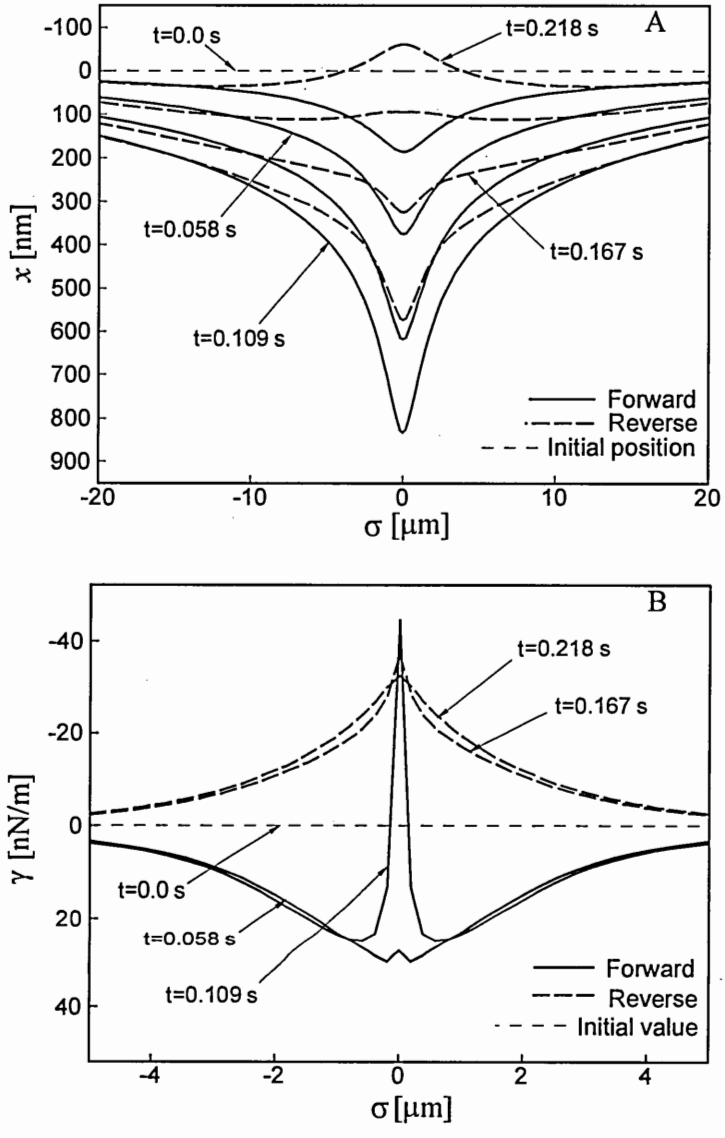

Figure 2.4 The transient evolution of the cell membrane (A) and the transient local tension (positive) and compression (negative) force along the cell membrane (B) during the forward and reverse strokes of the AFM imaging process corresponding to case b in Figure 2.2.

2.4 Conclusions

Electrohydrodymaic and electrostatic forces acting on the AFM tip and a charged biological membrane have been analyzed for a full cycle of noncontact, nonresonant AFM imaging in a dilute electrolyte solution. The AFM tip-membrane interactions are simulated using intimately coupled continuum theories of electrohydrodynamics, membrane biomechanics, and electrostatics within an integrated computational framework. The analysis neglects the molecular-level interactions and it is limited to the low zeta-potentials of the membrane immersed in the electrolyte which is in the state of local electrochemical equilibrium. Although greatly simplified, it is the first time when an integrated model for the coupled electromechanical and hydrodynamic analysis has been developed for AFM imaging of the soft and charged lipid bilayers and membranes.

Through careful scaling and simulations, it has been shown that the electrostatic force between the AFM tip and a membrane is always repulsive and an order of magnitude smaller than a electrohydrodynamic shear force. The shear force changes its behavior from repulsive during the forward AFM stroke to attractive during the reverse stroke, and it becomes significant only when the AFM tip penetrates into the electric double layer of the membrane. In the latter case, the surface force interactions are influenced by the strong coupling of the unsymmetric electric field perturbed by the dielectric AFM tip and the fluid flow induced on both sides of the deforming membrane. This results in an unusual membrane bending behavior at the end of the AFM forward stroke, which is not observed in the case of purely hydrodynamic AFM tip-membrane analysis discussed in chapter 1. The scaling arguments are also presented to extend the results to a more realistic case of the membrane with higher zeta potential immersed in the high ionic

strength electrolyte solutions. The fundamental insight obtained should be instrumental for qualitative interpretation of the AFM measurements of the electrophysiological and mechanical properties of biomembranes or supported artificial membranes in response to the change in the ionic strength of the solutions on both sides of the membrane.

CHAPTER 3

An Integrated Transport Model for Tracking an Exocytotic Event Dynamics Using a Microelectrode

Vesicular exocytosis is a process by which a vesicle within a cell fuses to a plasma membrane and releases its contents, one or several biochemical agents, into an extracellular medium. This process is one of the most important mechanisms in cell communications. We propose a theoretical model to simulate the intimately coupled dynamics and kinetics of an exocytotic event for an opening and expanding of a fusion pore, leading to vesicular polymer swelling and molecular messenger release. The model is based on continuum fluid transport and elasticity theories, and solved by the boundary integral method. The simulation results are qualitatively compared with experimental results from the literature of *in vitro* electroanalytical measurements of the Faradaic current resulting from messenger oxidation on an electrode surface. The results are significant as they provide new insight and a basic understanding of the slow and fast steps of an exocytotic sequence, allowing verification of competing hypotheses on what controls/limits messenger release during exocytosis.

3.1 Introduction

The complex biophysical process underlying the release of neurotransmitters and hormones from secretion cells, known as vesicular exocytosis, is an important mechanism that defines cell signaling and intercellular communication. This phenomenon

has drawn the attention of neuroscientists and physiologists because abnormal regulation of the cell signaling process may cause many human diseases. A simplified description of the exocytotic event starts with protein synthesis and vesicle packing in the cell cytoplasm, followed by the vesicle transport within the cell, fusion of the vesicle to the cell membrane by a working protein, and ends with the release of the vesicle content, that is one or several chemical messengers included in the vesicle granule matrix, to the extracellular medium. In the case of neurons, the released neurotransmitter crosses the synaptic cleft and directly binds to a receptor on a postsynapse or a muscle cell. For endocrine secretion cells, the sequence is similar except that a hormone is released into the bloodstream and it targets a particular cell to trigger the corresponding biological function. In the release process, several fundamental issues have been a focus of active research for more than a decade. These include the signal pathway that leads to membrane fusion, the structure and conformation change of the working proteins that mediate the pore opening, the expansion of a small fusion pore followed by the membrane unfolding, the role of the swelling granule, the signals that trigger or inhibit the overall secretion process, and transport mechanisms of these chemical messengers in a cellular environment.

Bio-transport phenomena of a dynamic exocytotic event involve fluid (due to intra- and extra- cellular physiological liquid environment) and solid (due to membrane tension/compression and granule swelling) mechanics that either promote or resist the messenger release from the fused vesicle granule and its transport through a fusion pore and a thin cleft to the binding zone of a specific target cell. This process involves two key features. First, once the fusion pore is opened, the fused membrane continues unfolding

until its minimum energy state is achieved. Both the cytoskeleton network that supports the plasma membrane of the host cell and the pre-stressed (higher energy) state of the fused vesicle membrane may provide the tension force to drive the event dynamics. It is known that the fused membrane may have nonhomogeneous tension and perhaps even locally varying elastic properties that, together with the expansion of the swelling granule matrix and the viscous drag forces in the fluid inside and outside of the cell, drive expansion of the fusion pore and the messenger release. The second important feature that has to be carefully considered in the analysis is that the granule inside of the vesicle undergoes a phase transition from a dense messenger-packed protein matrix to a fully swollen and empty (free of messengers) state. The granule matrix is a polyelectrolyte mixture, part of which is a network of proteins, effectively cross-linked by the divalent cations such as Ca^{2+}, and the rest interstice consists of highly concentrated secretion messengers and other ionic species. Once granule swelling is triggered by biochemical changes in the extracellular environment, the matrix transitions to a fully swollen state, and the negatively charged protein network either dissolves in the environment or resists further elastic expansion by stretching the polymer strands to maintain its structure. Similar to an ion exchanger, this transition phenomenon has a cascade behavior triggered by monovalent cations such as Na^+ and K^+.[68,69] These ions from the solution medium replace the divalent polymer cross-linkers and maintain electroneutrality while the molecular messengers and cross-linkers are released from the interstice of the protein network, and at the same time, water molecules gradually fill in the space. These phenomena are well known in synthetic polymer systems,[70] but it has not been clearly

established how they can be coupled to other transport processes involved in an exocytotic event.

Cellular experiments on the organized uptake and release of biochemical agents are commonly performed by fluorescence imaging techniques.[71,72] Optical limitations, however, prohibit a more detailed local analysis, which requires higher spatial and temporal resolutions on the scales below sub-microns and sub-milliseconds, respectively. In order to resolve these finer scales of local biophysical processes, a microelectrode-based biosensor is one of the most promising techniques and has been continuously developed for more than a decade.[73,74,75,76,77] The operating principle is rather simple: a stationary or a scanning electrode biased at a certain voltage/current level is used to detect a response current/voltage due to the interfacial flux of reactants in order to characterize a fingerprint of molecules, the interfacial transport phenomena, bioreactivities, neurotransmission, or hormone secretion processes. In the field of brain chemistry and neuroscience, efforts have been devoted to monitoring and characterizing the release and uptake events of neurotransmitters, with micron resolution, from a single cell in a culture, and even for mammalian brain tissues *in vivo* in response to chemical or electrical pulse stimuli.[78,79,80] This resolution is possible because these molecular messengers can be electrochemically oxidized on a carbon fiber electrode and be detected by electroanalytical methods. As for nonelectroactive molecules, a biological sensing element, such as an enzyme, is needed to enable electron flow through the electrode, for example, insulin detection with a glucose sensor. Enzymatic modification of the electrode surface has been used in the studies of various nonoxidizable neurotransmitters during exocytosis on the time scale of milliseconds,[81,82] and the chemically-modified electrode

was employed for detection of insulin release from the pancreatic β cells on a much longer time scale.[83]

To conclude this brief review of the current state-of-the-art in experimental investigations of exocytosis, in the last decade the efforts have been mainly focused on chronoamperometric real time monitoring of the secretion process by placing a microelectrode near the surface of the cultured secretion cell,[84,85,86,87,88,89,90] or directly detecting an isolated, electroporated granule of the mast cells.[68,91] However, owing to the lack of detailed biochemical information, a broad range of the characteristic length and time scales, and an overwhelming complexity of the phenomena, there have been only a few theoretical models developed, all of which are limited to a semi-empirical diffusion-like transport and a simplified cell/vesicle geometry. Stiles et al.[92] used Monte Carlo simulations to predict the passive diffusion behavior of acetylcholine from a small and clear synaptic vesicle with spatial and temporal resolutions of tenths of nanometers and microseconds, respectively. Amatore's and Wightman's groups[88,89] developed a semi-empirical diffusion-kinetics model to separate the effect of the pore opening kinetics and diffusional transport based on their experimental observations of adrenaline release from chromaffin cells. Recently, Farrell and Cox[93] also developed a diffusion model for a class of pore opening functions as a dynamic boundary condition to reproduce the efflux that matches experiments with mast cells for various vesicle sizes.

Early studies in the area of nanoscale fluid dynamics and transport phenomena in physiological applications have been reviewed by Ciofalo,[94] and it appears that the role of fluid–membrane interactions in exocytosis was first studied by Nir[95] using the boundary integral method adopted from simulation of coalescence phenomena of liquid droplets.

The importance of conformational dynamics of vesicles, including exocytosis and endocytosis, and fluid interactions are perhaps best illustrated in a collection of pioneering papers edited by Pincus[96] and, in particular, the visualization of transient dynamics of the pore opening and closing of vesicles by Sandre et al.[97]

It is apparent that cellular exocytosis is a very complex biophysical process that involves several intimately coupled phenomena that may occur on widely different time scales. Even an initial phase of exocytosis such as membrane fusion is a very complex topic that has been actively studied for more than two decades for its fundamental importance to cell biology. The theory of membrane fusion began with the hypothesis of stalk formation[98,99] associated with a hemifusion diaphragm and its continuous expansion into to a fusion pore. This model and those reported in numerous follow-up studies were built on a continuous theory of the curvature energy of an elastic bilayer membrane. More recent studies are focused on the biological function of protein mediators that initialize the membrane fusion, and are aimed at finding the molecular structure of these proteins and their conformational changes at different stages.[100,101] An excellent literature review on the biophysics of membrane fusion including atomistic simulations can be found in the recent Jahn and Grubmüller's article.[102] Once fused to the plasma membrane, swelling of the vesicle granule matrix is triggered by an "action potential"[103] or change in the solution composition.[104] The transition of the condensed granule matrix to a fully swollen state has similar dynamics to those observed in the swelling of ion exchange resin.[70]

Understanding of the intimately coupled dynamics and kinetics of exocytosis is without doubt a grand-challenge type of a problem that requires concerted experimental

and theoretical efforts. Many hypotheses have been proposed, and naturally many of them contradict one another. For example, it was believed that granule swelling may play a key factor that causes the fusion pore to expand,[89] but Monck et al.[105] shed doubts on this commonly accepted hypothesis by observing similar pore expansion velocity for various swelling conditions in experiments with mast cells. An interesting case was also observed by Holstein and Tardent[106] for an extremely fast nematocyst discharge process whose dynamics are very different from those of typical exocytosis.

It is too ambitious and perhaps even unrealistic to expect that a general theory can be developed for such a complex biophysical process as exocytosis. Thus, in this paper we only focus on the vesicle post-fusion step of the exocytotic sequence, aiming for development of a theoretically sound modeling framework that can be used to interpret the electroanalytical measurements of exocytosis. The set of models we developed are based on continuum theories with the length and time scales relevant to three specific experimental studies of exocytosis, which are used for the model validation. These models are governed by: (i) the quasi-steady Stokes equations of fluid motion induced by unfolding of the membrane, (ii) a transient, nonhomogeneous diffusion equation for the molecular messenger distribution inside of the swelling granule matrix, and (iii) a quasi-steady convection-diffusion equation for the transport of these chemical messengers in the extracellular solution. We use Helfrich's curvature energy theory and Zhong-can's equilibrium membrane equation,[12] augmented by the constraint equation for local membrane incompressibility, as a quasi-steady, nonlinear moving boundary condition to link the fluid stress fields on both sides of the fused membrane. In addition, to predict the swelling behavior of the protein network in the granule matrix, we apply the Tanaka,

Hocker, and Benedek (THB)[107] hydrogel model, originally designed for measuring the viscoelastic properties of gels using light scattering spectroscopy and later applied by Tanaka and Fillmore[108] to swelling of a spherical hydrogel.

The simulation results are qualitatively compared with the experimental data from the literature of the *in vitro* electroanalytical measurements of the Faradaic current resulting from the messenger oxidation at the microelectrode.[68,91;85,92;88,89,90] We believe that biologists and biochemists can find this model useful as a tool to verify competing hypotheses that control/limit the messenger release process as well as for interpretation of the electroanalytical measurements of exocytosis.

3.2 Theoretical Development

The model is developed using continuum transport theories of fluid mechanics, mass transfer, and electrochemistry, linear elasticity mechanics, and bilayer membrane mechanics. We assume that initially the fusion pore is already in an opened state and the vesicle and plasma membranes are securely fused (i.e., we do not consider "kiss-and-run" events), and the fused membrane has a homogeneous simple bilayer structure. The presence of cytoskeleton is not directly modeled, but it can be potentially included through the parameters in the macroscopic tension, bending, and viscous forces that govern unfolding of the membrane. We assume that both the extracellular environment and the intracellular fluids are homogeneous, incompressible Newtonian fluids with the same densities, but with different viscosities. We neglect molecular level interactions and other short-range effects. This includes neglecting electrostatic forces, a good assumption under normal physiological conditions (ie., an electrolyte buffer strength ~0.1 M), where

the electric forces are screened by a very thin (<1 nm) electric double layer in the extracellular medium and in the cytosol. The membrane thickness is also small (~ 5 nm) relative to the vesicle/cell size, so the membrane can be mathematically treated as an infinitesimally thin and perfectly smooth interface separating intra- and extra- cellular environments. We neglect the effect of any heat generation due to nonequilibrium, rapid matrix swelling. Further, thermally-induced membrane fluctuations are assumed insignificant as compared to the large deformation of the fused membrane. In this idealized system, we further assume that the mechanical work performed by the swelling granule matrix on the vesicle membrane can be neglected in the limit of small deformations, meaning that the linear elasticity theory is valid. In the case of large granule matrix deformation, the two-phase polymer system has to be modeled and a much more complex, nonlinear analysis would be required.

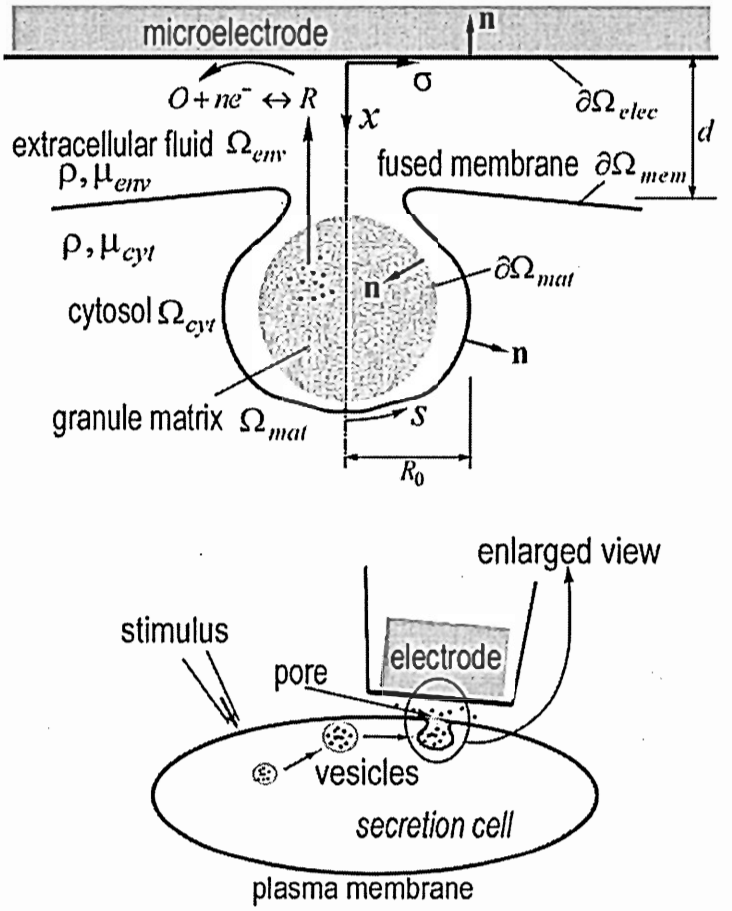

Figure 3.1 Schematic of electroanalytical monitoring of exocytosis using a microelectrode (bottom) and an idealized simulation domain (top).

3.2.1 Scaling of the Phenomena

In this section, we analyze the time scales involved in the system to properly define the characteristic time for the process and also to assess whether certain simplifications in the analysis can be made. Figure 3.1 shows a schematic of the idealized physical arrangement that includes the intracellular cytosol (Ω_{cyt}), the extracellular fluid environment (Ω_{env}), and a separating boundary established by a fused vesicle/plasma membrane ($\partial\Omega_{mem}$). The domain of a granule matrix (Ω_{mat}) is bounded by an interface ($\partial\Omega_{mat}$), and the reacting surface of the microelectrode ($\partial\Omega_{elec}$) is placed adjacent to the pore in the fused membrane in the extracellular environment. An axisymmetric three-dimensional hourglass shape[109] is employed as an initial configuration with the fusion pore and granule matrix positioned along the centerline. The following notation is used hereafter: R_0 is the initial radius of a secretion vesicle, V_0 is the experimentally observed maximum expansion velocity of the fusion pore, and d is a fixed electrode-to-membrane separation distance (usually $d \sim R_0$). The extracellular fluid is characterized by density ρ and dynamic viscosity μ_{env}. The cytosol is approximated by the same fluid density ρ, but, in general, has a different viscosity μ_{cyt}. The simplified bilayer structure of the fused membrane is characterized by its intrinsic elastic properties such as an effective bending rigidity B, a spontaneous curvature c_0, and a local tension force γ.

By assuming that the exocytosis dynamics are driven by the interplay between the membrane relaxation (unfolding) and release and transport of molecular messengers from the vesicle granule, five time scales can be identified as relevant to the problem in hand. They all can be expressed in terms of the length scale $\ell \sim R_0$ as follows:

(i) The fusion pore expansion time scale, t_{pore}, characterizes the pore expansion dynamics, and is defined by the characteristic length scale, R_0, divided by the maximum pore expansion velocity, V_0.

(ii) The viscous diffusion time scale, t_{visc}, characterizes the viscous driving force of fluid motion, and is defined by the square of the diffusion length (also scaled by the vesicle radius R_0^2) divided by the viscous diffusivity of either the cytosol, μ_{cyt}/ρ or the extracellular fluid, μ_{env}/ρ.

(iii) The messenger diffusion time scale, $t_{diff,bulk}$, characterizes the molecular transport to the electrode through the extracellular electrolyte solution, and is defined by the square of the distance, $d^2 \sim R_0^2$, divided by the bulk diffusivity, D_{bulk}.

(iv) The second characteristic time for messenger transport, $t_{diff,matrix}$, characterizes the apparent diffusion behavior through the protein network inside the granule matrix, and similarly is defined by R_0^2 / D_{matrix}.

(v) The collective diffusion time scale, $t_{diff,swell}$, controls the linear swelling dynamics of the protein matrix, and is defined by R_0^2 / D_{swell}, where the physical meaning of the collective swelling diffusivity D_{swell} is discussed later in the manuscript.

To summarize, the relevant time scales for the problems are given by:

$$t_{pore} \sim R_0 / V_0, \qquad t_{visc} \sim \rho R_0^2 / \mu_{cyt}, \qquad t_{diff,bulk} \sim R_0^2 / D_{bulk}, \tag{3-1}$$

$$t_{diff,matrix} \sim R_0^2 / D_{matrix}, \qquad t_{diff,swell} \sim R_0^2 / D_{swell}$$

Note that the electron transfer of the oxidation reaction at the electrode-solution interface is a much faster process than the dynamics presented (i.e., diffusion-limited transport), so the electrochemical reaction can mathematically treated as an instantaneous event.

To compare the relative magnitude of the time scales in eq 3-1, we use experimentally obtained values for the secretion vesicle size R_0 and the maximum pore expansion velocity V_0 for different types of vesicles. Specifically, we look at three cases: (a) the large size vesicles in mast cells $R_0 \sim 2.5$ μm,[91] with a pore expansion velocity $V_0 \sim$ 20 μm/s;[93] (b) the small clear synaptic vesicles, $R_0 \sim$ 20 nm, with a pore expansion velocity $V_0 \sim 25$ μm/s;[85,92] and (c) the medium size vesicles of the chromaffin cells $R_0 \sim$ 150 nm[89] with the expansion velocity V_0 ranging between 0.37 μm/s (beginning of the process) and 18 μm/s (end of process).[89] Based on these experimental data, the characteristic pore expansion time scales for cases (a), (b), and the fast stage of (c), respectively, are given by

$$t_{pore} \sim \text{(a) } 0.125 \text{ s, (b) } 8.0\text{x}10^{-4} \text{ s, and (c) } 8.33\text{x}10^{-3} \text{ s} \qquad (3\text{-}2)$$

For a typical physiological cell environment with fluid density $\rho \sim 10^3$ kg/m^3 and viscosity $\mu_{env} \sim 1.5\text{x}10^{-3}$ kg/m.s (1.5 cp) at room temperature, the viscous diffusion time scales in the extracellular environment are different for all three cases (a, b, and c) considered because of the difference in the characteristic length scale:

$$t_{visc} \sim \text{(a) } 4.2\text{x}10^{-6} \text{ s, (b) } 2.7\text{x}10^{-10} \text{ s, and (c) } 1.5\text{x}10^{-8} \text{ s} \qquad (3\text{-}3)$$

For the purpose of scale analysis, if we assume the viscosity of the cytosol μ_{cyt} is of the same order of magnitude as that of the extracellular environment, then the viscous

diffusion time scales in the cytosol are similar to the extracellular environment values given by eq 3-3.

Two diffusion time scales based on molecular diffusivities in the bulk solution ($D_{bulk} \sim 6.0\text{x}10^{-10}$ m^2/s[18,92]) and in the granule matrix ($D_{matrix} \sim 2.0\text{x}10^{-12}$ m^2/s[68]) are given by

$$t_{diff,bulk} \sim \text{(a) } 1.0\text{x}10^{-2}\text{ s, (b) } 6.7\text{x}10^{-7}\text{ s, and (c) } 3.75\text{x}10^{-5}\text{ s} \tag{3-4}$$

$$t_{diff,matrix} \sim \text{(a) 3.1 s, (b) Not applicable (no granule in the vesicle), and (c) } 1.13\text{x}10^{-2}\text{ s} \tag{3-5}$$

Finally, the apparent swelling diffusivity of the granule D_{swell} is about $1.4\text{x}10^{-11}$ m^2/s[68] and the corresponding time scales for the cases (a), (b), and (c) are given by

$$t_{diff,swell} \sim \text{(a) 0.45 s, (b) Not applicable (no granule in the vesicle), and (c) } 1.6\text{x}10^{-3}\text{ s} \tag{3-6}$$

In summary, although the relevant time scales for the problem span a wide range of magnitudes, they can be grouped into several categories based on their relative order of magnitudes as follows:

$$\left.\begin{array}{l}(a)\ t_{diff,matrix} > t_{diff,swell} \sim t_{pore} \\ (b)\ t_{pore} \\ (c)\ t_{diff,matrix} \sim t_{pore} > t_{diff,swell}\end{array}\right\} > t_{diff,bulk} >> t_{visc},\ t_{reaction} \tag{3-7}$$

The comparison of time scales given by eq 3-7 is important in two respects: (1) it establishes certain generality in the dynamics of the exocytotic event regardless of the specific vesicle type, (2) it is credible enough for theory development as being based on the direct experimental observations. From the theoretical prospective, eq 3-7 is also very important as it allows us to reduce the complexity of the models underlying the process dynamics for different temporal observation windows (e.g., by contrasting the fast versus

slow processes) and by treating only a limited number of the key phenomena that are relevant on the time scale for the specific observation window. That is:

(i) The oxidation reactions at the electrode/electrolyte interface are very fast and can be treated as an equilibrium surface phenomenon. As a result, the transport models in the bulk fluid environment are free of the source/sink terms associated with the non-equilibrium species consumption/generation.

(ii) The viscous diffusion time scale, t_{visc}, is much smaller than all diffusion time scales, $t_{diff,bulk}$, $t_{diff,swell}$, and $t_{diff,matrix}$, so that the quasi-steady approach to the analysis of the fluid motion (i.e., a vanished time derivative term in the Navier-Stokes equations), and similarly, the quasi-steady stress balance equation for the deforming membrane bilayer can be employed.

(iii) The ratio of $t_{diff,bulk}$ to t_{pore} generates the Peclet number, which compares the species transport by advection and by bulk diffusion,

$$Pe_{fluid} = \frac{t_{diff,bulk}}{t_{pore}} = \frac{V_0 R_0}{D_{bulk}} \sim \text{(a) } 8.3\text{x}10^{-2}\text{, (b) } 8.4\text{x}10^{-4}\text{, and (c) } 4.5\text{x}10^{-3} \qquad (3\text{-}8)$$

A very small Peclet number in case (b) suggests that advection effects are negligible (i.e., a vanished bulk advection term in the convection-diffusion equation). It also implies that the pore expansion is relatively slow and, thus, the transient molecular flux is hindered by the small fusion pore when we focus on resolving the diffusion of neurotransmitters to the microelectrode on the time scale of $t_{diff,bulk}$. In cases (a) and (c), the bulk advection effects are small but may not be negligible.

(iv) The comparison of bulk and matrix diffusion times scales, i.e., $t_{diff,bulk}$ vs. $t_{diff,matrix}$, generates a very small diffusivity ratio,

$$\frac{t_{diff,\,bulk}}{t_{diff,\,matrix}} = \frac{D_{matrix}}{D_{bulk}} \sim \text{(a) } 3.33\text{x}10^{-3}\text{, (b) Not applicable, and (c) } 3.33\text{x}10^{-3} \qquad (3\text{-}9)$$

This implies that the dynamics of the process in cases (a) and (c) is limited by the diffusion in the vesicle granule matrix. Thus, if time scale $t_{diff,matrix}$ needs to be resolved, the quasi-steady analysis can be used for the transport phenomena in the liquid environment (i.e., a vanished time derivative term in the mass transport equation), whereas a transient diffusion system should be applied to the matrix domain.

(v) A transient analysis of the swelling dynamics of the granule matrix is required for cases (a) and (c) because the messenger concentration field inside the vesicle matrix is first dominated by the swelling behavior on a shorter time scale, $t_{diff,swell}$, and later by the matrix diffusion on a longer time scale, $t_{diff,matrix}$. The close proximity of the matrix swelling and matrix diffusion time scales makes these two dynamic processes intimately coupled, thus requiring simultaneous resolution.

(vi) Finally, owing to the very low Reynolds number, $\text{Re} = \rho V_0 R_0 / \mu_{cyt} = 3.3\text{x}10^{-7} \sim 3.3\text{x}10^{-5}$, the flow inertial forces are negligibly small as compared to the viscous forces and, thus, the nonlinear advection terms in the Navier-Stokes equations can be dropped.

3.2.2 Mathematical Model

Figure 3.1 shows a schematic of the simulation domain used for the model development. A Eulerian axisymmetric coordinate system with the origin affixed to the electrode surface and the axial coordinate axis x pointed downward is used to simulate (i) the intracellular and extracellular fluid motion, messenger transport, and the membrane deformation, and (ii) the granule elastic deformation and intra-matrix molecular messenger transport. Due to the lack of the detailed biological information about extrusion behavior of the granule matrix, we assume that the matrix is suspended at a fixed position in the extracellular fluid that fills the vesicle when the pore is opened.

In general, the messenger transport in the fluid as well as in the granule matrix is governed by the general transient, nonhomogeneous transport equation,

$$\frac{\partial C(\mathbf{x})}{\partial t} + \nabla \cdot (C(\mathbf{x})\mathbf{v}(\mathbf{x})) = D\nabla^2 C(\mathbf{x}) + S(\mathbf{x}), \quad \mathbf{x} \in \Omega \tag{3-10}$$

where C is the local neurotransmitter concentration, S is the sink/source term due to homogeneous chemical reactions involving neurotransmitters (if present), $\mathbf{v}$ is the bulk advection fluid velocity vector, and D is a diffusivity (assumed constant). Further, eq 3-10 is strictly valid in the limit of the linear Fickian diffusion in a dilute, binary system. It should also be noted that neurotransmitter transport is intimately coupled to the fluid dynamics of the extra and intra cellular fluids since eq 3-10 requires knowledge of the fluid velocity field as an input. To make the presentation of the model development clear, we first introduce the model for the fluid motion as it remains the same for all three cases (a), (b), and (c) considered here. Then, we discuss on the case-by-case basis the governing messenger transport models for cases (a), (b), and (c), because of the difference in the time scales leading to differences in the mathematical formulation.

Finally, the fluid and mass transport models are coupled by the initial and boundary conditions, which are also of a general nature and equally applicable to all three cases (a), (b), and (c). Such a presentation order not only makes the mathematical logic clearer, but also allows for case-by-case comparison of the model predictions with the experimental results from the literature.

3.2.2.1 The Fluid System

According to the scaling arguments presented in the previous section, the dynamics of both fluids, i.e., inside (Ω_{cyt}) and outside (Ω_{env}) of the cell (Figure 3.1), is governed by the quasi-steady Stokes equation and the continuity equation:

$$-\nabla p(\mathbf{x})+\mu_{env}\nabla^2\mathbf{v}(\mathbf{x})=0,\quad \nabla\cdot\mathbf{v}(\mathbf{x})=0 \qquad \text{for} \quad \mathbf{x}\in\Omega_{env} \tag{3-11a}$$

$$-\nabla p(\mathbf{x})+\mu_{cyt}\nabla^2\mathbf{v}(\mathbf{x})=0,\quad \nabla\cdot\mathbf{v}(\mathbf{x})=0 \qquad \text{for} \quad \mathbf{x}\in\Omega_{cyt} \tag{3-11b}$$

where p, $\mathbf{v}$, μ_{env}, μ_{cyt} are the pressure, the velocity vector, and the dynamic viscosities of the extracellular environment and cytosol, respectively, and $\mathbf{x}$ denotes a position vector in the Cartesian coordinate system. For both eqs 3-11a and 11b, the hydrodynamic pressure is scaled by the fluid viscous force based on the cytosol viscosity μ_{cyt}, so that the dimensionless Stokes equations can be written as, regardless of the time scale selected,

$$-\nabla p+\lambda\nabla^2\mathbf{v}=0,\quad \nabla\cdot\mathbf{v}=0,\qquad \mathbf{x}\in\Omega_{env} \tag{3-12a}$$

$$-\nabla p+\nabla^2\mathbf{v}=0,\quad \nabla\cdot\mathbf{v}=0,\qquad \mathbf{x}\in\Omega_{cyt} \tag{3-12b}$$

with the viscosity ratio defined by $\lambda=\mu_{env}/\mu_{cyt}$. These governing momentum conservation equations are subject to the following boundary conditions:

$$\mathbf{v} = 0, \quad |\mathbf{x}| \to \infty \qquad \text{vanishing velocity (quiescence) at the infinity} \qquad (3\text{-}12c)$$

$$\mathbf{v} = 0, \quad \mathbf{x} \in \partial\Omega_{elec} \qquad \text{no slip condition on the electrode surface} \qquad (3\text{-}12d)$$

$$\mathbf{v} = \mathbf{v}_{mem}, \quad \mathbf{x} \in \partial\Omega_{mem} \qquad \text{no slip condition on the cell membrane} \qquad (3\text{-}12e)$$

It should be emphasized that the scaling arguments indicate that the same Stokes system of equations is appropriate to describe the fluid motion in all three cases (a), (b), and (c) that are considered in this study.

3.2.2.2 Case (a): Serotonin Release by an Electroporated Granule of the Mast Cell

In the first case (a) we consider the messenger diffusion in a freely suspended, electroporated granule matrix as the rate controlling process for the microelectrode signal. This corresponds to the experimental studies performed by Marszalek et al.[68,91] Based on the experimental conditions, the scales for the characteristic time, length, the messenger concentration, and fluid velocity are given by,

$$t_{char} \sim t_{diff,matrix} \sim 3.1 \text{ s}, \quad \ell \sim R_0 \sim 2.5 \text{ μm}, \qquad (3\text{-}13)$$

$$C \sim C_0 \sim 3.37 \text{ moles/m}^3 \ (3.37\text{x}10^{-3} \text{ M}), \quad \mathbf{v} \sim D_{matrix} / R_0 \sim 0.8 \text{ μm/s},$$

respectively. Here, C_0 is the initial concentration of serotonin in an isolated granule of the mast cell. In the experiments, electroporation was used to disrupt the granule membrane, and the pore expansion velocity was estimated to be close to 10~25 μm/s.[91] Using the scaling arguments from the previous section, the serotonin concentration field in the extracellular fluid Ω_{env} should be in a quasi-steady state, the advection mass transport is negligible in a quiescent fluid environment, and no homogeneous reactions involving serotonin take place. With these observations, the mass conservation equation,

eq 3-10, governing serotonin transport in the extracellular fluid environment reduces to a simple Laplace equation,

$$\nabla^2 C = 0, \quad \mathbf{x} \in \Omega_{env} \tag{3-14}$$

On the other hand, the serotonin transport inside of the granule matrix with fast swelling behavior is described by the transient diffusion-advection system with the local matrix bulk velocity $\mathbf{v}$ related to the matrix swelling deformation $\mathbf{u}$ ($\mathbf{v} = \partial \mathbf{u}/\partial t$),

$$\frac{\partial C}{\partial t} + \nabla \cdot (C\mathbf{v}) = D_{matrix} \nabla^2 C, \quad \mathbf{x} \in \Omega_{mat} \tag{3-15}$$

In eq 3-15, the bulk advection term $\nabla \cdot (C\mathbf{v})$ can be separated into sum of two components, $\mathbf{v} \cdot \nabla C$ and $C(\nabla \cdot \partial \mathbf{u}/\partial t)$. Since we only consider small matrix deformation, we assume that the contribution from the first term is relatively small as compared to the divergence effect given by the second term $C(\nabla \cdot \partial \mathbf{u}/\partial t)$. Physically, the divergence term represents a pseudo-sink (dilution effect) in the system caused by the volumetric expansion of the granule. It is interesting to note that since $t_{diff,matrix} > t_{diff,swell}$ and we are focusing on resolving the matrix diffusion process, the local matrix dilution effect dominates the system dynamics at the very beginning of the process and it vanishes as the process continues with the diffusion effect taking control at a longer time. With the above mentioned assumptions, the governing equation describing neurotransmitter transport in the granule matrix, eq 3-15, can be expressed in the following dimensionless form,

$$\frac{\partial C}{\partial t} = \nabla^2 C - C(\nabla \cdot \partial \mathbf{u}/\partial t), \quad \mathbf{x} \in \Omega_{mat} \tag{3-16}$$

The system is completed by specifying the initial and boundary conditions, also expressed in a dimensionless form,

$C = 1$, $\mathbf{x} \in \Omega_{mat}$ at $t = t_0$

uniform initial concentration of neurotransmitters in the matrix (3-17a)

$C = 0 \ , \ \mathbf{x} \in \Omega_{env}$ at $t = t_0$

initial absence of neurotransmitters in the fluid environment (3-17b)

$C = 0 \ , \ |\mathbf{x}| \to \infty$

neurotransmitter concentration vanishes at the infinity (3-17c)

$C = 0 \ , \ \mathbf{x} \in \partial\Omega_{elec}$

infinitely fast neurotransmitter oxidation at the electrode surface (3-17d)

$\partial C / \partial n = 0, \ \mathbf{x} \in \partial\Omega_{mem}$

nonpermeable membrane (everywhere except the open pore) (3-17e)

$C_{matrix} = C_{env}, \ \mathbf{x} \in \partial\Omega_{mat}$

continuity of the concentration field at the matrix interface (3-17f)

$D_r \nabla C_{matrix} \cdot \mathbf{n} = \nabla C_{env} \cdot \mathbf{n}, \ \mathbf{x} \in \partial\Omega_{mat}$

continuity of the messenger flux through the matrix interface (3-17g)

In the last eq 3-17g, the relative diffusivity is defined as $D_r = D_{matrix} / D_{bulk}$. The displacement of the swelling matrix and that of the matrix/solution interface is governed by the Tanaka, Hocker, and Benedek (THB) hydrogel model,[107] which is described later in some details. The effect of the pore expansion of the electroporated membrane on the neurotransmitter transport is simulated by tracking the opening of the pore area of the membrane (using the constant lateral pore expansion speed). Naturally, everywhere where the pore is open the coupling boundary conditions, eqs 3-17f and 17g, are applied; whereas the membrane outside of the open pore is treated as a nonpermeable interface described by eq 3-17e.

3.2.2.3 Case (b): Neurotransmitter Release by a Small and Clear Synaptic Vesicle

In the previous case, we focused on the serotonin transport in an electroporated granule of the mast cell with the temporal scale, $t_{diff,matrix}$, of the order of milliseconds. Here, in case (b), we change our focus to a much faster exocytotic event, that is neurotransmitter release by a small and clear (i.e., without a granule inside) synaptic vesicle.[85,92] The length/time scales for this process are in a nanometer/microsecond range and defined by the bulk diffusion in the extracellular fluid. The order-of-magnitude values for other characteristic scales are given by,

$$t_{char} \sim t_{diff,bulk} \sim 0.67\,\mu s, \quad \ell \sim R_0 \sim 20\ nm, \tag{3-18}$$

$$C \sim C_0 \sim 270\ moles/m^3\ (0.27\ M), \quad \mathbf{v} \sim D_{bulk} / R_0 \sim 0.03\ m/s$$

Here, C_0 is the initial concentration of the neurotransmitter inside of the clear vesicle at the beginning of the pore expansion process. Based on the previous scaling results, the bulk advection effect can be neglected in describing the neurotransmitter transport in the extracellular fluid, owing to a very small Peclet number. Thus, a simple transient diffusion equation can be used to simulate messenger transport,

$$\frac{\partial C}{\partial t} = \nabla^2 C, \qquad \mathbf{x} \in \Omega_{env} \tag{3-19}$$

with the initial and boundary conditions given by the following dimensionless equations:

$C = 1$, $\mathbf{x} \in \Omega_{vesicle}$ at $t = t_0$

uniform initial concentration of neurotransmitter inside the vesicle (3-20a)

$C = 0$, $\mathbf{x} \in \Omega_{env} - \Omega_{vesicle}$ at $t = t_0$

initial absence of neurotransmitters in the fluid environment (3-20b)

$C = 0$, $|\mathbf{x}| \to \infty$

neurotransmitter concentration vanishes at the infinity (3-20c)

$C = 0 \ , \ \mathbf{x} \in \partial\Omega_{elec}$

infinitely fast oxidation of neurotransmitters on the electrode surface (3-20d)

$\partial C / \partial n = 0, \ \mathbf{x} \in \partial\Omega_{mem}$

nonpermeable membrane (3-20e)

Note that in this case the vesicle is free of a granule matrix, and the lumen contained inside the vesicle, and denoted as a domain $\Omega_{vesicle}$, is considered to be a part of Ω_{env} with the constant diffusivity D_{bulk} assumed the same as in the solution environment. Based on the experimental results,[85,92] the initial radius of the fusion pore upon opening is about 1 nm. The pore expansion continues at the speed ~25 nm/ms until the pore radius reaches an approximately 5 nm and then the neurotransmitters continuously diffuse out through the fixed in size fusion pore.

3.2.2.4 Case (c): Adrenaline Release by a Medium Size Vesicle in the Chromaffin Cell

The case (c) is the most complex and it includes the main aspects of the previous two models to simulate the release of adrenaline from the granule matrix enclosed by a vesicle of the chromaffin cell. We select $t_{diff,matrix}$ as the characteristic time scale in order to match the sub-millisecond temporal resolution of experiments reported in the references.[88,89,90] Based on the experimental conditions, the reference values for the scaling parameters are given by

$$t_{char} \sim t_{diff,matrix} \sim 11.3 \text{ ms}, \quad \ell \sim R_0 \sim 150 \text{ nm}, \tag{3-21}$$

$$C \sim C_0 \sim 600 \text{ moles/m}^3 \text{ (0.6 M)}, \quad \mathbf{v} \sim D_{matrix} / R_0 \sim 13.3 \text{ μm/s}$$

where C_0 is the initial concentration of adrenaline inside the granule matrix. In the fluid domains, the quasi-steady diffusion-advection equation is applied,

$$D_r(\mathbf{v}\cdot\nabla C)=\nabla^2 C, \quad \mathbf{x}\in\Omega_{env} \tag{3-22}$$

Where the relative diffusivity is defined by $D_r = D_{matrix}/D_{bulk}$ as in the case (a). The neurotransmitter concentration inside of the granule matrix is described by the transient diffusion equations with the sink term on the right-hand-side representing the matrix dilution due to fast swelling,

$$\frac{\partial C}{\partial t}=\nabla^2 C - C(\nabla\cdot\partial\mathbf{u}/\partial t), \quad \mathbf{x}\in\Omega_{mat} \tag{3-23}$$

The initial and boundary conditions are given by:

$C=1$, $\mathbf{x}\in\Omega_{mat}$ at $t=t_0$

uniform initial concentration of neurotransmitters in the matrix (3-24a)

$C=0$, $\mathbf{x}\in\Omega_{env}$ at $t=t_0$

initial absence of neurotransmitters in the fluid environment (3-24b)

$C=0$, $|\mathbf{x}|\to\infty$

neurotransmitter concentration vanishes at the infinity (3-24c)

$C=0$, $\mathbf{x}\in\partial\Omega_{elec}$

infinitely fast neurotransmitter oxidation on the electrode surface (3-24d)

$\partial C/\partial n=0$, $\mathbf{x}\in\partial\Omega_{mem}$

nonpermeable membrane (3-24e)

$C_{matrix}=C_{env}$, $\mathbf{x}\in\partial\Omega_{mat}$

continuity of the concentration field at the matrix interface (3-24f)

$D_r\nabla C_{matrix}\cdot\mathbf{n}=\nabla C_{env}\cdot\mathbf{n}$, $\mathbf{x}\in\partial\Omega_{mat}$

continuity of the messenger flux through the matrix interface (3-24g)

3.2.2.5 First Dynamic Boundary Condition: Large Deformation of the Fused Membrane

The first dynamic boundary condition describes the continuous expansion of the fusion pore and the unfolding behavior of the fused membrane, both modeled by a continuous deformation of a simple lipid bilayer structure. We assume that the large deformation of the membrane is driven by the local tension applied to the fused membrane and by the curvature induced bending energy. We also assume that the simple fluidlike bilayer membrane has locally isotropic tension on the time scale of interest and has negligible shear elasticity. In our earlier works,[1,2] a generalization of the interfacial force jump condition for a two-fluid system[25] has been developed by including the formalisms of Helfrich's curvature energy theory[11,36] and Zhong-can's membrane mechanics.[28] To summarize these results, the surface force jump condition for the fluid interface is governed by a quasi-steady stress balance in the fluids (cytosol and the extracellular environment in this case) adjacent to both sides of the membrane,

$$\left(\boldsymbol{\tau}_{cyt}\cdot\mathbf{n}-\boldsymbol{\tau}_{env}\cdot\mathbf{n}\right)+\nabla_s\gamma-\gamma\mathbf{n}\left(\nabla_s\cdot\mathbf{n}\right)=0,\qquad \mathbf{x}\in\partial\Omega_{mem} \tag{3-25}$$

where $\boldsymbol{\tau}$ denotes the fluid stress tensor, $\left(\boldsymbol{\tau}_{cyt}\cdot\mathbf{n}-\boldsymbol{\tau}_{env}\cdot\mathbf{n}\right)$ is the net surface traction induced by the hydrodynamic stresses from the adjacent fluids and acting along the surface normal $\mathbf{n}$. The fluid stresses are balanced by the isotropic local tension/compression of the membrane expressed in terms of $\nabla_s\gamma-\gamma\mathbf{n}\left(\nabla_s\cdot\mathbf{n}\right)$, where ∇_s represents the surface gradient operator. The shear component $\nabla_s\gamma$ is given by the membrane tension gradient along the tangential direction $\mathbf{s}$ of the membrane, the normal component $\gamma\mathbf{n}\left(\nabla_s\cdot\mathbf{n}\right)$ is defined by the membrane equilibrium shape equation.[12,28] Both

terms solely depend on the instantaneous geometry of the evolving membrane and its elastic properties. By using the Zhong-can's equilibrium shape equation for biomembranes,[28] eq 3-25 can be rearranged to become the following force jump condition, which is suitable for the boundary integral solution of the problem:

$$\Delta \mathbf{f} = -\nabla_s \gamma + \left(-2\gamma H + B(2H + c_0)(2H^2 - 2K - c_0 H) + 2B\nabla^2 H\right)\mathbf{n} \tag{3-26}$$

Here, $\Delta \mathbf{f} = \boldsymbol{\tau}_{cyt} \cdot \mathbf{n} - \boldsymbol{\tau}_{env} \cdot \mathbf{n}$ is the net surface traction, H is the mean curvature, K is the Gaussian curvature, B is the apparent membrane bending rigidity, c_0 is the effective spontaneous curvature, and ∇^2 is the Laplace-Beltrami operator for the curvilinear surface. An additional assumption of membrane local incompressibility, $\partial(dA)/\partial t = 0$, is enforced based on the membrane surface area constraint condition to complete the formulation since the local tension force γ is an additional unknown introduced by the boundary condition.[1,2] A general form of the constraint equation for a locally incompressible membrane was first derived by Pozrikidis[30] to study deformation of red blood cells in the shear flow and it can be expressed in terms of the arc-length coordinate,

$$\sigma \hat{\mathbf{t}}_s \cdot \frac{\partial \mathbf{v}}{\partial s} + \mathbf{v} \cdot \hat{\mathbf{e}}_\sigma = 0, \qquad \mathbf{x} \in \partial\Omega_{mem} \tag{3-27}$$

where $\hat{\mathbf{t}}_s$ denotes the local surface tangent, σ is the coordinate along the radial direction, and $\mathbf{v}$ is the local migration velocity of the fused membrane. The suitable scales for the parameters in the membrane dynamic boundary condition are defined by

$$\gamma \sim D\mu_{cyt}/R_0, \quad B \sim D\mu_{cyt}R_0, \quad H \sim 1/R_0, \tag{3-28}$$

$$K \sim 1/R_0^2, \quad c_0 \sim 1/R_0, \quad \mathbf{f} \sim D\mu_{cyt}/R_0^2$$

where $D = D_{bulk}$ in the case (b), and $D = D_{matrix}$ in the case (c). Using these scales, it is apparent that both the stress balance condition, eq 3-26, and the membrane area

constraint equation, eq 3-27, retain their original forms after being made dimensionless. Finally, it is worth mentioning that the mean curvature and the Gaussian curvature can be transformed into the parametric forms in terms of the arc-length coordinate s along the membrane interface $\partial\Omega_{mem}$.[2]

3.2.2.6 Second Dynamic Boundary Condition: Swelling Matrix Interface

Experimental results[68,91] suggest that the vesicle granule matrix increases by 30~40% in radius and 2~3 fold in volume during the swelling process as compared to its condensed state, thus a dynamic boundary condition is required to describe the interfacial location of the swelling matrix. Further, the local internal elastic deformation of the matrix is needed to compute the pseudo-sink terms describing the matrix dilution in the messenger transport equations, eqs 3-16 and 3-23. To accomplish these objectives, we use the phenomenological Tanaka-Hocker-Benedek (THB) model[108] for elastically expanding hydrogels. This theory has been shown to be fairly accurate and it is also described by a simple differential equation, whose analytical solution can be explicitly integrated into an overall model describing the fluid flow-membrane dynamics-messenger transport. The origin of the THB model lies in linear elasticity theory, and incorporates an assumed Stokes-like friction force between the interlinked polymer network and the liquid solution during the swelling process. A brief derivation is given here starting from the general quasi-steady Cauchy equation of motion for a linear elastic body undergoing a small deformation,

$$\nabla \cdot \boldsymbol{\tau}(\mathbf{x}) + \mathbf{F}(\mathbf{x}) = 0, \quad \mathbf{x} \in \Omega_{mat} \tag{3-29}$$

where $\mathbf{F}$ is the body force term, and τ_{ij} is the stress tensor for a linear elastic body. The constitutive relation between the stress and strain is linear and defined by the Hook's law,

$$\tau_{ij} = K\frac{\partial u_k}{\partial x_k}\delta_{ij} + 2G\left(\frac{1}{2}\left(\frac{\partial u_i}{\partial x_j} + \frac{\partial u_j}{\partial x_i}\right) - \frac{1}{3}\frac{\partial u_k}{\partial x_k}\delta_{ij}\right) \tag{3-30}$$

where u_k is the equilibrium displacement vector, K is the bulk modulus of elasticity, G is the modulus of elasticity in shear, and δ_{ij} is the Kronecker delta function. In his pioneering paper,[107] Tanaka et al. postulated that a friction force in the polymer matrix should be simply added as a body force to Cauchy's equation. In this case, the interactions between the polymer network and the solvent contained in the matrix are represented by an effective friction coefficient f. By combining Tanaka's postulation $\mathbf{F} = -f(\partial \mathbf{u}/\partial t)$ and eq 3-30 , the so-called "THB hydrogel model"[108] can be derived on the basis of eq 3-29:

$$\frac{\partial \mathbf{u}}{\partial t} = \frac{G}{f}\nabla^2\mathbf{u} + \frac{K + G/3}{f}\nabla(\nabla\cdot\mathbf{u}), \quad \mathbf{x}\in\Omega_{mat} \tag{3-31}$$

In the considered cases (a) and (c), we assumed that the swelling of the protein matrix is uniformly triggered by the monovalent cations diffusing into the matrix from the extracellular solution, owing to the fast diffusion in the liquid solution. Here, we further assume that the matrix is swelling uniformly and the spherical symmetry is maintained in the linear deformation process as observed in the spherical hydrogel system.[108] Then, for the cases (a) and (c) wherein $t_{char} \sim t_{diff,matrix}$, eq 3-31 can be reduced to the following dimensionless, spherically-symmetric form,

$$\frac{D_{matrix}}{D_{swell}}\left(\frac{\partial u_r}{\partial t}\right) = \frac{\partial}{\partial r}\left\{\frac{1}{r^2}\frac{\partial\left(r^2 u_r\right)}{\partial r}\right\} \tag{3-32}$$

where u_r and r are the radial displacement and the spatial variable in the radial direction, respectively, and $D_{swell} = (K + 4G/3)/f$ represents an apparent collective

diffusion coefficient determined by the elastic properties and the effective friction coefficient. In a typical case of $G \ll K$, the collective diffusion coefficient is approximated by $D_{swell} \sim K/f$ and is experimentally found to be ~1.4x10^{-11} m^2/s.[68] The eigenvalue problem for eq 3-32 was solved analytically[108] using an initial condition of the uniform, positive osmotic pressure π_0 that ensures the stress balance throughout the gel, $\sigma_{ij} = \pi_0 \delta_{ij}$, and the boundary conditions of central symmetry, $u(0,t) = 0$, and stress-free outer interface of the gel, $\sigma_{rr} = 0$ at $r = a$. The initial condition can be further reduced to the equation, $K\nabla \cdot \mathbf{u} = \pi_0$, with the solution of the THB model given by[108]

$$u_r(r,t_0) = \Delta a_0 \left(\frac{r}{a}\right), \quad \Delta a_0 = \frac{\pi_0 a}{3K} \tag{3-33}$$

where π_0 is the initial uniform stress (positive osmotic pressure), a is final radius after swelling, Δa_0 is the total displacement of the interface, and $a - \Delta a_0$ is the initial radius of the matrix. The general solution of eq 3-32 is given by a series expansion in terms of eigenfunctions[108] for the radial displacement of the gel,

$$u(r,t) = 6\Delta a_0 \sum_{n=1}^{\infty} \frac{(-1)^n}{n\pi} \left\{ \frac{\cos(\beta_n r)}{\beta_n r} - \frac{\sin(\beta_n r)}{(\beta_n r)^2} \right\} \exp\left(-\hat{D}_r \beta_n^2 t\right), \quad r \in \Omega_{mat} \tag{3-34}$$

where $\beta_n = n\pi/a$ are the eigenvalues, $n = 1,2,...,\infty$, and the diffusivity ratio is defined by $\hat{D}_r = D_{swell}/D_{matrix}$. For reference, in both cases (a) and (c) considered in this work, the diffusivity ratio is around 7.0. Finally, it should be noted that the solution u represents the point displacement inside the network from its final equilibrium location after the matrix is fully swollen, that is, $u \to 0$ everywhere at $t \to \infty$. Accordingly, the divergence of the displacement velocity is

$$\nabla\cdot\frac{\partial \mathbf{u}(r,t)}{\partial t}=6\Delta a_0\sum_{n=1}^{\infty}\frac{(-1)^n}{n\pi}\left\{-\hat{D}_r\beta_n^2\frac{\sin(\beta_n r)}{r}\right\}\exp\left(-\hat{D}_r\beta_n^2 t\right),\quad r\in\Omega_{mat} \tag{3-35}$$

The simplified THB model presumes that the swelling polymer matrix has a sharp interface separating the protein network from the liquid environment, and the radius of the moving interface is therefore given by $R_{matrix}(t)=a-u(a,t)$ with the diffusivity ratio assumed constant during the swelling process.

3.2.2.7 Electroanalysis: Faradaic Current Response

Once the messenger concentration field is determined everywhere, the Faradaic current response of the microelectrode can be obtained by integrating the local molecular flux over the active surface area of the electrode, including the conversion from dimensionless to dimensional form,

$$I(t)=nFD_{bulk}C_0R_0\int_{\partial\Omega_{elec}}\nabla C\cdot\mathbf{n}\,dA,\quad \mathbf{x}\in\partial\Omega_{elec} \tag{3-36}$$

where F is the Faraday constant, n is the valence number of the released neurotransmitter [n=4 for cases (a) and (b), and n=2 for case (c)]. Alternatively, the local current density distributed along the electrode surface can be computed as $i(t)=dI(t)/\left(R_0^2\,dA\right)=nFD_{bulk}C_0\left(\nabla C\cdot\mathbf{n}\right)_{\partial\Omega_{elec}}/R_0$.

3.2.3 Boundary Integral Formulation

The intimately coupled governing equations for the fluid flow and neurotransmitter transport are reformulated in terms of integral equations based on the fundamental solutions of the Stokes and Laplace differential operators, and the system of integral equations is then solved by the boundary element method (BEM) and by the dual

reciprocity boundary element method (DRBEM). The general integral solution of the Stokes flow equation, $-\nabla p+\mu\nabla^2\mathbf{v}=0$, combines contributions from the single-layer and the double-layer surface integrals,[13,19]

$$\omega v_j(\mathbf{x}_0)=-\int_{\partial\Omega}\tau_{ik}(\mathbf{x})n_k(\mathbf{x})G_{ij}(\mathbf{x},\mathbf{x}_0)dA(\mathbf{x})+\overset{p.v.,\,\mathbf{x}_0\in\partial\Omega}{\int_{\partial\Omega}}v_i(\mathbf{x})T_{ijk}(\mathbf{x},\mathbf{x}_0)n_k(\mathbf{x})dA(\mathbf{x}) \qquad (3\text{-}37)$$

where $\omega=0$ for $\mathbf{x}_0\notin\Omega$, $\omega=8\pi\mu$ for $\mathbf{x}_0\in\Omega-\partial\Omega$, and $\omega=4\pi\mu$ for $\mathbf{x}_0\in\partial\Omega$ on a sufficiently smooth boundary. The unit surface normal vector n_k points into the fluid domain, v_i and τ_{ik} represent the velocity and hydrodynamic stress fields, respectively. Note that when the source point is located at the boundary, $\mathbf{x}_0\in\partial\Omega$, the double-layer contribution from the Stresslet has to be interpreted in the sense of Cauchy principal value because of the stronger singularity in the integral kernel T_{ijk}. The fundamental solution, the Stokeslet, and its corresponding stress field, the Stresslet, are available for the homogeneous system,[13]

$$G_{ij}(\mathbf{x},\mathbf{x}_0)=\frac{\delta_{ij}}{r}+\frac{r_i r_j}{r^3},\quad T_{ijk}(\mathbf{x},\mathbf{x}_0)=-6\frac{r_i r_j r_k}{r^5} \qquad (3\text{-}38)$$

respectively, where δ_{ij} is the Kronecker delta function, and $\mathbf{r}=\mathbf{x}\text{-}\mathbf{x}_0$ and $r=|\mathbf{x}\text{-}\mathbf{x}_0|$ are, respectively, the position vector and the distance between the field and the source points. The boundary integral formulation based on the Stokes fundamental solution has been proven a very efficient technique to solve many fluid-fluid interfacial problems with various viscosity ratios.[20,21] This technique was also adapted in our previous work focused on the AFM-fluid-membrane interactions,[1,2] albeit with a simplified assumption for the viscosity ratio $\lambda=\mu_{env}/\mu_{cyt}=1$. Similarly, the problem in hand is solved by combining the boundary integral solutions of the flow fields in the cytosol and

environmental fluid domains (i.e., inside and outside of the cell) through the use of the dynamic interface boundary condition (eq 3-26). We skip the lengthy derivation and only present the final solution of the flow field for the combined intra and extra cellular simulation domains expressed in a dimensionless form,

$$4\pi v_j(\mathbf{x}_0) = a_1 \int_{\partial\Omega_{mem}} \Delta f_i G_{ij}\, dA + a_2 \int_{\partial\Omega_{mem}}^{p.v.,\mathbf{x}_0 \in \partial\Omega_{mem}} v_i T_{ijk} n_k dA + a_3 \int_{\partial\Omega_{elec}+\partial\Omega_{mat}} f_i G_{ij}\, dA + a_4 \int_{\partial\Omega_{mat}}^{p.v.,\mathbf{x}_0 \in \partial\Omega_{mat}} v_i T_{ijk} n_k dA \quad (3\text{-}39)$$

Here, $v_i(\mathbf{x}_0)$ is the velocity field, $f_i = \tau_{ik} n_k$ is the surface force acting on the interface, and the surface force jump condition Δf_i in the first integral is given by eq 3-26, which can be physically interpreted as the source density acting on the fluid from the fused membrane surface. The coefficients a_1 through a_4 in eq 3-39 can be derived for an arbitrary physical domain with sufficiently smooth boundaries and equal to:

$$a_1 = \frac{-1}{1+\lambda},\quad a_2 = \frac{1-\lambda}{1+\lambda},\quad a_3 = \frac{1}{1+\lambda},\quad a_4 = \frac{-\lambda}{1+\lambda} \quad \text{for} \quad \mathbf{x}_0 \in \partial\Omega_{mem} \quad (3\text{-}40a)$$

$$a_1 = \frac{-1}{\lambda},\quad a_2 = \frac{1-\lambda}{\lambda},\quad a_3 = \frac{1}{\lambda},\quad a_4 = -1 \quad \text{for} \quad \mathbf{x}_0 \in \partial\Omega_{mat} + \partial\Omega_{elec} \quad (3\text{-}40b)$$

$$a_1 = \frac{-1}{2\lambda},\quad a_2 = \frac{1-\lambda}{2\lambda},\quad a_3 = \frac{1}{2\lambda},\quad a_4 = \frac{-1}{2} \quad \text{for} \quad \mathbf{x}_0 \in \Omega_{env} \quad (3\text{-}40c)$$

$$a_1 = \frac{-1}{2},\quad a_2 = \frac{1-\lambda}{2},\quad a_3 = \frac{1}{2},\quad a_4 = \frac{-\lambda}{2} \quad \text{for} \quad \mathbf{x}_0 \in \Omega_{cyt} \quad (3\text{-}40d)$$

The boundary only formulation in a three-dimensional space for the linear fluid system is exact and complete at this point. However, the complexity of the integral formulation can be further reduced for an axisymmetric system by using the cylindrical coordinate transformation $(x, y, z) = (x, \sigma\cos\theta, \sigma\sin\theta)$ and expressing the fundamental solutions, the Stokeslet and the Stresslet, in terms of the Green's functions of the ring-source type. As shown in Figure 3.1, x is the coordinate along the axial direction, σ is the coordinate

along the radial direction, and θ is the azimuthal angle. Thus, the surface integral in the cylindrical coordinate system is $dA = \sigma d\theta d\ell$ where $d\ell$ denotes a line integral. For an axisymmetric system, the unknown functions Δf_i, f_i, and v_i are independent of the azimuthal angle so that the azimuthal integration needs to be performed only for the Green's function and for its corresponding stress field, leading to the final solution of the three-dimensional axisymmetric problem in terms of one-dimensional integrals only,

$$v_\alpha(\mathbf{x}_0) = a_1 \int_{\partial\Omega_{mem}} M_{\alpha\beta}\Delta f_\beta \, d\ell + a_2 \overset{p.v., \mathbf{x}_0 \in \partial\Omega_{mem}}{\int_{\partial\Omega_{mem}}} Q_{\alpha\beta\gamma} v_\gamma n_\beta d\ell + a_3 \int_{\partial\Omega_{elec}+\partial\Omega_{mat}} M_{\alpha\beta} f_\beta \, d\ell + a_4 \overset{p.v., \mathbf{x}_0 \in \partial\Omega_{mat}}{\int_{\partial\Omega_{mat}}} Q_{\alpha\beta\gamma} v_\gamma n_\beta d\ell \tag{3-41}$$

where coefficients $a_1 \sim a_4$ are defined in eq 3-40, the Greek symbols α, β and γ denote either x or σ directions, and the kernel functions $M_{\alpha\beta}$ and $Q_{\alpha\beta\gamma}$ are the general coordinate transformation matrices for the Stokeslet and the Stresslet in the Cartesian coordinate system, which can be expressed in terms of the complete elliptic integrals of the first and second kinds.[13,21] Notice that in eq 3-41, either the traction or the interfacial velocity has to be specified along the integration domain boundary $\partial\Omega_{mat}$. This is an important observation for proper integration of the Eulerian fluid flow-membrane deformation analysis with the Lagrangian simulation of the granule matrix swelling, if the matrix is free to move. Indeed, if the interfacial velocity is specified, the presence of the surface force resulting from solving eq 3-41 would violate the boundary condition required for the validity of the THB model, i.e., $\sigma_{rr} = 0$ at $r = a$. Likewise, if the vanished surface force is specified, the spherically symmetric shape of the granule matrix will be distorted by the nonuniform interfacial velocity distribution resulting from solution of eq 3-41. Rigorously, this contradiction may only be overcome by full

simulation of the two-phase granule system. Here, as a first approximation we assume that the interfacial velocity vanishes on the matrix interface, but the matrix surface force is compromised in a way that the symmetric swelling behavior is imposed. In principle, one may assign a single velocity value from the experimental observation to advance the granule in the Eulerian coordinate system and, consequently, to relocate the Lagrangian coordinate system affixed to the center of the granule matrix. However, such an approach requires detailed biological information that is currently not available.

By substituting eq 3-41 into eq 3-27, the integral formulation of the local membrane constraint equation, eq 3-27, takes the final compact form,

$$a_1 \int_{\partial\Omega_m} \Pi_1(\mathbf{x},\mathbf{x}_0)\Delta f_\beta(\mathbf{x})d\ell(\mathbf{x}) + a_2 \overset{p.v.,\,\mathbf{x}_0\in\partial\Omega_t}{\int_{\partial\Omega_m}} \Pi_2 v_\gamma n_\beta d\ell + a_3 \int_{\partial\Omega_{elec}+\partial\Omega_{mat}} \Pi_1 f_\beta d\ell + a_4 \int_{\partial\Omega_{mat}} \Pi_2 v_\gamma n_\beta d\ell = 0 \quad (3\text{-}42)$$

with the modified integral kernels expressed as:

$$\Pi_1(\mathbf{x},\mathbf{x}_0) = \sigma(\mathbf{x}_0)t_\alpha(\mathbf{x}_0)\frac{\partial M_{\alpha\beta}(\mathbf{x},\mathbf{x}_0)}{\partial s(\mathbf{x}_0)} + M_{\sigma\beta}(\mathbf{x},\mathbf{x}_0), \quad \Pi_2 = \sigma t_\alpha \frac{\partial Q_{\alpha\beta\gamma}}{\partial s} + Q_{\sigma\beta\gamma} \quad (3\text{-}43)$$

where α, β and γ denote either the σ or x directions, and the unknown local membrane tension/compression force is obtained implicitly from $\Delta\mathbf{f}$ given by eq 3-26. The exact integral forms for the tangential derivatives of these kernel functions, $\partial M_{\alpha\beta}/\partial s$ and $\partial Q_{\alpha\beta\gamma}/\partial s$, can be expressed in terms of the complete elliptic integrals of the first and second kinds and are listed in Appendix D for completeness.

The integral formulation for the transient, nonhomogeneous, diffusion-advection system requires special treatment for the domain integration since a simple fundamental solution is not available for the system with a nonuniform velocity field. A convenient way to treat a diffusion-dominated system (low Peclet number) in an integral form is to

use the fundamental solution of the Laplace operator. By applying the weighted residual formulation and the general Green's identity, the integral form of the general mass transport equation can be expressed as follows:

$$-\omega C + \int_{\partial\Omega}\left(G_L \frac{\partial C}{\partial n} - C\frac{\partial G_L}{\partial n}\right) dA = \int_{\Omega} G_L \; b \; dV \tag{3-44}$$

where ω=1 for $\mathbf{x}_0 \in \Omega$ and ω=1/2 for $\mathbf{x}_0 \in \partial\Omega$ on a sufficiently smooth boundary. At the right hand side, the transient, advection, and the nonhomogeneous terms are grouped into a pseudo-source term b as a local intensity of the domain integral,

$$b = \frac{\partial C}{\partial t} + \mathbf{v}\cdot\nabla C + g\,C \tag{3-45}$$

where $g = \nabla\cdot\partial\mathbf{u}/\partial t$ is given by eq 3-35. The three-dimensional fundamental solution of the Laplace operator is $G_L = 1/4\pi r$ with $r = |\mathbf{x}\text{-}\mathbf{x}_0|$ being the distance between the source and field points. The reason for not using an obvious time-dependent fundamental solution for the transient diffusion operator but including the contribution of the initial condition into the pseudo-source term is because in the axisymmetric transformation, the time dependent Green's function contains a complex combination of trigonometric and exponential functions so that the explicit form of the ring-source type integral kernel cannot be readily established. On the other hand, the fundamental solution of Laplace operator has a simple form amenable for transformation using elliptic integrals.

In summary, we have developed a complete system of linear integral equations, eqs 3-41, 42, and 44, that, combined with the boundary conditions, eqs 3-17a~g, 20a~e, and 24a~g, and the dynamic interfacial conditions, eqs 3-26 and 34, constitute a boundary value problem for the coupled fluid flow/messenger transport/membrane deformation problem describing the local dynamics of a single exocytotic event. The numerical

technique applied for solving the integral equations is described in detail in the following section with a focus on the numerical approximation of the domain integrals.

3.3 Numerical Implementation

An approach to numerical solution of the Stokes flow system for two fluids (e.g., intra and extra cellular solutions) interacting via interfacial coupling governed by the membrane biomechanics has already been reported.[1,2] Therefore, the focus of this discussion is on numerical solution of the boundary integral equation (eq 3-44) that describes the transient molecular messenger transport. Specifically, the source term on the right hand side of eq 3-44 requires special treatment in order to accurately evaluate the value of the integral. Among several numerical approximation methods, the dual reciprocity boundary element method (DRBEM), originally proposed by Nardini and Brebbia,[110] appears to be the most promising strategy for constructing the domain integral. General reviews of BEM and DRBEM are available in the literature.[111,112] The key idea behind DRBEM is to expand the nonhomogeneous term in terms of its values at the nodes using a set of interpolating functions. The approximation for the source term is expressed as a finite sum of interpolating functions at the boundary and internal nodes,

$$b_m(\mathbf{x}_m) = \sum_{k=1}^{N+L} \phi_{mk}(\mathbf{x}_m, \mathbf{x}_k)\,\alpha_k, \quad m = 1,2,\ldots,N+L \tag{3-46}$$

where N and L are the total numbers of the boundary elements and of the selected internal nodes, respectively. The interpolation function ϕ_{mk} is an $N+L$ by $N+L$ square matrix whose elements depend on the location of a pair of collocation points $(\mathbf{x}_m, \mathbf{x}_k)$. The column vector α_k is a set of unknown interpolation coefficients to be determined, and the

column vector b_m is the nonhomogeneous or pseudo-source term evaluated at each nodal point. If b_m includes the derivative of the unknown variable, another set of interpolating function is required for the approximation, and such a case is often seen in the transport equations. The selection of internal nodal points can be considered extra degrees of freedom for the approximation. There is no rigorous mathematical rule to justify how to select the arbitrary internal nodes and how many nodes should be selected, but physically it is reasonable to increase the degrees of freedom by clustering nodes in the solution domain where it is expected to have a higher gradient of the dependent variable. The discussion and numerical tests of various approximation functions can be found in the literature.[113,114] The numerical experiments showed that the radial basis functions, given by low degree polynomials, are often a good choice for the interpolation functions,

$$\phi_{mk} = 1 + r_{mk} + r_{mk}^2 + \ldots \tag{3-47}$$

where the radial basis $r_{mk} = |\mathbf{x}_m - \mathbf{x}_k|$ is the distance between a pair of boundary or internal nodes. In practical computations, only one set of basis functions is required and we use $\phi = 1 + r$. Using this simplest basis function, the corresponding particular solution f_{mk} can be readily obtained that satisfies the Poisson equation

$$\nabla^2 f_{mk} = \phi_{mk} \tag{3-48}$$

This solution is $f = r^2/6 + r^3/12$, and now eqs 3-44, 46, and 48 can be combined to obtain an approximation of the domain integral given by

$$-\omega C + \int_{\partial\Omega} \left(G_L \frac{\partial C}{\partial n} - C \frac{\partial G_L}{\partial n} \right) dA = \int_{\Omega} G_L \sum_{k=1}^{N+L} \left(\nabla^2 f_{mk} \right) \alpha_k \, dV \tag{3-49}$$

We can factor the coefficients α_k out of the integral, and transform the domain integral to a boundary only integral formulation by applying the Green's second identity to the Laplace operator,

$$-\omega C + \int_{\partial\Omega}\left(G_L\frac{\partial C}{\partial n} - C\frac{\partial G_L}{\partial n}\right)dA = \sum_{k=1}^{N+L}\alpha_k\left[-\omega f_{mk} + \int_{\partial\Omega}\left(G_L\frac{\partial f_{mk}}{\partial n} - f_{mk}\frac{\partial G_L}{\partial n}\right)dA\right] \tag{3-50}$$

It should be noted that the bracketed term on the right hand side of eq 3-50 depends on the domain geometry only, and the contribution from the source function is embedded into the unknown set of coefficients α_k. Since the series expansion in eq 3-46 is based on a set of linearly independent functions, ϕ_{mk} is invertible and α_k are uniquely determined by

$$\alpha_k = \sum_{m=1}^{N+L}(\phi)^{-1}_{km} b_m \tag{3-51}$$

where $(\phi)^{-1}_{km}$ are the elements of the inverse of the matrix ϕ_{mk}.

The pseudo-source term b_m includes two derivatives: the time derivative can be approximated by any time-domain finite difference scheme, whereas the spatial derivative requires further approximation for the concentration field using a second set of unknown interpolating coefficients β_k in the linearly independent series expansions,

$$C_m(\mathbf{x}_m) = \sum_{k=1}^{N+L}\phi_{mk}(\mathbf{x}_m, \mathbf{x}_k)\,\beta_k, \quad \nabla C_m(\mathbf{x}_m) = \sum_{k=1}^{N+L}(\nabla\phi)_{mk}\,\beta_k \tag{3-52}$$

Similarly, β_k is uniquely determined by

$$\beta_k = \sum_{m=1}^{N+L}(\phi)^{-1}_{km} C_m \tag{3-53}$$

By combining eqs 3-52 and 53, including the result into eq 3-46, and then substituting the latter into eq 3-51, the equation for the unknown set of coefficients α_k takes the final form:

$$\alpha_k = \sum_{m=1}^{N+L} \left(\phi^{-1}\right)_{km} \left\{ \frac{\partial C_m}{\partial t} + \mathbf{v}_m \cdot \sum_{k=1}^{N+L} (\nabla \phi)_{mk} \left(\sum_{p=1}^{N+L} (\phi)_{kp}^{-1} C_p \right) \right\} \tag{3-54}$$

where the velocity field is obtained by solving the Stokes fluid system at each time step.

Similar to the fluid system, in the axisymmetric case, the surface integrals in eq 3-50 can be reduced to line integrals by using the polar coordinate transformation. For axisymmetric applications, Šarler[115] further suggested the axisymmetric forms of the interpolation function $\bar{\phi}_{mk}$ and the particular solution $\bar{f}_{mk}$. Thus, eq 3-50 can be written as a line integral form, with indices i and j representing the source and field points of the discretized domain,

$$-\omega C_i + \int_{\partial\Omega_j} \left(M_L \frac{\partial C}{\partial n} - C Q_L \right) d\ell = \sum_{k=1}^{N+L} \alpha_k \left[-\omega \bar{f}_{ik} + \int_{\partial\Omega_j} \left(M_L \frac{\partial \bar{f}_{jk}}{\partial n} - \bar{f}_{jk} Q_L \right) d\ell \right] \tag{3-55}$$

Here, the ring-source type Green's function M_L and its normal gradient Q_L, the new interpolation function $\bar{\phi}$, the particular solution $\bar{f}$ and its normal gradient $\partial \bar{f} / \partial n$ are listed in Appendix E for completeness.

With the background developed in the previous paragraphs, the algorithm for solving the system of coupled integral equations for the problem can be described as a sequence of the following steps. First, the computational domain boundaries $\partial\Omega_{matrix}$, $\partial\Omega_{mem}$, and $\partial\Omega_{elec}$ (Figure 3.1) are partitioned into a finite number of boundary elements $\partial\Omega_j$ with j being an element index. A few nodal points are also distributed in the aqueous environment for solving the pseudo-source term of the transient diffusion-advection

equation. For each element, the physical parameters are assumed constant, and by substituting the element level integration into the integral equations 3-41, 42, and 55, the system is rearranged into a set of linear algebraic equations. The next step is to cast the system into a fully implicit form and set up the system of algebraic equations describing the initial and boundary conditions. The discretized forms of equations 3-41 and 42 are lengthy but straightforward, and therefore we only present the discretization of the diffusion-advection system, eq 3-55, in the Appendix F in order to clarify some matrix manipulations. The moving boundary problem is simultaneously solved for two sets of unknowns: (i) $\mathbf{v}(\mathbf{x} \in \partial\Omega_{mem})$, $\mathbf{f}(\mathbf{x} \in \partial\Omega_{elec}, \partial\Omega_{mat})$ and $\gamma(\mathbf{x} \in \partial\Omega_{mem})$ for the fluid motion system, and (ii) $C(\mathbf{x} \in \Omega_{env}, \Omega_{mat})$ and $\nabla_n C(\mathbf{x} \in \partial\Omega_{elec}, \partial\Omega_{mat})$ for the diffusion-advection transport system. The internal velocity field $\mathbf{v}(\mathbf{x} \in \Omega_{env})$ required for the diffusion-advection system is calculated at the post-processing stage upon solving the Stokes flow problem at each time step, and the membrane evolution is advanced following the local velocity field at every time step using a simple time integration at each collocation point. The matrix interface is explicitly defined by the analytical solution $a - u(a,t)$ of the THB model, eq 3-34. Further, the computational domains Ω_{mat} and Ω_{env} both share the same boundary nodes at the matrix-environment interface $\partial\Omega_{mat}$, so that the coupling boundary conditions requiring continuity of the messenger concentration and its flux across the interface, eqs 3-17f,g and 24f,g, can be simultaneously solved. In the next section, we discuss the numerical results and qualitatively compare them to the experimental results for the three types of vesicles considered in this study.

3.4 Results and Discussion

3.4.1 Case (a): Serotonin Release by an Electroporated Granule of the Mast Cell

While the simulations are performed in terms of dimensionless variables, all simulation results, with an exception of the messenger concentration, are presented in dimensional form to facilitate comparison with the experimental data. Figure 3.2 presents the numerical results for the benchmark case (a): an electroanalysis of serotonin transport in an electroporated granule of the mast cell. Although electroporation induces opening of the pores throughout the vesicle membrane, the simplest configuration with only two pores, located at the north and south poles of the vesicle, is simulated here. This simplification was suggested by Marszalek et al.,[68] and it is based on the observation that for the large vesicles of the mast cell (radius about 2.5 μm[91]) only the messengers released from the pore that is in immediate vicinity to the microelectrode would contribute to the detected electrical current. Further, in the analysis it is assumed that the pores are initially fully closed and they expand with a constant velocity, assumed to be close to the maximum pore expansion velocity $V_0 = 10 \sim 25$ μm/s,[91,93] until the membrane (shown by the bold solid line in Figure 3.2B) is completely open. Figure 3.2A shows the radial distributions of the transient local current density $i(t)$ at the microelectrode surface at several consecutive time instants for the simulations with $V_0 = 25$ μm/s. As expected, at the very beginning the current density is at its maximum at the center of the electrode, as it corresponds to the shortest travel distance for the released serotonin to reach the electrode. Furthermore, the peak magnitude increases in time and it broadens, owing to an increase in the size of the pore opening with time. The normalized serotonin local

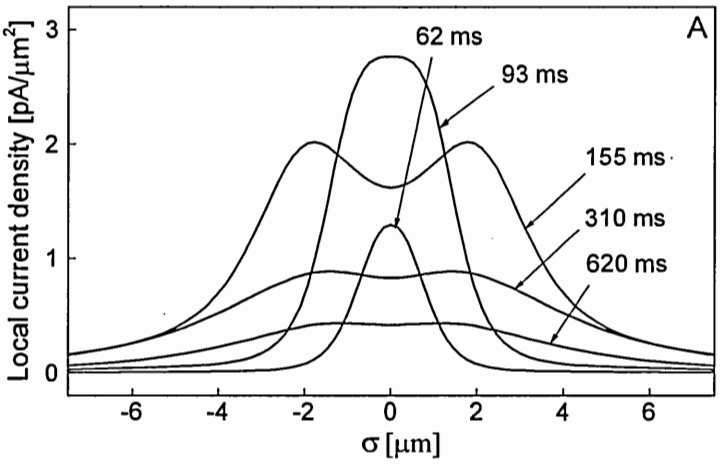

Figure 3.2 Simulation results for the serotonin release by an electroporated granule: (A) Transient, radially distributed local current density $i(\sigma,t)$ at the microelectrode for several consecutive time instances (pore expansion velocity $V_0 = 25\,\mu m/s$ is constant), (B) Normalized instantaneous serotonin concentration field C/C_0 superimposed with the velocity field resulting from swelling of the granule matrix (time instant $t = 155$ ms and pore expansion velocity $V_0 = 25\,\mu m/s$), (C) Transient total current response $I(t)$ (solid lines) for pore expansion velocities $V_0 = 25\,\mu m/s$ and $V_0 = 10\,\mu m/s$, superimposed with the dynamics of the radius of the swelling matrix (dash line) expanding from 2.5 μm to 3.375 μm.

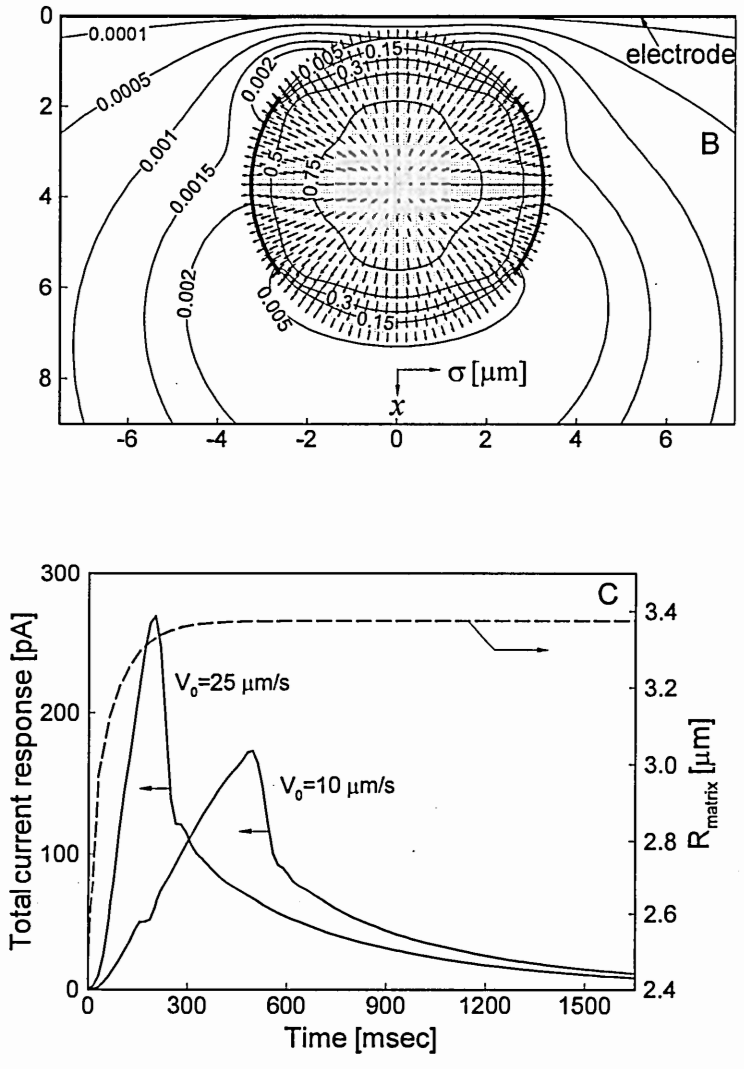

Figure 3.2 (cont'd)

concentration field shown in Figure 3.2B indicates that the concentration gradient is the greatest within the granule matrix near the interface, owing to almost two orders of magnitude smaller diffusivity of the D_{matrix} as compared to the bulk solution diffusivity D_{bulk}. This implies that the main resistance to the messenger transport is near the interfacial region of the matrix. However, the rate of the matrix swelling, as given by the swelling velocity $\partial u(r,t)/\partial t$, is also the greatest near the interface, at least in the beginning of the process, which partially improves the situation by contributing to a decrease in the near interface transport resistance due an increase in the surface area. It is interesting to note that the maximum of the matrix swelling velocity gradually moves from the interfacial area towards the granule center (not shown in Figure 3.2) with time as the matrix approaches its fully swollen state.

The surface integration of the transient current density profiles (Figure 3.2A) results in the transient total current response $I(t)$ detected by the microelectrode, as shown in Figure 3.2C. It should be noted that the current density distribution in Figure 3.2A is shown for the case of the pore expansion velocity V_0~25 μm/s, whereas the total current responses in Figure 3.2C are shown for two representative pore expansion velocities of 10 and 25 μm/s. It is clear from Figure 3.2C that the current spike is stronger (maximum ~270 pA) and its duration is shorter (~300 ms) in the case of the higher pore expansion velocity. This is because at the higher expansion velocity, the pore opens much faster establishing a bigger in size window for the messenger release from the granule matrix. And the size of this release window is the parameter that controls the total rate of the messenger release (and, in turn, the total current signal) since the local messenger flux is

essentially independent of the magnitude of the pore expansion velocity, at least in the beginning of the process when the granule matrix is messenger-rich and undiluted. It is important to state that the characteristic rising time (~180 ms) and the magnitude of the total microelectrode current (~270 pA) for the case of $V_0 = 25\,\mu m/s$ are very consistent with the experimental results.[68,91] This favorable comparison of the predictions with the experiments for the current rising phase is also important for one additional reason: as shown by the dash line in Figure 3.2C, it is also during the rising phase of the process when the matrix swells from its initial condensed state, R_{matrix} = 2.5 μm, to nearly an equilibrium, fully swollen state of R_{matrix} = 3.375 μm. Thus, this indicates that accounting for the matrix swelling dynamics is essential to understanding the sequence of the exocytotic events.

As the pore opening continues to expand, the radial distribution of the current density or a messenger flux reaching the electrode changes dramatically from unimodal to bimodal due to local depletion of the matrix near the center portion (e.g., compare t=93 ms versus t=155 ms in Figure 3.2A). The bimodal current density distribution features peaks of the smaller magnitude (due to overall matrix dilution as the neurotransmitters are being released), but much greater broadening owing to matrix expansion. Overall, however, the total current detected by the electrode continues to increase, albeit at a slower rate, due to an increase of the total open pore window through which the messengers can leave the matrix. Eventually, an increase in the pore size can no longer compensate for a serotonin dilution in the fully swollen matrix, and the total current (Figure 3.2C) begins to decrease with the dynamics of the messenger diffusion in the matrix being the rate-defining process. The process continues until ~2000 ms when the

entire serotonin content of the matrix is released to the environment. In comparison with the experiments,[68,91] the model overpredicts the rate of drop in the total current signal after the peak value is reached. The reason for this disagreement, we believe, lies in the fact that the pore expansion velocity is probably not constant, but decreases as the pore opens more and more. It is probably a good assumption to use the maximum pore expansion velocity in the beginning of the process when the membrane/pore system is farthest from the equilibrium, and that is why the comparison with experiments is satisfactory in this case. The only way to test this hypothesis is to perform more detailed biological studies of the exocytotic pore opening dynamics leading to the time resolved pore expansion velocity measurements.

3.4.2 Case (b): Neurotransmitter Release by a Small and Clear Synaptic Vesicle

Prior to analyzing the simulation results in this case, a brief discussion is needed of the proper boundary condition and the elastic properties for the membrane for self-consistent formulation. This is important because, unlike in the previous case (a) of a freely suspended vesicle, the simulations must now include the fluid-membrane interactions. This requires an additional boundary condition to specify the membrane tension force γ that should produce the prescribed pore expansion velocity. Here, we only consider a reduced dynamic model of the membrane, which is driven purely by the local tension force with vanished edge energy and the bending rigidity. There are several reasons why we neglected the contribution from the bending energy. First is purely computational as it is very difficult to achieve a stable, fully converged and physically meaningful solution of the problem that involves such a large curvature on a very small

spatial scale in the vicinity of the pore area where the vesicle and the cell membranes merge. Second reason is more physical and it rests on the assumption that the bending energy alone cannot provide a driving force that is sufficiently strong to overcome the edge energy and the fluid viscous force while unfolding the membrane leading to the rupture of the small fusion pore. Finally, the short-range electrostatic forces between the connecting edges of the fused vesicle and cell membranes may also reduce the potential of the bending rigidity and the pore edge energy to mediate the membrane unfolding process. Clearly, further investigation is required to address these issues in full details.

Our previous analysis[1] shows that a surface tension γ (a Lagrange multiplier in the Helfrich's curvature energy theory) has to be assigned at the far field (a truncation point in the simulations) of the membrane in order to obtain mathematically well-behaved or physically reasonable results for the local tension/compression force. Similarly in this case, a certain finite tension/compression force γ has to be prescribed in the far field in order to provide a driving force for unfolding of the membrane and pore opening with the required expansion velocity V_0. Indeed, Monck et al.[116] provide experimental evidence that the membrane of the secretory vesicle is under a tension force by measuring the reduction of the capacitance during the fusion event. Thus, it is very possible that both the vesicle and the cell plasma membranes are pre-stressed during the fusion process. Once the fusion pore is opened, the tension forces in the cell and vesicle membranes acting outward along the radial direction near the neck area of the pore work together in order to overcome the edge energy of the small fusion pore, leading to unfolding of the membrane. A simple way to incorporate this idea into our model is by assigning certain finite tension force γ at $\sigma \to 0$ (the center of the vesicle membrane) and $\sigma \to \infty$ (far-

field of the cell membrane, truncated in simulations at the dimensionless radius $\sigma = 8$), while everywhere else the local tension force should satisfy the membrane constraint equation (eq 3-27). Such an approach is rather general and provides a way to impose a required/measured tension force at any place in the membrane if needed for validation the biological hypothesis. For example, if a particular protein is speculated to provide radial tension or circumferential contraction edge energy near the pore area, such a hypothesis can be indirectly verified using this macroscopic approach.

The results of numerical simulations of the neurotransmitter transport by a small and clear synaptic vesicle are shown in Figure 3.3 We used the pore size suggested by Stiles et al.[92] with the pore radius of 1 nm initially and increasing to 5 nm during the pore expansion. Figures 3.3A and B show the instantaneous radial current density distributions and the normalized neurotransmitter concentration field, respectively, for the case of high pore expansion velocity up to $V_{avg} \sim 63 \mu m/s$. The magnitude of the current density is always maximized at the center of the electrode, which corresponds to the shortest diffusion path through the pore for the released neurotransmitter to reach the electrode. This is in contrast to transition from the uni-modal to the bimodal current density distribution observed in the previously discussed case of an electroporated granule of the mast cell. This is because there is no matrix in the case of a small and clear synaptic vesicle, and diffusivity of the neurotransmitters in the extracellular fluid is much higher than that in the matrix. It is also interesting to note that the magnitude of the current density increases during the first 18 μs, and then begins to decrease owing to dilution of the vesicle with time. This is perhaps better observed on the transient total current response, shown in Figure 3.3C for three representative pore expansion velocities of

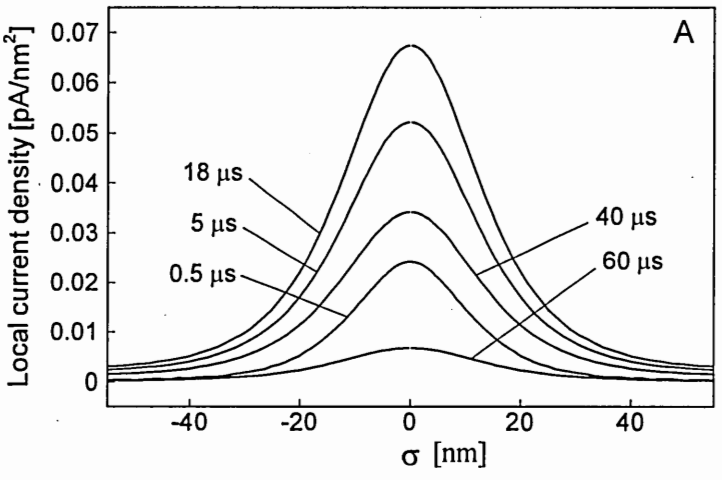

Figure 3.3 Simulation results of the neurotransmitter release by a small and clear synaptic vesicle: (A) Transient, radially distributed local current density $i(\sigma,t)$ at the microelectrode for several consecutive time instances (average pore expansion velocity $\sim 63\,\mu m/s$), (B) Normalized instantaneous serotonin concentration field C/C_0 (time instant $t=10$ μs and an average pore expansion velocity $\sim 63\,\mu m/s$), superimposed with the final membrane position (dotted line) with the pore opening radius of 5 nm, (C) Transient total current response $I(t)$ for the average pore expansion velocities $V_{avg}=63$, 20 , and 0 $\mu m/s$.

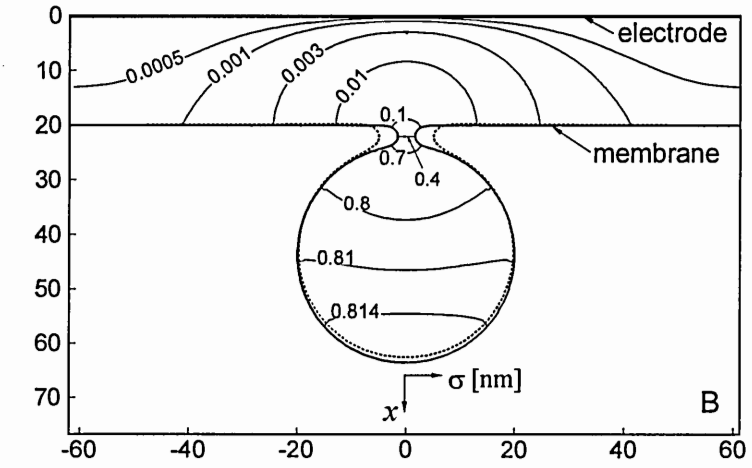

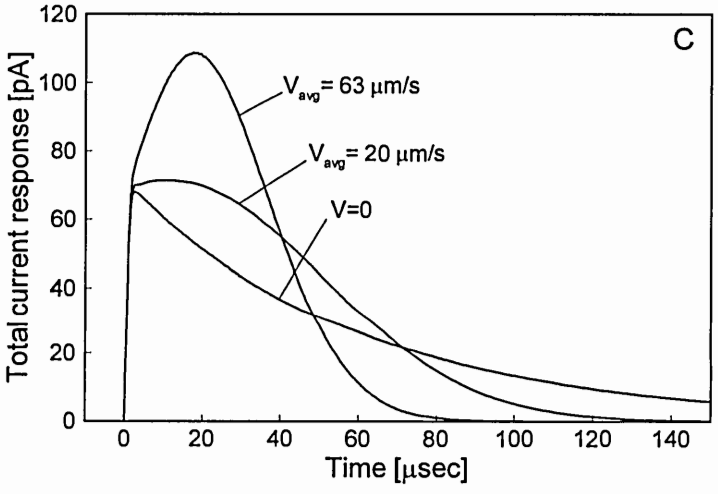

Figure 3.3 (cont'd)

0, 20, and 63 μm/s. This is the curve that is measured in the typical exocytosis experiments involving microelectrode. The model predicts a spike shape which is similar to the experimental results[85] with an almost instantly rise phase and a longer decaying tail. However, the time rate of rise to the maximum total current response, computed to be less than 18 μs, is overpredicted as compared to the reported experimental values of 25~80 μs[92] and ~90 μs[85] for the neurotransmitter release from the small synaptic vesicles. Further, our predictions in Figure 3.3C indicate that the current spike can reach a value greater than 100 pA, which is more than an order of magnitude higher than the experimental result, ~5 pA, measured by Bruns and Jahn.[85] We are not sure what causes such a significant difference between predictions and experiments in both the amplitude and time constant. There could be important phenomena that we overlooked in our model, but a simple analysis of the experimental data[85] suggests that for the measured 4200 messenger molecules released during the time period of 160 μs, the current spike magnitude should reach a value at least of the order of several tens of picoampere, not ~5 pA, measured by Bruns and Jahn.[85] The reasons for this inconsistency of results may include poor control of the microelectrode position during the experiment (e.g., tilted electrode) resulting in a smaller amount of detected neurotransmitters, the finite rate of the electrode reaction kinetics (although less probable), additional resistances to the messenger transport within the narrow pore, a reduction in the number of messengers released due to the "kiss and run" events, or a smaller diffusivity of the lumen region inside the small vesicle as compared to the bulk extracellular environment value that we assigned to it in our simulations.

Despite the lack of quantitative agreement, some interesting qualitative conclusions can be drawn by comparing the current response in Figure 3.3 for the cases with an expanding (non-zero pore expansion velocity $V_{avg} \sim 20\mu m/s$ & $63\mu m/s$) and a stationary ($V_0 = 0$) pore. The simulation results show that the pore opening velocity is not important for the messenger transport during the initial few microseconds when three current signals (for different velocities) rise quickly and overlap until the amplitude reaches ~70 pA. This suggests that the neurotransmitter diffusion within the vesicle or in the extracellular environment, but not in the neck area of the pore, initially dominates the transport. However, once the concentration fields within the extracellular and intravesicular environments are established, the rate of neurotransmitter release becomes limited by diffusion through the constriction provided by the pore. As a result, greater is the pore expansion velocity, the bigger in size pore becomes, and the smaller is the pore resistance to the transport. As a result, the current spike magnitude increases and the current decay time constant decreases drastically with an increase in the pore expansion velocity (see Figure 3.3C). This is well illustrated by the normalized local concentration field shown in Figure 3.3B which indicates the greatest concentration gradient within the neck area of the narrow fusion pore, proving that this is the area of the bottleneck resistance to the molecular transport.

3.4.3 Case (c): Adrenaline Release by a Medium Size Vesicle in the Chromaffin Cell

In the case (c), we apply an integrated messenger transport-release model to simulate the adrenaline release by a medium size vesicle in the chromaffin cells. The biophysical parameters from the simultaneous amperometry and membrane capacitance measurements by Amatore et al.[89] are used as in input in our simulations. The process

dynamics is treated as a two-stage process, as conceptually suggested by amperometric experiments showing a constant rate of the neurotransmitter release (the current plateau) through a stable fusion pore (the "pore-release" stage with the low pore expansion velocity) followed by a sudden increase in current through an enlarged pore with the granule matrix totally exposed to the extracellular environment (the "full-fusion" stage with high pore expansion velocity).[89] The model we propose to interpret the experiments is different from the semi-empirical kinetics model developed by Amatore and co-workers [88] in the following important aspects: (i) We account for the fact that a granule matrix is surrounded by the lumen fluid before and after the small fusion pore is opened as well as during the swelling process. We do not impose the constraint on the matrix interfacial area exposed to the fluid medium, but allow it to expand according to the THB swelling model. Similar molecular diffusivities are assumed for the monovalent ions in both lumen and extracellular fluids that trigger the matrix swelling, and, thus, local electroneutrality is maintained owing to an immediate replenishment of counter-ions that surround the granule matrix during the swelling process. (ii) Both the membrane dynamics and messenger transport are simultaneously considered with a minimum number of physically meaningful tuning parameters to match the experimental results. (iii) The pore edge energy is not considered in our model. Instead, the surface energy is indirectly evaluated from the computed local tension force γ rather than approximating the nonequilibrium pore energy using equilibrium thermodynamics. The magnitude of the tension force far away from the pore is assigned based on the apparent pore opening velocity measured in experiments. (iv) The advection effect induced by the suddenly enlarged pore promotes and locally redistributes the molecular flux to the electrode

surface and is accounted for. It is demonstrated that the advection contribution is significant, especially for the cases with higher Peclet number flows corresponding to the vesicles whose size are comparable to or greater than the nominal size ($R_0 \geq 150$ nm) of vesicles in chromaffin cells and for a higher pore opening velocity ($V_0 \geq 18$ μm/s).

The simulation results shown in Figure 3.4 are intended to match the experimental data[89] and obtained for the following conditions. During the "pore-release" stage, the messengers are released through a small pore with initial radius ~0.5 nm which slowly expands to ~4.2 nm, corresponding to the average pore expansion velocity of about 0.37 μm/s. After 10 milliseconds, the "pore-release" process transition into a "full-fusion" stage with a much higher pore expansion velocity about 18 μm/s. In the simulations, the change in the pore expansion velocity is enforced by changing the magnitude of the membrane tension γ from 2.0 nN/m (the dimensionless tension force ~0.1) to 1.2 μN/m (the dimensionless tension force ~60), respectively, in the far-field and at the symmetry plane of the membrane, as discussed in great details in the previous section for the simulation case (b). For the reference, the membrane tension force required to overcome the viscous drag force alone during the fast opening stage is three order of magnitude smaller than an estimated edge energy (~ 1 mN/m)[89] and four order of magnitude smaller than the rupture tension force of a lipid bilayer membrane.[33] For the simulations, we estimated the pore expansion velocities for the slow "pore-release" and fast "full-fusion" stages of exocytosis from the transient measurements of change in the capacitance induced by the fact that the vesicle membrane area is incorporated into the cell membrane.[88] The swelling matrix is assumed to expand symmetrically from the dimensionless radius 0.7 to 0.945 with a ~150% increase in volume,

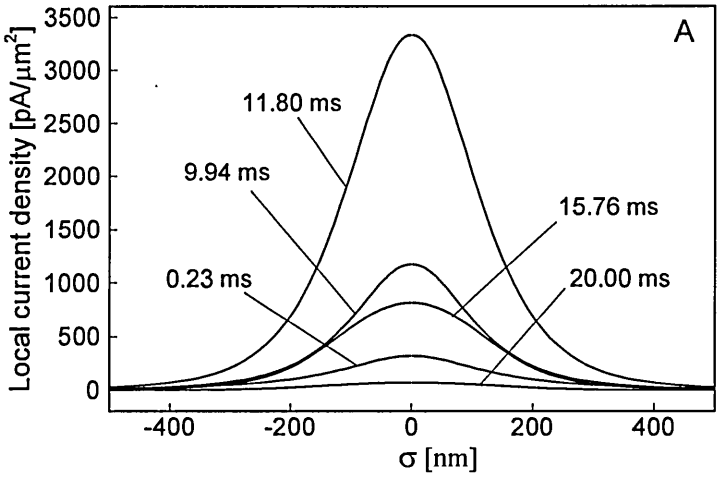

Figure 3.4 Simulation results of the adrenaline release by a medium size vesicle in the chromaffin cell: (A) Transient, radially distributed local current density $i(\sigma,t)$ at the microelectrode for several consecutive time instances, t=0.23, 9.94, 11.80, 15.76, and 20.00 ms, (B) Instantaneous snapshots of the dynamic membrane evolution corresponding to the time instances of the plot in A, superimposed with the initial and final interfacial locations (dash lines) of the granule matrix, (C) Transient total current response $I(t)$ in the two-stage pore opening process (a slow "pore-release" at 0.37 μm/s and a fast "pore-fusion" at 18 μm/s), superimposed with the case (dashed line) simulated where the fluid advection effect is negected.

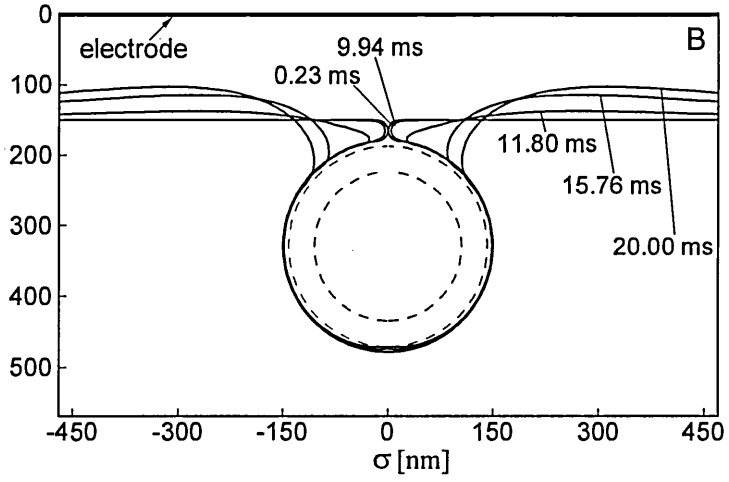

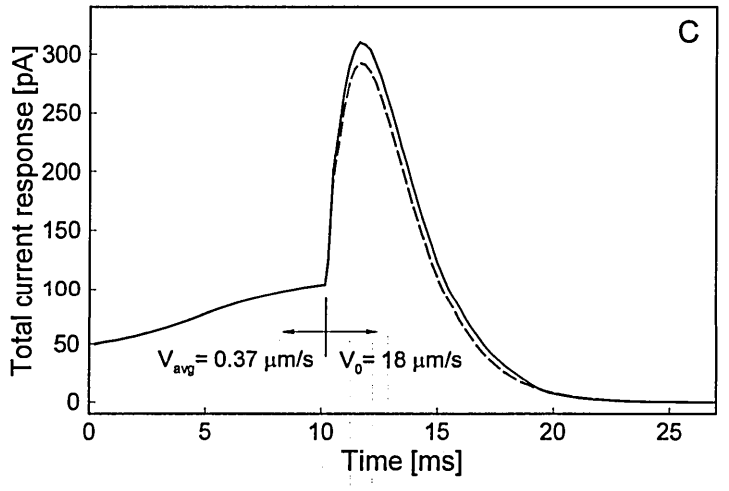

Figure 3.4 (cont'd)

the matrix diffusivity is set to $D_{matrix} \sim 2.0 \times 10^{-12}$ m^2/s, and both of these conditions are approximated from the measurements of an electroporated granule matrix.[68,91]

In Figure 3.4A, the local current density as detected by a microelectrode increases slowly during the initial "pore-release" stage with maximum amplitude at the center of the electrode. After 10 ms, the fast "full-fusion" stage starts and the current density sharply and almost instantly rises to its maximum value around 3300 pA/μm^2, with a rise time of only 2 ms, and then slowly decays with the time to full decay being about 8 ms. A drastic change in the messenger flux (as expressed by the total microelectrode current) for the slow-to-fast stage transition is also well illustrated by Figure 3.4C, where the signal slowly increases from 50 to 120 pA during the "pore-release" stage followed by an almost immediate current spike to a peak value of up to 310 pA in the beginning of the "full-fusion" stage. The simulated shape of the current spike and its decay as shown in Figure 3.4C qualitatively agree very well with the experimental results.[88,89,90] However, there is a lack of quantitative agreement between our predictions using the medium vesicle size ($R_0 = 150$ nm) and the experimental data[88,89,90]: the predicted magnitude of the current spike is four to five times higher, i.e., predicted 310 pA versus measured 60~80 pA, and the decay is three to four times faster, predicted 10 ms versus measured 30~40 ms. This significant difference between predictions and experiments in both the amplitude and the time constant could be due to several reasons. First, we suspect that adrenaline oxidation on the microelectrode may not be infinitely fast (as assumed by experimentalists), and the finite electrode kinetics would result in the diminished molecular flux oxidized at the electrode and consequently reduced the current spike amplitude and increased decay time. Unfortunately, the electrode kinetics was not

characterized by Amatore et al.[89,90], making inclusion of kinetics effects into simulations very speculative. Other possible reasons include the greater diffusion resistance due to possible lower-than-assumed diffusivity of the water molecules and counter-ions in the lumen fluid between the granule matrix and the vesicle membrane (see Figure 3.4b), the nonhomogeneous diffusivity inside the granule matrix caused by partially exposed matrix interface and highly localized swelling dynamics[88], or a very complex interaction induced by an extrusion behavior of the granule matrix. Neither of the above mentioned facts has been characterized experimentally, and, therefore, it would have been be too speculative to include these effects into our simulations. It would suffice to say that the first model developed for the electroporated granule matrix in the simulation case (a) should be accurate enough to predict the diffusion behavior of the partially exposed matrix[88] as long as symmetric elastic deformation of matrix is a reasonable approximation. However, for the case involving the matrix extrusion behavior, there is presently no physically sound understanding of the process to be able to mathematically model this complex phenomenon. Whether the matrix extrusion significantly affects the membrane dynamics remains an open question from both the experimental and theoretical perspectives.

Despite the lack of detailed biological information for further theoretical comparison of many competing hypotheses of exocytosis, we do observe several interesting phenomena exclusively from the modeling results: (i) If the matrix swelling is relatively symmetric by allowing the fluid medium flow in and fill the gap between the matrix interface and the vesicle membrane, the second half of the membrane unfolding process during the "full-fusion" stage, that is, when the opening angle[89] $\alpha(t) \geq \pi/2$, does not play any significant role in the messenger release process, at least for the case when the pore

opening velocity is close to the order of 18 μm/s. (ii) During the "pore-release" stage and the initial rise phase of the "full-fusion" stage (the time period 0~12 ms), the rate of the messenger release is hindered by the narrow fusion pore. As a result, the two-step slow-to-fast rising behavior in the current signal (Figure 3.4C) is determined by the pore opening size, which corresponds in turn to the two different pore opening velocities. The current decay at the end of the "full-fusion" stage (time course ≥ 12 ms in Figure 3.4C) is, however, obviously limited by the messenger diffusion within the swollen matrix. (iii) The inclusion of advective transport associated with the bulk extracellular fluid motion enhances the amplitude of the current spike, e.g., by 5~6% for a pore opening velocity of 18 μm/s, as shown by comparison with the simulation with a neglected advection (dashed line) in Figure 3.4C. Thus, the fact that the Peclet number given by eq 3-8 is small (only $4.5x10^{-3}$) can be rather misleading as it artificially neglects an increasingly important messenger transport by advection in the region away from the fusion pore, where the diffusion flux is much smaller than the species transport by bulk flow induced by the large membrane deformation (see Figure 3.4B). Therefore, use of a single characteristic diffusion length scale (e.g., given by the vesicle radius) is not appropriate to justify the simplifications in the diffusion-advection transport equation for such a multiscale process as vesicular exocytosis. Instead, several characteristic length scales (e.g., vesicle radius, pore opening radius, electrode-to-membrane distance) should be locally used to facilitate reduction in the model complexity without loss of the accuracy.

3.5 Conclusions

In summary, we have developed a new, integrated theoretical model of the bio-transport phenomena underlying dynamics of exocytotic events for several different vesicle/cell types. The model considers the opening and expansion of the fusion pore, vesicular matrix swelling, elastic membrane unfolding, and molecular messenger release in the limits of the continuous fluid transport and elasticity theories. Only a simplified dynamic model of the membrane is used here that assumes that the membrane evolution is driven purely by the local tension force with vanished edge energy and the bending rigidity. The solution of the problem is obtained using the combination of the boundary integral and the dual reciprocity boundary element methods. The simulation results are qualitatively compared with the experimental data from the literature of the *in vitro* electroanalytical measurements of the Faradaic current resulting from the messenger oxidation on the microelectrode. The results are significant as they provide new insight and basic understanding of the slow and fast steps of an exocytotic sequence, allowing verification of competing hypotheses on what control/limit the messenger release during exocytosis. The following specific conclusions can be drawn:

- Proper selection of the time and length scales involved in exocytosis allows one to simplify significantly the dynamic models of the process without loss of the essential biophysical features of the process.

- Accounting for the matrix swelling dynamics is essential for correct prediction of the rise time in the electric current signal in the electroanalytical measurements of exocytosis using microelectrode. A simple Tanaka-Hocker-Benedek (THB) model[107,108] for elastically expanding hydrogels has been shown to be fairly accurate for prediction of

the matrix swelling dynamics, and its analytical solution can be explicitly integrated into an overall model describing the fluid flow-membrane dynamics-messenger transport during exocytosis.

- The transient change in the pore expansion velocity is very important for prediction the total amount of the messengers released during different stages of the exocytotic process. Unfortunately, currently available experimental data is limited to the estimates of the maximum pore expansion velocity, which is not sufficient for development of fully accurate dynamic models.

- The shape and behavior of the predicted and measured total current vs. time response curves are in good agreement, but there is lack of quantitative agreement in the time and magnitude of the total current rise recorded by the electrode in tracking the neurotransmitter release from a small and clear synaptic vesicle and a medium size vesicle in the chromaffin cell. It is possible that the model we developed does not take into account other important phenomena that limit the release process, but this would require further, more detailed experimental work to refine the biophysical fundamentals beyond the current state of understanding. There is also an apparent inconsistency in the reported experimental results, which may partially explain the lack of agreement between the predictions and measurements.

- In the case of a small and clear vesicle, the pore expansion velocity is very important to define the magnitude of the current rise and the time constant for the current decay, but only after the neurotransmitter release and the exocytosis dynamics become limited by diffusion through the neck area of the fused pore connecting the cell and vesicle membranes.

- In the case of a medium size vesicle in chromaffin cells, a two-stage pore opening process appears to be a suitable conceptual formalism to describe the essential features of the messenger release dynamics. It consists of the slow "pore-release" and fast "full-fusion" processes, when the pore expands with distinctly different opening velocities. The simulations reveal that an initial rise in the rate of the messenger transport is defined mainly by the pore opening velocity, whereas the decay time when the current slowly decreases from its peak value is limited by the messenger diffusion inside of the granule matrix. Further, it is demonstrated that the advection transport of molecular messengers induced by large membrane deformations may be significant and cannot be neglected solely based on the small magnitude of the global flow Peclet number.

- The size of the opening pore and the pore opening velocity play the key roles in controlling the messenger release kinetics in all three simulated cases, in a way they affect the rising time and the spike amplitude of the total current response. The internal diffusion of messengers inside of the granule matrix is important only for the non-clear vesicles, cases (a) and (c), as it extends the decay time of the release process until the matrix is fully depleted.

CHAPTER 4

Conclusions and Recommendations for Future Work

Unlike any man-engineered systems, biological systems can hardly be fully understood through theoretical analysis and modeling, at least based on the current level of basic knowledge in the field. However, theoretical analysis definitely has its value in comparative hypothesis verification, gaining an insight on the system behavior in response to environmental and physiological changes, and defining the directions for potential research. Therefore, it is very important to clearly understand and state the validity limits of the biophysical theories. In this chapter, such limits are summarized for the models developed in this thesis work followed by the discussion on the recommendations for future work, including needed experiments, routes for extension of the theories, and numerical simulation methods.

The model of AFM-biomembrane hydrodynamic interactions described in Chapter 1 neglects a number of possibly important effects, including a heterogeneous nature of the cell membrane, the structure and properties of the cytoskeleton network, as well as presence of various internal organelles. This model is perhaps the best suited to describe the interactions between an AFM tip and a simplest prototype of the cell membrane such as the planar sheet of a synthetic lipid bilayer or a self-assembled vesicle. To extend the model application to more realistic cell membranes, the following studies are recommended for future research:

1. The effect of a much higher viscosity of the intercellular environment (cytosol) as compared to the extracellular solution should be incorporated into an analysis.

There is no fundamental difficulty in this extension and it could be done by adopting the same theoretical approach as the one described in Chapter 3 of this thesis.

2. In general, a viscoelastic fluid model is expected to be a more general description of the cytosol as a structured liquid due to possibly high concentration of charged proteins packed inside of the cell. However, such a model can only be realized if the viscoelastic properties of the protein solutions are experimentally determined and properly correlated with the protein type and concentration.
3. The local arrangement of the membrane cytoskeleton network may provide a major resistance to the membrane deformation. The current model can only be applied for an isotropic and homogeneous membrane or membrane/skeleton system. For a system with the more complex structural organization and an anisotropic skeleton structure, the investigation of the AFM tip-membrane interactions in the limit of small deformations may require a full three-dimensional analysis near the scanning area rather than an axisymmetric analysis performed here. This is not presently clear and further investigation is needed on both experimental and theoretical fronts.
4. In addition to vesicles forming a lipid bilayer structure of the cell membrane, the proteins, carbohydrates, and other complex molecules are integrated into a cell membrane to perform many physiological functions of the biological cell. Only in the case when the integrated molecules are uniformly distributed within the cell membrane, it is perhaps possible to simplify the membrane structure by using a homogenization-like algorithm to resolve the heterogeneities and accommodate

the multiscale phenomena. The analysis of a confluent monolayer of cells may also adopt this strategy for a simplified analysis. An alternative approach would require the molecular discrete-level modeling. However, the latter can be reliably implemented only if the fine details of the molecular structure and force interactions are known, and also requires significant computational simplifications to obtain meaningful results for such a complex system as a biological cell. In the future, one shall consider this possibility only if the molecular dynamics simulations can shake hands with the continuum models in self-consistent fashion without currently used numerous *ad hoc* numerical manipulations.

5. The first step in the experimental verification of the model is investigation of AFM noncontact imaging of the scale-up model membrane system, such as the planar sheet of a synthetic lipid bilayer membrane or a giant vesicle. By labeling the membrane area of interest with fluorescent labels, it should be possible to trace the dynamics of the membrane deformation using a conventional or a confocal microscope and use the particle imaging/tracing technique to construct a three-dimensional topological map of motion. Environment parameters such as imposed flow or pressure fields and the membrane-supporting device, such as a micropipette, can be easily integrated into the theoretical model developed in Chapter 1.

In Chapter 2 the analysis focused on the effect of the membrane electric field on the AFM imaging of a bilayer membrane in a dilute environment. In most AFM experiments, this effect is not significant as the experimentalists commonly use the high ionic strength

buffers to minimize the thickness of the Debye electric double layer, thereby essentially screening the membrane electric field. However, there is a need for characterizing the electric double layer in many systems of interest to colloidal and interfacial sciences, whether or not a biological sample is involved. Thus, the practical value of the mathematical method and the solution technique developed in Chapter 2 is much broader and not limited to the biological applications only. It should be perhaps viewed as a more universal theoretical tool when one wants to use the AFM to investigate the complex microfluidic systems involving interactions between solid and soft matters on the small scale. The following studies are recommended for future research:

1. The limitation of the low zeta potential of the charged membrane used in the present study to linearize the electric system should be resolved. It can be done by solving the nonlinear Poisson-Boltzmann equation for the electric potential in the electrically-responsive media by using a numerical technique that can handle the domain integral terms such as, for example, the dual reciprocity boundary element method described in Chapter 3 of this thesis.
2. It should be possible to combine a simplified algebraic model for an electric double layer used in this thesis and the van der Waals forces in the framework of the DLVO theory of colloidal stability[16] if the parameters of the constitutive equation for the interaction potential energy can be experimentally determined.
3. The interplay between the short- and long-range electric force interactions may become important when focus is on the analysis of asymmetric and locally nonhomogeneously charged membranes. This definitely warrants further

investigation even on the purely theoretical ground and requires transition to a fully three-dimensional analysis.

Finally, in Chapter 3 the mathematical models are developed to analyze the molecular messenger release process and compared with experimental results for various vesicle and cell types. Careful design of the model system is necessary for meaningful comparison of the transient simulations and *in-situ* experiments. Only through such a direct comparison, a better understanding may emerge of the linkage between the exocytosis triggering mechanisms at the molecular level, an individual exocytotic event, and the signaling at the cell and tissue levels. Many limitations made in design of the theoretical models discussed in Chapter 3 are either because of the lack of biological information or owing to the computational challenges. The following studies are recommended for future research:

1. The granule matrix of the vesicle serves as an active engine for release of the chemical messengers. It is necessary to develop a basic experimental method that can measure the effective transport properties (e.g., diffusivity) of the messengers stored in the matrix at a submicron scale to properly describe transport of messengers under realistic conditions. The transport property measurements have to be coupled with the development of suitable predictive models for polymer-solvent interactions at various transition states.
2. The two-phase polymer model should be able to better describe the nonhomogeneous, nonlinear, and asymmetric deformation of the vesicle granular matrix. By incorporating the mechanisms of momentum transport for both polymer and solvent phases, limitations of the phenomenological THB elastic

model and the simplified boundary condition at the matrix/solution interface can be relaxed. A *mesoscale* modeling technique such as Lattice Boltzmann Simulations (LBS) can be recommended to simulate the hydrodynamics of non-equilibrium two-phase polymer system. These hydrodynamic interactions can then possibly be incorporated into the phenomenological THB hydrogel model or be directly combined with other possible continuum models for the multiscale analysis of the granule swelling. In addition, the matrix swelling induced by membrane tension also needs to be resolved.

3. A consistent thermodynamic theory for evaluation for the edge energy of the fusion pore is still needed to settle many inconsistencies in the experimental results reported in the literature. Detailed measurements are needed to identify the responsible proteins and to quantify the molecular forces acting along the radial and circumferential directions of the membrane during the pore opening process. It is possible and straightforward to extend the model of the post fusion exocytosis dynamics developed in Chapter 3 if a better knowledge of the local membrane tension force is available through direct measurements using, for example, an optical tweezer technique[117]. Knowledge of the driving tension force can lead to a more accurate prediction of the fluid flow pattern, the membrane unfolding dynamics, and thus the messenger transport phenomena into the extracellular medium.
4. The difficulties in computational solution of the governing boundary integral equations increase drastically as more and more various transport mechanisms need to be simultaneously considered. Development of hybrid approaches that

combine the field solution methods with the purely boundary integral method is recommended. For example, the finite volume schemes can be used for solving the nonlinear, heterogenous species transport equations, while the Stokes integral solutions can still be used to solve the linear fluid system with complex moving boundary conditions in the limit of low Reynolds number flows.

5. The uncertainties of electroanalysis, such as the electrode size, geometry, position, electrochemical properties and sources of contaminations, the redox reaction kinetics, among others can be critical factors that prevent accurate correlations between theoretical predictions and electroanalytical measurements. Thus, only carefully calibrated measurements on the well-characterized biological system can provide a route for development of realistic models of the exocytosis leading to complete fundamental understanding of the cell signaling.

APPENDIX A

Fundamentals of Boundary Integral Method

The boundary integral method is used for computationally efficient solution of the models developed in chapters 1 through 3. All theoretical formalism is expressed in the integral form and solved by the boundary element method (BEM) and dual reciprocity boundary element method (DRBEM) in a coherent way. Fundamentals of this solution methodology are briefly reviewed in this Appendix.

Engineering and physical problems are commonly formulated in terms of a system of differential equations for certain continuous field variables. However, equivalent integral formulation is often preferred since it directly represents the governing physics, for example, in the case of conservation laws in fluid mechanics and heat/mass transfer. In addition, integral equations can be more effectively solved as compared to the differential equations, and the numerical schemes are inherently preserving conservation laws. In general, there are two different ways to obtain the integral formulation: using the variational principle and the weighted residual technique. As a starting point, the variational principle assumes that the physical problem can be expressed in terms of a minimum value of a certain functional. The functional is in an integral form and usually represents the system energy, action, distance, surface area or any physical quantity that makes sense to minimize. However, it is often very difficult to find the variational formulation for more complex problems, for example, the fluid flow problems. Therefore, to circumnavigate this problem one needs to work in a reverse way – first, derive the differential system from the first principles governing the physics of the

problem, then use the weighted residual method to define the equivalent integral formulation. Weighted residual method is used for both finite element (FEM) and boundary element (BEM) applications. At the transformation level, the difference between FEM and BEM is that FEM only performs integration by parts once to obtain the weighted residual formulation (weak formulation), whereas BEM requires second integration by parts to generate an adjoint integral formulation (or reverse formulation). For example, consider a differential equation, $Lu = f$, where L is a linear differential operator and u is an unknown function which satisfies this equation with given boundary conditions. If the inverse operator L^{-1} exists and if there is an integral operator with the kernel $G(x,t)$ such that

$$\left(L^{-1}u\right)(x) = \int G(x,t)u(t)dt \tag{A-1}$$

then we can express the solution of the problem as

$$u(x) = LL^{-1}u(x) = L\int G(x,t)u(t)dt = \int LG(x,t)u(t)dt \tag{A-2}$$

Clearly, the only way for the statement A-2 to be true for all continuous functions u is if the kernel $G(x,t)$ is defined by a distribution solution of the fundamental equation

$$LG(x,t) = \delta(x-t) \tag{A-3}$$

where $G(x,t)$ is the fundamental solution or the free space Green's function of the differential operator L, and $\delta(x-t)$ is Dirac delta function with the field point x and the source point t. The idea of fundamental solutions of linear differential operators is essential to apply integral analysis as a solution technique.

Further, let's now consider the general Green's identity given by[118,119]

$$\int_{\Omega}\left(vLu - uL^{*}v\right)dV = \int_{\partial\Omega}\mathbf{J}(u,v)\cdot\mathbf{n}\,dA \tag{A-4}$$

where u and v are continuous functions with continuous derivatives of the order of L (let m be the differential order of L), L^* is an adjoint operator of L defined by the inner product $<Lu,v>=<u,L^*v>$, and the conjunct term $\mathbf{J}$ is a bilinear vector form of functions u and v with highest derivative of the order $m-1$ or less. Here the solution domain Ω is bounded in R^3 by a sufficiently smooth boundary $\partial\Omega$, dV is the volume element, and dA is the surface element of the boundary with an outward unit normal $\mathbf{n}$. Obviously, a frequently seen Green's theorem is a special case of eq A-4 in the case of the Laplace differential operator.

The fundamental solution, eq A-3, and the general Green's identity, eq A-4, are two most important ingredients of the integral or inverse formulation that lead to the weighted residual method. Assuming u is the solution we want, the residual of eq A-1 can be set to zero in an average sense over the field Ω weighted by a function G, i.e.,

$$\int_{\Omega} G(Lu - f)d\Omega = 0 \tag{A-5}$$

The weighting function G, also called the basis function, is used for construction of the approximation solution. By comparing with the general Green's identity (eq A-4), eq A-5 can be expressed as

$$\int_{\Omega} uL^*G\,dV + \int_{\partial\Omega} \mathbf{J}\cdot\mathbf{n}\,dA - \int_{\Omega} Gf\,dV = 0 \tag{A-6}$$

Equation A-6 is now a complete integral form of the differential equation (A-1). And, if G is the fundamental solution that satisfies the singularly-forced adjoint differential equation,

$$L^*G = -\delta(x,t) \tag{A-7}$$

We can further substitute eq A-7 into eq A-6 to obtain the exact solution for the source point located inside the solution domain ($t \in \Omega - \partial\Omega$),

$$u = \int_{\partial\Omega} \mathbf{J} \cdot \mathbf{n}\, dA - \int_{\Omega} Gf\, dV \tag{A-8}$$

In summary, eqs A-6 and A-8 provide a very powerful way to find the solution of the original differential equation. The presented integral formulation is built on the classical mathematical theory by George Green, who introduced the Green's function in 1828[120], and many recent developments. Among the latter, the potential theory[121] was developed in the early nineteen century, and it established the foundation for application of integral equations in the boundary value problems for conduction heat transfer, electrostatic, magnetostatic, elastic, and potential flow. Also the integral equation theory[122,123] (most importantly, the Fredholm's alternative theorem) and the differential/integral linear operator theory[119,124] provided the grounding work for BEM. When computers became available in mid 20th century, numerical implementation of BEM has received many attentions for solutions of very complex integral equations. The numerical algorithms for BEM implementation can be found in many references,[111,125,126] and the generic solution sequence can be summarized as follows:

(i) express the governing differential equations in an integral form using the weighted residual method,

(ii) find the fundamental solution of the differential operator,

(iii) reduce the integral equation to a boundary only integral using Green's identity, Gauss divergence theorem, or direct integration by parts,

(iv) discretize the integral equation to a system of linear algebraic equations, and

(v) solve the linear system using one of the available matrix inversion methods.

The greatest advantage of using the boundary integral method is that it allows for reducing the dimensionality and hence the complexity of the problem by an order of one, and, for a number of systems, only the boundary integrals (i.e., no domain integrals) are remained in the final integral formulation of the problem. From the numerical point of view, computations are very efficient, and only a fairly small amount of computer memory is required for variable storage. Other advantages include:

(i) integral solution is semi-analytical, thus, one can obtain a better physical insight into the simulation results,

(ii) discretization of the differential operator is not needed, that prevents truncation errors and numerical instabilities

(iii) computer coding is relatively concise compared with traditional finite difference, finite volume, or finite element methods.

However, these advantages come with a number of difficulties arising when the problem becomes complicated:

(i) derivation of the fundamental solution can be very difficult,

(ii) singular integration requires special efforts and has to be done very carefully,

(iii) solvability condition raised by the integral equation, in general, is difficult to prove rigorously, and

(iv) if the domain integrals cannot be transformed to the boundary integrals, direct domain discretization or further approximations such as DRBEM are required and the integral method may lose its computational superiority.

APPENDIX B

Integral Solution of Stokes System

Quasi-steady Stokes flow problem can be conveniently solved by using boundary integral method. The theory was originally proposed by Lorentz in 1907. In fact, Lorentz reciprocal theorem[17] gives a pairwise relation between the flow velocity and its corresponding stress by linking the real flow in the actual physical domain to the so-called Stokeslet flow induced by the corresponding Green's function, the Stokeslet. The integral solution was later outlined by Odqvist[18] and Ladyzhenskaya[19] by considering the flow field as a superposition of the contributions from a single layer potential (the flow induced by the continuously distributed point force, Stokeslet) and a double layer potential (the flow induced by continuous point stress, Stresslet). The details of the theory development and numerical implementation of the integral formulation can be found in references[13,19]. According to Ladyzhenskaya,[19] the nonhomogeneous Stokes equation and its singularly-forced adjoint equation can be written as

$$\nabla \cdot \boldsymbol{\tau}(\mathbf{v}, p) = \mu \nabla^2 \mathbf{v} - \nabla p = \mathbf{S} \tag{B-1}$$

$$\nabla \cdot \boldsymbol{\tau}'(\mathbf{v}', p') = \mu \nabla^2 \mathbf{v}' + \nabla p' = \delta(\mathbf{x} - \mathbf{x}_0)\hat{\mathbf{e}} \tag{B-2}$$

respectively, where $\mathbf{S}$ is a combination of nonhomogeneous terms, $\mathbf{v}$ and p are the velocity and pressure solutions of the nonhomogeneous Stokes system with dynamic viscosity μ, $\mathbf{v}'$ and p' are the fundamental velocity and pressure solutions for the singularly-forced system (B-2), $\mathbf{x}$ and $\mathbf{x}_0$ denote the field and source points, respectively, and $\boldsymbol{\tau}$ and $\boldsymbol{\tau}'$ are the corresponding second order stress tensors. Similarly to eq A-4, the general Green's identity for the Stokes problem was derived by Ladyzhenskaya,[19]

$$\int_{\Omega}\left[v_i'\left(\mu\nabla^2 v_i-\frac{\partial p}{\partial x_i}\right)-v_i\left(\mu\nabla^2 v_i'+\frac{\partial p'}{\partial x_i}\right)\right]dV=\int_{\partial\Omega}\left(\tau_{ij}'v_i n_j-\tau_{ij}v_i' n_j\right)dA \qquad \text{(B-3)}$$

here the unit surface normal vector n_j points into the fluid domain Ω. Note that if the system is homogeneous and the source point $\mathbf{x}_0$ does not belong to the domain Ω, the right hand side of eq B-3 reduces to the Lorentz Reciprocal Identity,[17] expressed in differential form as $\nabla\cdot\left(v_i'\tau_{ij}-v_i\tau_{ij}'\right)=0$. Now, combining eq B-2 with the continuity equation, $\nabla\cdot\mathbf{v}'=0$, the fundamental solutions for velocity $\mathbf{v}'$ (Stokeslet), pressure p', and their corresponding stress tensor $\boldsymbol{\tau}'$ (Stresslet) can be derived by Fourier transform.[19] Finally, since the continuity equation is satisfied by both $\mathbf{v}$ and $\mathbf{v}'$, eq B-3 provides a mechanism to derive an integral form of nonhomogeneous Stokes equation by combining Stokeslet, Stresslet, and contributions from the nonhomogeneous terms,

$$\begin{aligned}&\frac{1}{8\pi\mu}\int_{\Omega}S_i(\mathbf{x})G_{ij}(\mathbf{x},\mathbf{x}_0)\,dV(\mathbf{x})\\&\quad+\frac{1}{8\pi\mu}\int_{\partial\Omega}\tau_{ik}(\mathbf{x})n_k(\mathbf{x})G_{ij}(\mathbf{x},\mathbf{x}_0)\,dA(\mathbf{x})-\frac{1}{8\pi}\int_{\partial\Omega}v_i(\mathbf{x})T_{ijk}(\mathbf{x},\mathbf{x}_0)n_k\,dA(\mathbf{x})=0\end{aligned} \qquad \text{(B-4)}$$

where the singular source point is located outside the fluid domain, $\mathbf{x}_0\notin\Omega$, the unit surface normal vector n_j points into the fluid domain, S_i represents the vector source term, v_i and τ_{ik} represent the physical velocity and stress fields, respectively. The fundamental solution (Stokeslet) and its corresponding stress field (Stresslet) are given by[13]

$$G_{ij}(\mathbf{x},\mathbf{x}_0)=\frac{\delta_{ij}}{r}+\frac{r_i r_j}{r^3},\quad T_{ijk}(\mathbf{x},\mathbf{x}_0)=-6\frac{r_i r_j r_k}{r^5} \qquad \text{(B-5)}$$

respectively, where δ_{ij} is the Kronecker delta, $\mathbf{r} = \mathbf{x}\text{-}\mathbf{x}_0$ is the position vector between the given field and source points, and $r = |\mathbf{x}\text{-}\mathbf{x}_0|$ is the distance between the field and source points.

When the source point is located inside of the flow field, $\mathbf{x}_0 \in \Omega - \partial\Omega$, the induced velocity field must satisfy the general integral equation:

$$v_j(\mathbf{x}_0) = \frac{-1}{8\pi\mu}\int_{\Omega} S_i(\mathbf{x}) G_{ij}(\mathbf{x},\mathbf{x}_0)\, dV(\mathbf{x}) \\ -\frac{1}{8\pi\mu}\int_{\partial\Omega} \tau_{ik}(\mathbf{x}) n_k(\mathbf{x}) G_{ij}(\mathbf{x},\mathbf{x}_0)\, dA(\mathbf{x}) + \frac{1}{8\pi}\int_{\partial\Omega} v_i(\mathbf{x}) T_{ijk}(\mathbf{x},\mathbf{x}_0)\, n_k\, dA(\mathbf{x}) \tag{B-6}$$

whereas if the source point is located on the sufficiently smooth boundary, $\mathbf{x}_0 \in \partial\Omega$, the double layer contribution (last term in eq B-6) has to be interpreted in the sense of Cauchy principal value because of the stronger singularity in the integral kernel T_{ijk}. For a homogeneous Stokes system, the domain integrals in eqs B-4 and B-6 vanish and both equations reduce to the formulation with the boundary integrals only. In the thesis, eqs B-4 and B-6 are the key equations used for deriving solutions for the low-Reynolds number fluid flow in two coupled domains (inside and outside of the cell) which are linked by the moving boundary of the deforming membrane. It should be emphasized that many complex transport problems can be solved by the general solution procedure for Stokes flow even with the nonlinear sources and nonlinear boundary conditions.

APPENDIX C

In terms of the Green's function expressed in the Cartesian coordinates, the transformation matrices are given by[13]

$$M_{\alpha\beta} = \sigma \int_0^{2\pi} \begin{bmatrix} G_{xx} & G_{yx}\cos\phi + G_{zx}\sin\phi \\ G_{xy} & G_{yy}\cos\phi + G_{zy}\sin\phi \end{bmatrix} d\phi ,$$

$$Q_{x\alpha\beta} = \sigma \int_0^{2\pi} \begin{bmatrix} T_{xxx} & T_{yxx}\cos\phi + T_{zxx}\sin\phi \\ T_{xxy}\cos\phi + T_{xxz}\sin\phi & T_{yxy}\cos^2\phi + T_{zxz}\sin^2\phi + 2T_{yxz}\cos\phi\sin\phi \end{bmatrix} d\phi ,$$

$$Q_{\sigma\alpha\beta} = \sigma \int_0^{2\pi} \begin{bmatrix} T_{xyx} & T_{yyx}\cos\phi + T_{zyx}\sin\phi \\ T_{xyy}\cos\phi + T_{xyz}\sin\phi & T_{yyy}\cos^2\phi + T_{zyz}\sin^2\phi + 2T_{yyz}\cos\phi\sin\phi \end{bmatrix} d\phi$$

After simplifications, the elements of the transformation matrices are given by

$$M_{xx} = \sigma\left(I_{10} + \hat{x}^2 I_{30}\right), \quad M_{x\sigma} = \hat{x}\sigma\left(\sigma I_{30} - \sigma_0 I_{31}\right),$$

$$M_{\sigma x} = \hat{x}\sigma\left(\sigma I_{31} - \sigma_0 I_{30}\right), \quad M_{\sigma\sigma} = \sigma\left[I_{11} + \left(\sigma^2 + \sigma_0^2\right)I_{31} - \sigma\sigma_0\left(I_{30} + I_{32}\right)\right],$$

$$Q_{xxx} = -6\hat{x}^3\sigma I_{50},$$

$$Q_{xx\sigma} = -6\hat{x}^2\sigma\left(\sigma I_{50} - \sigma_0 I_{51}\right),$$

$$Q_{x\sigma x} = Q_{xx\sigma},$$

$$Q_{x\sigma\sigma} = -6\hat{x}\sigma\left(\sigma^2 I_{50} + \sigma_0^2 I_{52} - 2\sigma\sigma_0 I_{51}\right),$$

$$Q_{\sigma xx} = -6\hat{x}^2\sigma\left(\sigma I_{51} - \sigma_0 I_{50}\right),$$

$$Q_{\sigma\sigma x} = Q_{\sigma x\sigma},$$

$$Q_{\sigma x\sigma} = -6\hat{x}\sigma\left[\left(\sigma^2 + \sigma_0^2\right)I_{51} - \sigma\sigma_0\left(I_{50} + I_{52}\right)\right],$$

$$Q_{\sigma\sigma\sigma} = -6\sigma\left[\sigma^3 I_{51} - \sigma^2\sigma_0\left(I_{50} + 2I_{52}\right) + \sigma\sigma_0^2\left(I_{53} + 2I_{51}\right) - \sigma_0^3 I_{52}\right]$$

The general expression for I_{mn} is given by,[13]

$$I_{mn} = \frac{4k^m}{(4\sigma\sigma_0)^{m/2}} \int_0^{\pi/2} \frac{(2\sin^2(\theta)-1)^n}{[1-k^2\sin^2(\theta)]^{m/2}} d\theta$$

where $k = \sqrt{4\sigma\sigma_0 / (\hat{x}^2 + (\sigma+\sigma_0)^2)}$, $\hat{x} = x - x_0$, and the field and source point locations are $\mathbf{x} = (x, \sigma)$ and $\mathbf{x}_0 = (x_0, \sigma_0)$, respectively. The general form of integrals I_{mn} can be expressed in terms of complete elliptic integrals:[67]

$$I_{10} = \frac{2k}{(\sigma\sigma_0)^{1/2}} F, \qquad I_{11} = \frac{2}{(\sigma\sigma_0)^{1/2} k} [(2-k^2)F - 2E],$$

$$I_{30} = \frac{k^3 E}{2(\sigma\sigma_0)^{3/2}(1-k^2)}, \qquad I_{31} = \frac{k}{(\sigma\sigma_0)^{3/2}} \left[\frac{2-k^2}{2(1-k^2)} E - F \right],$$

$$I_{32} = \frac{1}{(\sigma\sigma_0)^{3/2} k} \left[\frac{k^4 - 8k^2 + 8}{2(1-k^2)} E + (2k^2 - 4)F \right],$$

$$I_{50} = \frac{k^5}{24(\sigma\sigma_0)^{5/2}(1-k^2)} \left[\frac{2(2-k^2)}{1-k^2} E - F \right],$$

$$I_{51} = \frac{k^3}{24(\sigma\sigma_0)^{5/2}(1-k^2)} \left[\frac{2(k^4 - k^2 + 1)}{1-k^2} E + (k^2 - 2)F \right],$$

$$I_{52} = \frac{k}{24(\sigma\sigma_0)^{5/2}(1-k^2)} \left[\frac{2(-k^6 + 6k^2 - 4)}{1-k^2} E - (k^4 + 8k^2 - 8)F \right],$$

$$I_{53} = \frac{1}{24(\sigma\sigma_0)^{5/2}(1-k^2)k} \left[\frac{2(k^8 + k^6 - 33k^4 + 64k^2 - 32)}{1-k^2} E + (k^6 + 30k^4 - 96k^2 + 64)F \right]$$

The complete elliptic integrals of the first and second kind and the modulus are defined by, respectively,

$$F(k) = \int_0^{\pi/2} \frac{d\theta}{\sqrt{1-k^2\sin^2\theta}}, \quad E(k) = \int_0^{\pi/2} \sqrt{1-k^2\sin^2\theta}\, d\theta, \quad k = \sqrt{\frac{4\sigma\sigma_0}{\hat{x}^2 + (\sigma+\sigma_0)^2}}$$

APPENDIX D

The tangential derivatives of the transformation matrices $M_{\alpha\beta}$ and $Q_{\alpha\beta\gamma}$ are computed as follows:

$$\frac{\partial M_{\alpha\beta}}{\partial s} = \mathbf{t}_s \cdot \nabla M_{\alpha\beta}, \quad \frac{\partial Q_{\alpha\beta\gamma}}{\partial s} = \mathbf{t}_s \cdot \nabla Q_{\alpha\beta\gamma}$$

where

$$\frac{\partial M_{xx}}{\partial x_0} = \sigma\hat{x} I_{30} + 3\sigma\hat{x}^3 I_{50} - 2\sigma\hat{x} I_{30} \ ,$$

$$\frac{\partial M_{xx}}{\partial \sigma_0} = \sigma^2 I_{31} - \sigma\sigma_0 I_{30} + 3\sigma^2\hat{x}^2 I_{51} - 3\sigma\sigma_0\hat{x}^2 I_{50} \ ,$$

$$\frac{\partial M_{x\sigma}}{\partial x_0} = \sigma\sigma_0 I_{31} - 3\sigma\sigma_0\hat{x}^2 I_{51} - \sigma^2 I_{30} + 3\sigma^2\hat{x}^2 I_{50},$$

$$\frac{\partial M_{x\sigma}}{\partial \sigma_0} = -\sigma\hat{x} I_{31} + 3\sigma\sigma_0^2\hat{x} I_{51} - 3\sigma^2\sigma_0\hat{x} I_{52} - 3\sigma^2\sigma_0\hat{x} I_{50} + 3\sigma^3\hat{x} I_{51} \ ,$$

$$\frac{\partial M_{\sigma x}}{\partial x_0} = -\sigma^2 I_{31} + \sigma\sigma_0 I_{30} + 3\sigma^2\hat{x}^2 I_{51} - 3\sigma\sigma_0\hat{x}^2 I_{50},$$

$$\frac{\partial M_{\sigma x}}{\partial \sigma_0} = -\sigma\hat{x} I_{30} - 3\sigma^2\sigma_0\hat{x} I_{51} + 3\sigma\sigma_0^2\hat{x} I_{50} + 3\sigma^3\hat{x} I_{52} - 3\sigma^2\sigma_0\hat{x} I_{51} \ ,$$

$$\frac{\partial M_{\sigma\sigma}}{\partial x_0} = \sigma\hat{x} I_{31} + 3\sigma\sigma_0^2\hat{x} I_{51} + 3\sigma^3\hat{x} I_{51} - 3\sigma^2\sigma_0\hat{x} I_{50} - 3\sigma^2\sigma_0\hat{x} I_{52},$$

$$\frac{\partial M_{\sigma\sigma}}{\partial \sigma_0} = \sigma\sigma_0 I_{31} - \sigma^2 I_{30} + 3\sigma^2\sigma_0^2 I_{50} + 6\sigma^2\sigma_0^2 I_{52} - 3\sigma\sigma_0^3 I_{51} - 6\sigma^3\sigma_0 I_{51} - 3\sigma^3\sigma_0 I_{53} + 3\sigma^4 I_{52} \ ,$$

$$\frac{\partial Q_{xxx}}{\partial x_0} = 18\sigma\hat{x}^2 I_{50} - 30\sigma\hat{x}^4 I_{70} \ ,$$

$$\frac{\partial Q_{xxx}}{\partial \sigma_0} = 30\sigma\sigma_0\hat{x}^3 I_{70} - 30\sigma^2\hat{x}^3 I_{71} \ ,$$

$$\frac{\partial Q_{xx\sigma}}{\partial x_0} = 12\sigma^2\hat{x}I_{50} - 30\sigma^2\hat{x}^3I_{70} - 12\sigma\sigma_0\hat{x}I_{51} + 30\sigma\sigma_0\hat{x}^3I_{71},$$

$$\frac{\partial Q_{xx\sigma}}{\partial \sigma_0} = 30\sigma^2\sigma_0\hat{x}^2I_{70} - 30\sigma^3\hat{x}^2I_{71} + 6\sigma\hat{x}^2I_{51} - 30\sigma\sigma_0^2\hat{x}^2I_{71} + 30\sigma^2\sigma_0\hat{x}^2I_{72},$$

$$\frac{\partial Q_{x\sigma x}}{\partial x_0} = \frac{\partial Q_{xx\sigma}}{\partial x_0}, \quad \frac{\partial Q_{x\sigma x}}{\partial \sigma_0} = \frac{\partial Q_{xx\sigma}}{\partial \sigma_0},$$

$$\frac{\partial Q_{x\sigma\sigma}}{\partial x_0} = 6\sigma^3I_{50} - 30\sigma^3\hat{x}^2I_{70} - 12\sigma^2\sigma_0I_{51} + 60\sigma^2\sigma_0\hat{x}^2I_{71} + 6\sigma\sigma_0^2I_{52} - 30\sigma\sigma_0^2\hat{x}^2I_{72},$$

$$\begin{aligned}\frac{\partial Q_{x\sigma\sigma}}{\partial \sigma_0} &= 30\sigma^3\sigma_0\hat{x}I_{70} - 30\sigma^4\hat{x}I_{71} + 12\sigma^2\hat{x}I_{51} - 60\sigma^2\sigma_0^2\hat{x}I_{71} \\ &\quad + 60\sigma^3\sigma_0\hat{x}I_{72} - 12\sigma\sigma_0\hat{x}I_{52} + 30\sigma\sigma_0^3\hat{x}I_{72} - 30\sigma^2\sigma_0^2\hat{x}I_{73},\end{aligned}$$

$$\frac{\partial Q_{\sigma xx}}{\partial x_0} = 12\sigma^2\hat{x}I_{51} - 30\sigma^2\hat{x}^3I_{71} - 12\sigma\sigma_0\hat{x}I_{50} + 30\sigma\sigma_0\hat{x}^3I_{70},$$

$$\frac{\partial Q_{\sigma xx}}{\partial \sigma_0} = 30\sigma^2\sigma_0\hat{x}I_{71} - 30\sigma^3\hat{x}^2I_{72} + 6\sigma\hat{x}^2I_{50} - 30\sigma\sigma_0^2\hat{x}^2I_{70} + 30\sigma^2\sigma_0\hat{x}^2I_{71},$$

$$\begin{aligned}\frac{\partial Q_{\sigma x\sigma}}{\partial x_0} &= 6\sigma\sigma_0^2I_{51} + 6\sigma^3I_{51} - 30\sigma\sigma_0^2\hat{x}^2I_{71} - 30\sigma^3\hat{x}^2I_{71} \\ &\quad - 6\sigma^2\sigma_0I_{50} - 6\sigma^2\sigma_0I_{52} + 30\sigma^2\sigma_0\hat{x}^2I_{70} + 30\sigma^2\sigma_0\hat{x}^2I_{72},\end{aligned}$$

$$\begin{aligned}\frac{\partial Q_{\sigma x\sigma}}{\partial \sigma_0} &= 60\sigma^3\sigma_0\hat{x}I_{71} - 30\sigma^4\hat{x}I_{72} + 6\sigma^2\hat{x}I_{50} - 30\sigma^2\sigma_0^2\hat{x}I_{70} \\ &\quad + 6\sigma^2\hat{x}I_{52} - 60\sigma^2\sigma_0^2\hat{x}I_{72} + 30\sigma^3\sigma_0\hat{x}I_{73} - 12\sigma\sigma_0\hat{x}I_{51} + 30\sigma\sigma_0^3\hat{x}I_{71},\end{aligned}$$

$$\frac{\partial Q_{\sigma\sigma x}}{\partial x_0} = \frac{\partial Q_{\sigma x\sigma}}{\partial x_0}, \quad \frac{\partial Q_{\sigma\sigma x}}{\partial \sigma_0} = \frac{\partial Q_{\sigma x\sigma}}{\partial \sigma_0},$$

$$\frac{\partial Q_{\sigma\sigma\sigma}}{\partial x_0} = -30\sigma^2\sigma_0^2\hat{x}I_{73} + 60\sigma^3\sigma_0\hat{x}I_{72} + 30\sigma\sigma_0^3\hat{x}I_{72} - 30\sigma^4\hat{x}I_{71} + 30\sigma^3\sigma_0\hat{x}I_{70} - 60\sigma^2\sigma_0^2\hat{x}I_{71},$$

$$\begin{aligned}\frac{\partial Q_{\sigma\sigma\sigma}}{\partial \sigma_0} &= -12\sigma^2\sigma_0I_{53} + \left(12\sigma^3 + 18\sigma\sigma_0^2\right)I_{52} + 6\sigma^3I_{50} - 24\sigma^2\sigma_0I_{51} - 30\sigma^3\sigma_0^2I_{74} \\ &\quad + \left(60\sigma^4\sigma_0 + 60\sigma^2\sigma_0^3\right)I_{73} - \left(30\sigma\sigma_0^4 + 30\sigma^5 + 120\sigma^3\sigma_0^2\right)I_{72} + \left(60\sigma^4\sigma_0 + 60\sigma^2\sigma_0^3\right)I_{71} - 30\sigma^3\sigma_0^2I_{70}\end{aligned}$$

The lower order terms, I_{10}, I_{11}, I_{30}, I_{31}, I_{32}, I_{50}, I_{51}, I_{52}, and I_{53} are listed in Appendix C in terms of complete elliptic integrals of first kind F and second kind E with the modulus k, and therefore are not repeated here. The remaining higher order terms are:

$$I_{70}=\frac{k^7}{480(\sigma\sigma_0)^{7/2}\left(1-k^2\right)^2}\left(\frac{8k^4-23k^2+23}{1-k^2}E+4\left(k^2-2\right)F\right),$$

$$I_{71}=\frac{2-k^2}{k^2}I_{70}-\frac{1}{2\sigma\sigma_0}I_{50},$$

$$I_{72}=\frac{k^4-4k^2+4}{k^4}I_{70}+\frac{4k^2-8}{(4\sigma\sigma_0)k^2}I_{50}+\frac{4}{(4\sigma\sigma_0)^2}I_{30},$$

$$I_{73}=\frac{-8}{(4\sigma\sigma_0)^3}I_{10}+\frac{-12k^2+24}{(4\sigma\sigma_0)^2k^2}I_{30}+\frac{-6k^4+24k^2-24}{(4\sigma\sigma_0)k^4}I_{50}+\frac{-k^6+6k^4-12k^2+8}{k^6}I_{70},$$

$$I_{74}=\frac{64}{(4\sigma\sigma_0)^{7/2}k}E+\frac{k^8-8k^6+24k^4-32k^2+16}{k^8}I_{70}+\frac{8k^6-48k^4+96k^2-64}{(4\sigma\sigma_0)k^6}I_{50}$$
$$+\frac{24k^4-96k^2+96}{(4\sigma\sigma_0)^2k^4}I_{30}+\frac{32k^2-64}{(4\sigma\sigma_0)^3k^2}I_{10}$$

APPENDIX E

The ring-source-type Green's function M_L and its normal gradient Q_L for the Laplace operator are calculated by azimuthal integration of the three-dimensional forms,

$$M_L = \sigma \int_0^{2\pi} G_L \, d\theta = \frac{\sigma}{4\pi} I_{10},$$

$$Q_L = \sigma \int_0^{2\pi} \frac{\partial G_L}{\partial n} d\theta = -\frac{\sigma \hat{x}}{4\pi} I_{30} n_x + \left(\frac{\sigma \sigma_0}{4\pi} I_{31} - \frac{\sigma^2}{4\pi} I_{30} \right) n_\sigma$$

Similarly, the axisymmetric interpolation functions $\bar{\phi}_{mk}$, the gradient of the interpolation functions $\nabla \bar{\phi}_{mk}$, the particular solutions $\bar{f}_{mk}$, and their normal gradient $\partial \bar{f}_{mk} / \partial n$ can be derived,

$$\bar{\phi}_{mk} = \int_0^{2\pi} (1 + r_{mk}) d\theta = 2\pi + \frac{8\sqrt{\sigma_m \sigma_k}}{p} E,$$

$$\nabla \bar{\phi}_{mk} = \hat{x}_{mk} I_{10} \hat{e}_x + (\sigma_m I_{10} - \sigma_k I_{11}) \hat{e}_\sigma,$$

$$\bar{f}_{mk} = \int_0^{2\pi} \left(\frac{r_{mk}^2}{6} + \frac{r_{mk}^3}{12} \right) d\theta = \frac{2\sigma_m \sigma_k \pi}{3p^2} (2 - p^2) + \frac{8(\sigma_m \sigma_k)^{3/2}}{9p^3} \left[(4 - 2p^2) E + (p^2 - 1) F \right],$$

$$\frac{\partial \bar{f}_{mk}}{\partial n} = \int_0^{2\pi} \nabla f_{mk} \cdot \mathbf{n} \, d\theta = \frac{2\pi}{3} (\hat{x}_{mk} n_x + \sigma_m n_\sigma)$$
$$+ \frac{2\sqrt{\sigma_m \sigma_k}}{p} \left\{ \hat{x}_{mk} E n_x + \left(\sigma_m + \sigma_k - \frac{2\sigma_k (2p^2 - 1)}{3p^2} \right) E n_\sigma + \frac{2\sigma_k (p^2 - 1)}{3p^2} F n_\sigma \right\}$$

where $p = \sqrt{4\sigma_m \sigma_k / \left(\hat{x}_{mk}^{\,2} + (\sigma_m + \sigma_k)^2 \right)}$, $\mathbf{x}_m = (x_m, \sigma_m)$, $\mathbf{x}_k = (x_k, \sigma_k)$, and $\hat{x}_{mk} = x_m - x_k$.

At a singular point, $\mathbf{x}_m = \mathbf{x}_k$, the above expressions can be further reduced to become

$$\bar{\phi}_{mk} = 2\pi + 8\sigma_k, \quad \bar{f}_{mk} = \frac{2\pi}{3} \sigma_k^2 + \frac{16}{9} \sigma_k^3, \quad \frac{\partial \bar{f}_k}{\partial n} = \frac{2\sigma_k n_\sigma}{3} (\pi + 4\sigma_k)$$

whereas $\nabla \bar{\phi}_k$ remains unchanged.

APPENDIX F

Let the matrix be defined by

$$S_{ik} = -\omega \bar{f}_{ik} + \int_{\partial\Omega_j} \left(M_L \frac{\partial \bar{f}_{jk}}{\partial n} - \bar{f}_{jk} Q_L \right) d\ell$$

Then, the consolidation of the intermediate terms yields

$$A_{im} = \sum_{k=1}^{N+L} S_{ik} \left(\bar{\phi}\right)^{-1}_{km},$$

$$B_{ip} = \sum_{\ell=1}^{N+L} \left\{ \sum_{m=1}^{N+L} A_{im} \left(\mathbf{V} \cdot \nabla \bar{\phi}\right)_{mn} \right\} \left(\bar{\phi}\right)^{-1}_{np}$$

A fully implicit form of the integral convection-diffusion equation can be written as

$$\omega_i C_i^{n+1} - \sum_{j=1}^{N} \left(\int_{\partial\Omega_j} M_{L,ij}\, d\ell \right) \left(\frac{\partial C}{\partial n} \right)_j^{n+1} + \sum_{j=1}^{N} \left\{ \left(\int_{\partial\Omega_j} Q_{L,ij}\, d\ell \right) + \left(\frac{A_{ij}}{\Delta t} + B_{ij} + A_{ij} g_j \right) \right\} C_j^{n+1}$$
$$+ \sum_{j=N+1}^{N+L} \left(\frac{A_{ij}}{\Delta t} + B_{ij} + A_{ij} g_j \right) C_j^{n+1} = \frac{1}{\Delta t} \sum_{j=1}^{N+L} A_{ij}\, C_j^n$$

where i, j, n and Δt denote the source point, field point, index of time step, and the magnitude of the time step, respectively; $g_j = \left(\nabla \cdot \partial \mathbf{u} / \partial t\right)_j$ is the quasi sink term due to the matrix dilution; N is the total number of boundary elements, and L is the total number of internal nodes. In the above equations, the terms that include $1/\Delta t$ should be omitted for the steady state system, the advection terms that include B_{ij} should be removed for a purely diffusion system, and g_j should be removed for a homogeneous system. The constant coefficients or dimensionless groups can be multiplied to the matrices A and B according to the corresponding differential equations.

REFERENCES

[1] Fan, T.-H. and Fedorov, A. G., 2003, Analysis of hydrodynamic interactions during AFM imaging of biological membranes, *Langmuir,* **19**, pp. 1347-1356.

[2] Fan, T.-H. and Fedorov, A. G., 2003, Electrohydrodynamics and surface force analysis in AFM imaging of a charged, deformable biological membrane in a dilute electrolyte solution, *Langmuir,* in press.

[3] Fan, T.-H. and Fedorov, A. G., 2003, An integrated transport model for tracking an exocytotic event dynamics using a microelectrode, *Biophys. J.*, in preparation.

[4] Morris, V. J., Kirby, A. R., and Gunning, A. P., 1999, *Atomic Force Microscopy for Biologists*, Imperial College Press, London.

[5] Lee, I. and Marchant, R. E., 2000, Force measurement on platelet surfaces with high spatial resolution under physiological conditions, *Colloids Surf. B*, **19**, 357-365.

[6] Domke, J., Dannöhl, S., Parak, W.J., Müller, O., Aicher, W. K., and Radmacher, M., 2000, Substrate dependent differences in morphology and elasticity of living osteoblasts investigated by atomic force microscopy, *Colloids Surf. B*, **19**, 367-379.

[7] Dufrêne, Y. F., Boonaert, C. J. P., van der Mei, H. C., Busscher, H. J., and Rouxhet, P. G., 2001, Probing molecular interactions and mechanical properties of microbial cell surfaces by atomic force microscopy, *Ultramicroscopy*, **86**, 113-120.

[8] Domke, J., Parak, W. J., George, M., Gaub, H. E., and Radmacher, M., 1999, Mapping the mechanical pulse of single cardiomyocytes with the atomic force microscope, *Eur Biophys J.*, **28**, 179-186.

[9] Parak, W. J., Domke, J., George, M., Kardinal, A., Radmacher, M., Gaub, H. E., de Roos, A. D. G., Theuvenet, A. P. R., Wiegand, G., Sackmann, E., and Behrends, J. C., 1999, Electrically excitable normal rat kidney fibroblasts: a new model system for cell-semiconductor hybrids, *Biophys J.,* **76**, 1659-1667.

[10] Hertz, H., 1881, *J. Reine Angrew Math.*, **92**, 156-171.

[11] Helfrich, W., 1973, *Z. Naturforsch. Teil C*, **28**, 693.

[12] Zhong-can, O.-Y. and Helfrich, W., 1989, Bending energy of vesicle membranes: general expressions for the first, second, and third variation of the shape energy and applications to spheres and cylinders, *Phys. Rev. A*, **39**, 5280-5288.

[13] Pozrikidis, C., 1992, Boundary integral and singularity methods for linearized viscous flow, *Cambridge University Press*, Cambridge.

[14] Kranz, C., Friedbacher, G., Mizaikoff, B., Lugstein, A., Smoliner, J., and Bertagnolli, E., 2001, Integrating an ultramicroelectrode in an AFM cantilever: combined technology for enhanced information, *Anal. Chem.*, **73**, 2491-2500.

[15] Alberts, B. et al., 1994, *Molecular Biology of the Cell*, Garland Pub., New York.

[16] Israelachvili, J. N., 1998, *Intermolecular and Surface Forces,* Academic Press, San Diego, CA.

[17] Lorentz, H. A., 1907, Ein allgemeiner Satz, die bewegung einer reibenden Flüssigkeit betreffend, nebst einigen anwendungen Desselben, *Abh. Theor. Phys.,* **1**, 23-42.

[18] Odqvist, F. K. G., 1930, Uber die Randwertaufgaben der Hydrodynamik zaher Flussigkeiten, *Math. Z.*, **32**, 329-375.

[19] Ladyzhenskaya, O. A., 1969, *The Mathematical Theory of Viscous Incompressible Flow*, Gordon & Breach, New York.

[20] Rallison, J. M. and Acrivos, A., 1978, A numerical study of the deformation and burst of a viscous drop in an extensional flow, *J. Fluid Mech.*, **89**, 191-200.

[21] Lee, S. H. and Leal, L. G., 1982, The motion of a sphere in the presence of a deformable interface, *J. Colloid Interface Sci.*, **87**, 81-106.

[22] Pozrikidis, C., 1990, The instability of a moving viscous drop, *J. Fluid Mech.*, **210**, 1-21.

[23] Evans, E. A. and Skalak, R., 1980, *Mechanics and Thermodynamics of Biomembranes,* CRC Press, Boca Raton, FL.

[24] Landau, L. D. and Lifshitz, E. M., 1959, *Fluid Mechanics*, Pergamon Press, London.

[25] Scriven, L. E., 1960, Dynamics of a fluid interface, *Chem. Eng. Science*, **12**, 98-108.

[26] Deuling, H. J. and Helfrich, W., 1976, *J. Phys. (Paris)*, **37**, 1335.

[27] Zhong-can, O.-Y. and Helfrich, W., 1987, Instability and deformation of a spherical vesicle by pressure, *Phys. Rev. Lett.,* **59**, 2486-2488.

[28] Zhong-can, O.-Y., 2001, Elastic theory of biomembranes, *Thin Solid Films*, **393**, 19-23.

[29] Döbereiner, H. G., 2000, Properties of giant vesicles, *Curr. Opin. Colloid Interface Sci.,* **5**, 256-263.

[30] Pozrikidis, C., 1990, The axisymmetric deformation of a red blood cell in uniaxial straining Stokes flow, *J. Fluid Mech.*, **216**, 231-254.

[31] Press, W. H., Teukolsky, S. A., Vetterling, W. T., and Flannery, B. P., 1988, *Numerical Recipes in C: The Art of Scientific Computing,* Cambridge University Press, New York.

[32] Evans, E. and Rawicz, W., 1990, Entropy-driven tension and bending elasticity in condensed-fluid membranes, *Phys. Rev. Lett.*, **64**, 2094-2097.

[33] Evans, E. and Rawicz, W., 1997, Elasticity of "fuzzy" biomembranes, *Phys. Rev. Lett.*, **79**, 2379-2382.

[34] Scheffer, L., Bitler, A., Ben-Jacob, E., and Korenstein, R. 2001, Atomic force pulling: probing the local elasticity of the cell membrane, *Eur Biophys J.*, **30**, 83-90.

[35] Döbereiner, H.-G., Evans, E., Kraus, M., Seifert, U., and Wortis, M., 1997, Mapping vesicle shapes into the phase diagram: a comparison of experiment and theory, *Phys. Rev. E*, **55**, 4458-4474.

[36] Deuling, H. J. and Helfrich, W., 1976, Red blood cell shapes as explained on the basis of curvature elasticity, *Biophys. J.*, **16**, 861-868.

[37] Binnig, G., Quate, C. F., and Gerber, C., 1986, Atomic Force Microscope, *Phys. Rev. Lett.*, **56**, 930-933.

[38] Hansma, P. K., Elings, V. B., Marti, O., and Bracker, C. E., 1988, Scanning tunneling microscopy and atomic force microscopy: application to biology and technology, *Science,* **242**, 209-216.

[39] Lal, R. and John, S. A., 1994, Biological application of atomic force microscopy, *Am. J. Physiol.*, **266**, C1-C21.

[40] Heinz, W. F. and Hoh, J. H., 1999, Spatially resolved force spectroscopy of biological surfaces using the atomic force microscope, *Trends in BioNanotechnology*, **17**, 143-150.

[41] Kamm, R. D., 2002, Cellular fluid mechanics, *Annu. Rev. Fluid Mech.*, **34**, 211-232.

[42] McElfresh, M., Baesu, E., Balhorn, R., Belak, J., Allen, M. J., and Rudd, R. E., 2002, Combining constitutive materials modeling with atomic force microscopy to understand the mechanical properties of living cells, *Proc. Natl. Acad. Sci. USA*, **99**, 6493-6497.

[43] Sader, J. E., 1998, Frequency response of cantilever beams immersed in viscous fluids with applications to the atomic force microscopy, *J. Appl. Phys.*, **84**, 64-76.

[44] Rajagopalan, R., 2000, Atomic force and optical force microscopy: applications to interfacial microhydrodynamics, *Colloids & Surf A: Physicochem. Eng. Aspects,* **174**, 253-267.

[45] Ma, H., Jimenez, J., and Rajagopalan, R., 2000, Brownian fluctuation spectroscopy using atomic force microscopes, *Langmuir*, **16**, 2254-2261.

[46] Mitchell, D. J. and Ninham, B. W., 1989, Curvature elasticity of charged membranes, *Langmuir*, **5**, 1121-1123.

[47] Winterhalter, M. and Helfrich, W., 1992, Bending elasticity of electrically charged bilayers: coupled monolayers, neutral surfaces, and balancing stresses, *J. Phys. Chem.*, **96**, 327-330.

[48] Chou, T., Jarić, M. V., and Siggia, E.D., 1997, Electrostatics of lipid bilayer bending, *Biophys. J.*, **72**, 2042-2055.

[49] Tao, N. J., Lindsay, S. M., and Lees, S., 1992, Measuring the microelastic properties of biological material, *Biophys. J.*, **63**, 1165-1169.

[50] Radmacher, M., Tillmann, R. W., Fritz, M., and Gaub, H. E., 1992, From molecules to cells: imaging soft samples with the atomic force microscope, *Science*, **257**, 1900-1905.

[51] Velegol, S. B. and Logan, B. E., 2002, Contributions of bacterial surface polymers, electrostatics, and cell elasticity to the shape of AFM force curves, *Langmuir*, **18**, 5256-5262.

[52] Butt, H.-J., 1991, Electrostatic interaction in atomic force microscopy, *Biophys. J.*, **60**, 777-785.

[53] Butt, H.-J., 1991, Measuring electrostatic, van der Waals, and hydration forces in electrolyte solutions with an atomic force microscope, *Biophys. J.*, **60**, 1438-1444.

[54] Butt, H.-J., 1992, Electrostatic interaction in scanning probe microscopy when imaging in electrolyte solutions, *Nanotechnology*, **3**, 60-68.

[55] Grant, M. L. and Saville, D. A., 1995, Electrostatic interactions between a nonuniformly charged sphere and a charged surface, *J. Colloid Interface Sci.*, **171**, 35-45.

[56] Dungan, S. R. and Hatton, T. A., 1994, Electrostatic interactions between a charged sphere and an oppositely charged, deformable interface, *J. Colloid Interface Sci.*, **164**, 200-214.

[57] Bonaccurso, E., Kappl, M., and Butt, H.-J., 2002, Hydrodynamic force measurements: boundary slip of water on hydrophilic surfaces and electrokinetic effects, *Phys. Rev. Lett.*, **88**, 076103.

[58] Vinogradova, O. I. and Yakubov, G. E., 2003, Dynamic effects on force measurements. 2. Lubrication and the atomic force microscope, *Langmuir*, **19**, 1227-1234.

[59] Macpherson, J. V., Unwin, P. R., 2000, Combined scanning electrochemical-atomic force microscopy, *Anal. Chem.*, **72**, 276-285.

[60] Inoue, I., Kobatake, Y., and Tasaki, I., 1973, Excitability, instability and phase transitions in squid axon membrane under internal perfusion with dilute salt solutions, *Biochimica et Biophysica Acta (BBA) – Biomembranes*, **307**, 471-477.

[61] Inoue, I., Ishida, N., and Kobatake, Y., 1973, Studies of excitable membrane formed on the surface of protoplasmic drops isolated from Nitella. IV. Excitability of the drop membrane in various compositions of the external salt solution, *Biochimica et Biophysica Acta (BBA) – Biomembranes*, **330**, 27-38.

[62] Russel, W. B., Saville, D. A., and Schowalter, W.R., 1989, *Colloidal Dispersions*, Cambridge University Press, Cambridge.

[63] Bromberg, J. P., 1984, *Physical Chemistry*, Allyn and Bacon Inc., Boston.

[64] Melcher, J. R. and Taylor, G. I., 1969, Electrohydrodynamics: a review of the role of interfacial shear stresses, *Annu. Rev. Fluid Mech.*, **1**, 111-146.

[65] Peitzsch, R. M., Eisenberg, M., Sharp, K. A., and Mclaughlin, S., 1995, Calculation of the electrostatic potential adjacent to model phospholipid bilayers, *Biophys. J.*, **68**, 729-738.

[66] Brebbia, C. A., Telles, J. C. F., and Wrobel L. C., 1984, *Boundary Element Techniques*, Springer-Verlag, New York.

[67] Gradshteyn, I. S. and Ryshik, I. M., 1980, *Table of Integrals, Series, and Products*, Academic Press.

[68] Marszalek, P. E., Farrell, B., Verdugo, P., and Fernandez, J. M., 1997, Kinetics of release of serotonin from isolated secretory granules. II. Ion exchange determines the diffusivity of serotonin, *Biophysical Journal*, **73**, 1169-1183.

[69] Kennedy, R. T., Huang, L., Atkinson, M. A., and Dush, P., 1993, Amperometric monitoring of chemical secretions from individual pancreatic β-cells, *Anal. Chem.*, **65**, 1882-1887.

[70] Helfferich, F., 1995, *Ion exchange*, Dover Publications, New York.

[71] Qian, W.-J., Aspinwall, C. A., Battiste, M. A., and Kennedy, R. T., 2000, Detection of secretion from single pancreatic β-cells using extracellular fluorogenic reactions and confocal fluorescence microscopy, *Anal. Chem.*, **72**, 711-717.

[72] Qian, W.-J., Kennedy, R. T., 2001, Spatial oranization of Ca2+ entry and exocytosis in mouse pancratic β-cells, *Biochem. Biophys. Res. Comm*, **286**, 315-321.

[73] Lee, C, Kwak, J., and Bard, A. J., 1990, Application of scanning electrochemical microscopy to biology samples, *Proc. Natl. Acad. Sci.*, **87**, 1740-1743.

[74] Unwin, P. R., 1998, The marlow medal lecture: Dynamic electrochemistry as a quantitative probe of interfacial physicochemical processes, *Journal of Chemical Society, Faraday Transactions*, **9**, 3183-3195.

[75] Yasukawa, T., Kaya, T., and Matsue, T., 2000, Characterization and imaging of single cells with scanning electrochemical microscopy, *Electroanalysis*, **12**, 653-659.

[76] Travis, E. R. and Wightman R. M., 1998, Spatio-temporal resolution of exocytosis from individual cells, *Annu. Rev. Biophys. Biomol. Struct.*, **27**, 77-103.

[77] Troyer, K. P., Heien, M. L. A. V., Venton, B. J., and Wightman R. M., 2002, Neurochemistry and electroanalytical probes, *Current Opinion in Chemical Biology*, **6**, 696-703.

[78] Jackson, B. P., Dietz, S. M., and Wightman, R. M., 1995, Fast-scan cyclic voltammetry of 5-hydroxytryptamine, *Anal. Chem.*, **67**, 1115-1120.

[79] Cahill, P. S., Walker, Q. D., Finnegan, J. M., Mickelson, G. E., Travis, E. R., and Wightman, R. M., 1996, Microelectrodes for the measurement of catecholamines in biological systems, *Anal. Chem.*, **68**, 3180-3186.

[80] Peters, J. L. and Michael, A. C., 2000, Change in the kinetics of dopamine release and uptake have differential effects on the spatial distribution of extracellular dopamine concentration in rat striatum, *J. Neurochem.*, **74**, 1563-1573.

[81] Pantano, P., Morton, T. H., and Kuhr, W. G., 1991, Enzyme-modified carbon-fiber microelectrodes with millisecond response times, *J. Am. Chem. Soc.*, **113**, 1832-1833.

[82] Meyerhoff, J. B., Ewing, M. A., and Ewing, A. G., 1999, Ultrasmall enzyme electrodes with response time less than 100 milliseconds, *Electroanalysis*, **11**, 308-312.

[83] Huang, L., Shen, H., Atkinson, M. A., and Kennedy, R. T., 1995, Detection of exocytosis at individual pancreatic β cells by amperometry at a chemically modified microelectrode, *Proc. Natl. Acad. Sci. USA*, **92**, 9608-9612.

[84] Schroeder, T. J., Jankowski, J. A., Kawagoe, K. T., Wightman, R. M., Lefrou, C., and Amatore, C., 1992, Analysis of diffusional brodening of vesicular packets of catecholamines released from biological cells during exocytosis, *Anal. Chem.*, **64**, 3077-3083.

[85] Alvarez de Toledo, G., Fernandez-Chacon, R., and Fernandez, J.M., 1993, Release of secretory products during transient vesicle fusion, *Nature*, **363**, 554-557.

[86] Bruns, D. and Jahn, R., 1995, Real-time measurement of transmitter release from single synaptic vesicles, *Nature*, **377**, 62-65.

[87] Schroeder, T. J., Borges, R., Finnegan, J. M., Pihel, K., Amatore, C., and Wightman, R. M., 1996, Temporally resolved, independent stages of individual exocytotic secretion events, *Biophysical Journal*, **70**, 1061-1068.

[88] Amatore, C., Bouret, Y., and Midrier, L., 1999, Time-resolved dynamics of the vesicle membrane during individual exocytotic secretion events, as extracted from amperometric monitoring of adrenaline exocytosis from chromaffin cells, *Chem. Eur. J.*, **5**, 2151-2162.

[89] Amatore, C., Bouret Y., Travis, E. R., Wightman, R. M., 2000, Interplay between membrane dynamics, diffusion and swelling pressure governs individual vesicular exocytotic events during release of adrenaline by chromaffin cells, *Biochimie*, **82**, 481-496.

[90] Amatore, C., Arbault, S., Bonifas, I., Bouret Y., Erard M., and Guille M., 2003, Dynamics of full fusion during vesicular exocytotic events: release of adrenaline by chromaffin cells, *Chemphyschem*, **4**, 147-154.

[91] Marszalek, P. E., Farrell, B., Verdugo, P., and Fernandez, J. M., 1997, Kinetics of release of serotonin from isolated secretory granules. I. Amperometric detection of serotonin from electroporated granules, *Biophysical Journal*, **73**, 1160-1168.

[92] Stiles, J. R., Helden, D. V., Bartol, T. M., Salpeter, E. E., and Salpeter, M. M., Miniature endplate current rise times <100μs from improved dual recordings can be modeled with passive acetylcholine diffusion from a synaptic vesicle, *Proc. Natl. Acad. Sci. USA*, **93**, 5747-5752.

[93] Farrell, B. and Cox, S., 2002, Estimating the time course of pore expansion during the spike phase of exocytotic release in mast cells of the beige mouse, *Bulletin of Mathematical Biology*, **64**, 979-1010.

[94] Ciofalo, M., Collins, M. W., and Hennessy, T. R., 1996, Modelling nanoscale fluid dynamics and transport in physiological flows, *Med. Eng. Phys.*, **18**, 437-451.

[95] Nir, A., 1989, Deformation of some biological particles, *Phys. Fluids A*, **1**, 101-107.

[96] Pincus, P., 1999, Conformational dynamics of vesicles, *Proc. Natl. Acad. Sci. USA*, **96**, 10550.

[97] Sandre, O., Moreaux, L., and Brochard-Wyart, F., 1999, Dynamics of transient pores in stretched vesicles, *Proc. Natl. Acad. Sci. USA*, **96**, 10591-10596.

[98] Kozlov, M. M. and Markin, V. S., 1983, Possible mechanism of membrane fusion, *Biofizika*, **28**, 242-247.

[99] Markin, V. S. and Albanesi, J. P., 2002, Membrane fusion: stalk model revisited, *Biophysical Journal*, **82**, 693-712.

[100] Misura, K. M. S, Scheller, R. H., and Weis W. I., 2000, Three-dimensional structure of the neuronal-Sec1syntaxin1a complex, *Nature*, **404**, 355-362.

[101] Tamm, L. K., Han, X., Li, Y., and Lai, A. L., 2002, Structure and function of membrane fusion peptides, *Biopolymers (Peptide Science)*, **66**, 249-260.

[102] Jahn, R. and Grubmüller, H., 2002, Membrane fusion, Current Opinion in Cell *Biology*, **14**, 488-495.

[103] Nanavati, C. and Fernandez, J. M., The secretory granule matrix: a fast-acting smart polymer, *Science*, **259**, 963-965.

[104] Tasaki, I. And Bryne, P. M., 1992, Discontinuous volume transitions in ionic gels and their possible involvement in the nerve excitation process, *Biopolymers*, **32**, 1019-1023.

[105] Monck, J. R., Oberhauser, A. F., Alvarez de Toledo, G., and Fernandez, J. M., 1991, Is swelling of the secretory granule matrix the force that dilates the exocytotic fusion pore?, *Biophys. J.*, **59**, 39-47.

[106] Holstein, T. and Tardent, P., 1984, An ultrahigh-speed analysis of exocytosis: nematocyst discharge, *Science*, **223**, 830-832.

[107] Tanaka, T., Hocker, L. O., and Benedek, G. B., 1973, Spectrum of light scattered from a viscoelastic gel, *J. Chem. Phys.*, **59**, 5151-5159.

[108] Tanaka, T. and Fillmore, D. J., 1979, Kinetics of swelling of gels, *J. Chem. Phys.*, **70**, 1214-1218.

[109] Chandler, D. E., and Heuser, J. E., 1980, Arrest of membrane fusion events in mast cells by quick-freezing, *The Journal of Cell Biology*, **86**, 666-674.

[110] Nardini, D. and Brebbia, C. A., 1983, A new approach to free vibration analysis using boundary elements, *Appl. Math. Model*, 7, 157-162.

[111] Ramachandran, P. A., 1994, *Boundary Element Methods in Transport Phenomena*, Computational Mechanics Publications, Southampton.

[112] Partridge, P. W., Brebbia, C. A., and Wrobel, L. C., 1992, *The Dual Reciprocity Boundary Element Method*, Computational Mechanics Publications, Southampton.

[113] Patridge, P. W., 1994, Dual reciprocity BEM: local versus global approximation functions for diffusion, convection, and other problems, *Engineering Analysis with Boundary Elements*, **14**, 349-356.

[114] Karur, S. R. and Ramachandran, P. A., 1994, Radial basis function approximation in the dual reciprocity method, *Mathl. Comput. Modeling*, **20**, 59-70.

[115] Šarler, B., 1998, Axisymmetric augmented thin plate splines, *Engineering analysis with boundary elements*, **21**, 81-85.

[116] Monck, J. R., Alvarez de Toledo, G., and Fernandez, J. M., 1990, Tension in secretory granule membranes causes extensive membrane transfer through the exocytotic fusion pore, *Proc. Natl. Acad. Sci.*, **87**, 7804-7808.

[117] Sheetz, M. P. and Dai, J., 1996, Modulation of membrane dynamics and cell motility by membrane tension, *Trends in Cell Biology*, **6**, 85-89.

[118] Roach, G. F., 1982, *Green's Functions*, Cambridge University Press, Cambridge.

[119] Debnath, L. and Mikusiński P., 1999, *Introduction to Hilbert Spaces with Applications*, Academic Press, San Diego.

[120] Stackgold, I., 1998, *Green's Functions and Boundary Value Problems*, John Wiley & Son, New York.

[121] Kellogg, O. D., 1953, *Foundations of Potential Theory*, Dover, New York.

[122] Tricomi, F., 1957, *Integral Equations, Interscience*, New York.

[123] Kress, R., 1999, *Linear Integral Equations*, Springer-Verlag, New York.

[124] Kythe, P. K., 1996, *Fundamental Solutions for Differential Operators and Applications*, Birkhäuser, Boston.

[125] Brebbia, C. A., Telles, J. C. F., and Wrobel L. C., 1984, *Boundary Element Techniques*, Springer-Verlag, New York.

[126] París, F. and Cañas, J. (1997), *Boundary Element Method: Fundamentals and Applications*, Oxford University Press, Oxford.

VITA

Tai-Hsi Fan, born in November 25, 1969 in Hualien, Taiwan. In 1992 he received Bachelor's degree in aerospace engineering from Tamkang University, Taiwan. Following the graduation he served in the Air Force for two years as a jet engine technical sergeant. After discharge in 1994, he came to the United States and studied mechanical engineering at the Pennsylvania State University majoring in thermal-fluid sciences, where he received Master's degree in 1996. From 1996 to 1999 Mr. Fan was an aerospace engineer specialized in designing jet engine rotating parts at Chen-Tech industries in California. He joined Professor Fedorov's research group in the Woodruff School of Mechanical Engineering at Georgia Tech in January 2000, and was admitted to PhD candidacy in the Spring semester of 2003.